

EVALUATION OF MULTI-PLATFORM LIDAR-BASED LEAF AREA INDEX ESTIMATES OVER ROW CROPS

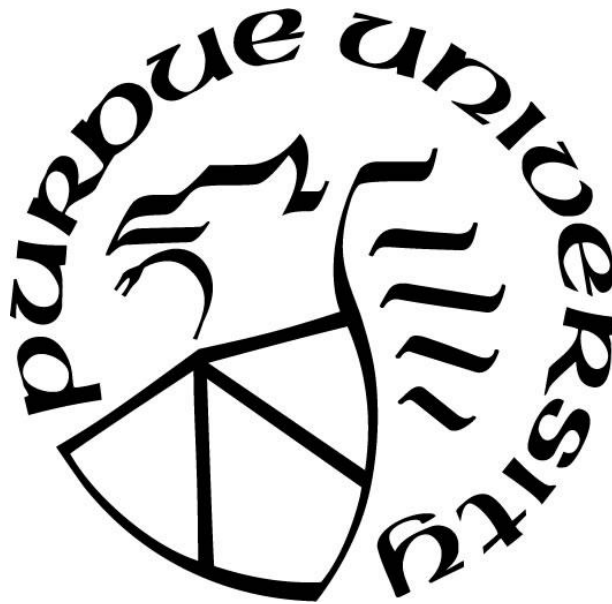
by
Behrokh Nazeri

A Dissertation

Submitted to the Faculty of Purdue University

In Partial Fulfillment of the Requirements for the degree of

Doctor of Philosophy



Lyles School of Civil Engineering

West Lafayette, Indiana

May 2021

THE PURDUE UNIVERSITY GRADUATE SCHOOL
STATEMENT OF COMMITTEE APPROVAL

Dr. Melba M. Crawford, Chair

Lyles School of Civil Engineering

Dr. Ayman F. Habib

Lyles School of Civil Engineering

Dr. James Bethel

Lyles School of Civil Engineering

Dr. Keith Cherkauer

Department of Agricultural & Biological Engineering

Approved by:

Dr. Dulcy Abraham

*To my beloved mother and sisters,
for their endless support.*

To the memory of my father.

And

To all frontline healthcare heroes in the COVID-19 pandemic

ACKNOWLEDGMENTS

First and foremost, I would like to express my sincere gratitude to my advisor Prof. Melba Crawford for her invaluable support, constant guidance, and advice throughout my doctorate program at Purdue University. She has been a source of immense motivation for me over the past few years in this research.

I also would like to thank the members of the advisory and examination committee Prof. Aymen Habib, Prof. Keith Cherkauer, and Prof. James Bethel for contributing toward my research through their insightful suggestions and inspiration.

I gratefully acknowledge the financial supports of the Advanced Research Projects Agency-Energy (ARPA-E), the U.S. Department of Energy under Grant DE-AR0000593, and the Lyles School of Civil Engineering for funding and supporting my research.

I would like to thank my friends and colleagues at the Purdue TERRA, DPRG, and LARS teams for their company and intellectual conversations over four years.

Last but not least, my deepest gratitude goes to my mother and sisters for their patience, understanding, and ceaseless love and support.

TABLE OF CONTENTS

LIST OF TABLES.....	8
LIST OF FIGURES	9
ABSTRACT	13
1. INTRODUCTION.....	15
1.1 Motivation.....	15
1.2 Objectives	18
1.3 Organization of the dissertation	19
2. ESTIMATING LEAF AREA INDEX IN SORGHUM USING WHEEL-BASED AND AIRBORNE DISCRETE RETURN LIDAR DATA	20
2.1 Abstract	20
2.2 Introduction	20
2.3 Materials and Methods.....	23
2.3.1 Study Area and Experiment Setting	23
2.3.2 Field Ground Reference Data	25
2.3.3 LiDAR Point Cloud Data Acquisitions	28
2.3.3.1 Platforms and Sensors.....	28
2.3.3.2 PhenoRover and UAV LiDAR Data.....	31
2.4 Methodology.....	32
2.4.1 Feature Extraction from LiDAR Data	32
2.4.2 Predictive Models of LAI.....	37
2.5 LAI Predictive Model Results	37
2.6 Summary and Conclusions	44
3. DETECTION OF OUTLIERS IN DISCRETE RETURN LIDAR DATA ACQUIRED BY MULTIPLE PLATFORMS OVER MAIZE AND SORGHUM	46
3.1 Abstract	46
3.2 Introduction	46
3.3 Materials	51
3.3.1 Experimental Setting	51
3.3.2 Experimental Data	53

3.3.2.1	Stationary Scanning of Plants	53
3.3.2.2	Image-based Point Clouds for the Sorghum Training Dataset.....	54
3.3.2.3	LiDAR Remote Sensing Data	55
3.4	Methodology.....	57
3.4.1	Geometric Approach.....	57
3.4.2	PointCleanNet Based Outlier Removal	60
3.4.3	LAI Estimation.....	63
3.5	Results.....	63
3.5.1	Geometric Outlier Removal from Individual Plants and Field Data	63
3.5.2	PointCleanNet Outlier Removal from Individual Plants and Field Data	67
3.5.2.1	Single Plants.....	67
3.5.2.2	Outlier Removal from Maize and Sorghum Field Data	70
3.5.3	Impact of PointCleanNet Outlier Removal method on LAI Estimation	73
3.6	Summary and Conclusions	77
4.	ESTIMATION LEAF AREA INDEX BY DEEP LEARNING-BASED FEATURE EXTRACTION FROM DISCRETE RETURN LIDAR DATA OVER AGRICULTURAL ROW CROPS	79
4.1	Abstract	79
4.2	Introduction	79
4.3	Materials	82
4.3.1	Experimental Setting	82
4.3.2	Experimental Data	84
4.3.2.1	LiDAR Point Cloud Data Acquisition	84
4.3.2.2	Ground Reference Data	86
4.4	Methodology.....	88
4.4.1	AutoEncoder Feature Extraction from LiDAR Data	88
4.4.1.1	SbDivTc_Cal (Sorghum).....	88
4.4.1.2	HIPS (Maize).....	94
4.4.2	Geometric Feature Extraction from LiDAR Data	96
4.4.3	Empirical Regression Models	97
4.5	Results.....	97

4.6	Summary and Conclusions	100
5.	CONCLUSIONS	102
5.1	Summary	102
5.2	Contributions of this work	102
5.3	Objectives and Key Findings.....	103
5.4	Research Limitations and Challenges	105
5.5	Future Work and Recommendations.....	106
	REFERENCES	108

LIST OF TABLES

Table 2.1. Experimental design for the 2019 and 2020 growing seasons	28
Table 2.2. Platforms and mounted sensors specification in 2019 and 2020	30
Table 2.3. Days After Sowing (DAS) relative to the available ground reference and LiDAR data in two experiments over SbDivTc_Cal	31
Table 2.4. Point density of sample data on 7/20/2020	32
Table 3.1. Experimental fields in 2020	53
Table 3.2. Platforms and mounted sensors specification in 2020.....	56
Table 3.3. LiDAR data and corresponding ground reference data in two experiments with associated DAS in 2020	57
Table 3.4. Ground point density for the HIPS maize experiment	62
Table 3.5. Ground point density of sorghum over SbDivTc_Cal sorghum experiment	62
Table 4.1. Experimental design for the 2020 growing seasons	84
Table 4.2. Platforms and mounted sensors specification	85
Table 4.3. Ground point density of sorghum over SbDivTc_Cal	85
Table 4.4. Ground point density of maize over HIPS	85
Table 4.5. Days After Sowing (DAS) relative to the available ground reference and LiDAR data in 2020	87
Table 4.6. Sorghum training time	89
Table 4.7. Maize training time	94

LIST OF FIGURES

Figure 2.1. Plot variety layout for 2020 SbDivTc_Cal panel	24
Figure 2.2. Photograph of the SbDivTc_Cal panel (July 20, 2020)	24
Figure 2.3. LiDAR-Based Height Map of SbDivTc_Cal Sorghum Panel (7/20/2020)	25
Figure 2.4. Measured ground reference LAI using: (A) Destructive sampling (2019), (B) Destructive sampling (2020), (C) LAI-2200C (2020).....	27
Figure 2.5. (a) PhenoRover platform with RGB/LiDAR/Hyperspectral/GNSS/INS sensors, (b) UAV-2 with RGB/LiDAR/GNSS/INS sensors in 2020.....	29
Figure 2.6. Example sensor point cloud sample data from (7/20/2020) from (a) PhenoRover (Bb) UAV-2, and (c) UAV-1.....	32
Figure 2.7. Typical plot; Rows 2 and 3 selected to extract features. The two arrows indicate rows 2 and 3. The orientation of the plot is shown with arrows (E: Easting, N: Northing, Z: Elevation).	33
Figure 2.8. Height of photoperiod sensitive variety SP SS405 FS relative to the surrounding plots 7/28/2020.....	33
Figure 2.9. Thematic region growing clustering steps: (a) Sample points. (b) Initial clustering. (c) Finding common points in two candidate clusters. (d) Connecting and joining two clusters.	35
Figure 2.10. Example of Clusters Area Plane (CAP) feature; (a) The third quartile of a row and (b) cross-section at the third quartile.	36
Figure 2.11. Sensitivity analysis: Feature correlation matrix (zero is the lowest correlation and 1 is the highest correlation)	37
Figure 2.12. R^2 values for 2019 UAV regression models for LAI estimation based on reference data from destructive sampling	38
Figure 2.13. R^2 values for 2020 regression models for LAI estimation; (PR: PhenoRover)	39
Figure 2.14. R^2 values for 2020 regression models (Circles): Removal of photoperiod sensitive varieties (ATx623xDwfYellMilo, ATx623xSC0044, and SP SS405 FS). (PR: PhenoRover).	40
Figure 2.15. Predictions based on SVR RBF models showing R^2 values and RMSE at midseason (7/20/2020) before and after removing photosensitive varieties for three platforms: a) UAV-1, b) UAV-2, and c) PhenoRover.	41
Figure 2.16. R^2 values for 7/13/2020: comparison of predictions based on the two ground reference methods (LI-2200C vs. destructive sampling)	42
Figure 2.17. Feature weight evaluation using SVR (RBF) on July 20 th 2020: (a) UAV-1, (b) UAV-2, (c) PhenoRover	43

Figure 3.1. PointCleanNet outlier removal architecture; \mathbb{P}' , \mathbb{P} , and \mathbb{O} denote a dataset contaminated with outliers as input, the dataset after outlier removal, and outliers, respectively. FCN and (Q)STN stand for Fully Connected and (Quaternion) Spatial Transformer Networks. The input is a patch point, and output is a label for each point regarding outliers (Rakotosaona et al., 2019).....	50
Figure 3.2. Plot variety layout for 2020 (a) SbDivTc calibration panel and (b) HIPS.....	52
Figure 3.3. Original single sorghum plant collected in the greenhouse	53
Figure 3.4. Overlapped images acquired for generating point clouds.....	54
Figure 3.5. Left to right: samples with 20%, 50%, and 70% outliers; three plant grouping.....	54
Figure 3.6. (a) PhenoRover platform with RGB/LiDAR/Hyperspectral/GNSS/INS sensors, (b) UAV-2 with RGB/LiDAR/GNSS/INS sensors in 2020.....	56
Figure 3.7. Majority voting procedure: (a) create a radius search around each bad point (b) determine the good points within the radius search (c) a new radius search is defined in the center of a good point and a radius of a distance between a good point and corresponding bad point (d) this step is repeated for all good points within a neighbor of bad point.....	58
Figure 3.8. Region growing clustering steps: (a) Point cloud. (b) Initial clustering. (c) Finding common points in two close clusters. (d) Connecting and joining two clusters.	59
Figure 3.9. The workflow of geometric outlier detection in two steps; non-isolated outliers were removed by the Wang and Feng (2015) method, and isolated outliers were removed by a clustering proposed method	59
Figure 3.10. Pre-trained vs. the network trained on the plant data loss in 200 epochs (the number of iterations). The loss range is between 0 and 1. If the model's prediction is perfect, the loss is zero	61
Figure 3.11. (a) Original LiDAR data with natural outliers. (b) Coarse level outlier removal from a sorghum plant. Arrows show the residual outliers from this step (c) Result of removal of residual outliers with two different views	64
Figure 3.12. Geometric method outlier removal for a synthetic point cloud.....	65
Figure 3.13. Geometric method outlier removal on joint three sorghum plants generated point cloud	65
Figure 3.14. UAV-2 LiDAR data of Maize (DAS:60) (a) Original data, (b) Point cloud after outlier removal.....	66
Figure 3.15. PhenoRover LiDAR data over Maize (DAS:62) (a) Original data, (b) Point cloud after outlier removal	67
Figure 3.16. outlier removal on individual plant LiDAR.....	68
Figure 3.17. PointCleanNet outlier removal for a point cloud based on a single plant	69
Figure 3.18. PointCleanNet outlier removal on joint three sorghum plants generated point cloud	69

Figure 3.19. Data from UAV-1 at 20 m altitude over maize (DAS: 60) (a) original data (b) outlier removal with PointCleanNet	70
Figure 3.20. Data UAV-2 at the altitude of 20 m over maize (DAS: 60) (a) original point cloud perpendicular to the direction of the rows; (b) results of outlier removal using PointCleanNet ...	71
Figure 3.21. PhenoRover LiDAR data of maize (DAS:62) (a) Original data, (b) Outlier removal PointCleanNet	72
Figure 3.22. UAV-2 LiDAR data of sorghum (DAS:68) (a) Original data, (b) Outlier removal PointCleanNet	72
Figure 3.23. Estimates of LAI for original data and after PointCleanNet based outliers removed from data acquired by the UAV and PhenoRover	74
Figure 3.24. Plot of estimated LAI vs. ground reference (a) original and (b) with outliers removed from PhenoRover data (7/24/2020) using PointCleanNet method	75
Figure 3.25. Maize LAI estimation on original and datasets with PointCleanNet outliers removed during the growing season on UAV and PhenoRover.....	76
Figure 4.1. PointNet Autoencoder architecture: the encoder part is PointNet, and the decoder is a fully connected network (FNN). The input of the network is all points in the dataset, and the output is the reconstructed input (Charles R. Qi, 2018/2020).....	81
Figure 4.2. Plot variety layout for 2020 (a) SbDivTc_Cal panel and (b) HIPS experiments.	83
Figure 4.3. Example point clouds acquired from UAV-2 (a) sorghum rows 2 and 3 from SbDivTc_Cal on July 13 th , 2020 (61 DAS), and (b) from maize from HIPS on July 11 th , 2020 (60 DAS).....	86
Figure 4.4. Evaluation of the loss between sorghum datasets with 2000, 5000, 7000 points.	88
Figure 4.5. Example of input with 2000 (a), 7000 (c), and 29000 (e) points; Figures (b), (d), and (f) show the corresponding reconstructed point clouds acquired from UAV-2 over sorghum rows 2/3 from SbDivTc_Cal on July 13 th , 2020 (DAS:61).....	90
Figure 4.6. Example of (a) input with 9000 points on 7/02/2020 (DAS:50) and 7/28/2020 (DAS:76), and (b) the corresponding reconstructed point clouds acquired from UAV-1 over sorghum rows 2 and 3 from SbDivTc_Cal.	91
Figure 4.7. Example of extracted features for one sorghum variety of the SbDivTc_Cal experiment (a) input with 2000 points for UAV-1 and UAV-2, (b) 7000 points for UAV-1 and UAV-2, and (c) 9000 points for UAV-1; 29,000 points for UAV-2.	93
Figure 4.8. Comparing the loss between maize datasets with 2000, 6000, 9000 points	94
Figure 4.9. Example of input with 2000 (a) and 9000 (c) points, (b) and (d) are the corresponding reconstructed points clouds acquired from UAV-2 over maize from HIPS on 7/11/2020 (DAS:60).	95
Figure 4.10. Example of extracted features for one maize variety of the HIPS experiment (a) input with 2000 points and (b) 9000 points for all datasets. The feature value does not have a unit.	96

Figure 4.11. R^2 values for sorghum SbDivTc_Cal 2020 SVR regression model for LAI estimation using geometric and autoencoder (AE) feature extraction methods.....	98
Figure 4.12. R^2 values for HIPS 2020 maize SVR regression model for LAI estimation using geometric and autoencoder (AE) feature extraction methods.....	99

ABSTRACT

Leaf Area Index (LAI) is an important variable for both for characterizing plant canopy and as an input to many crop models. It is a dimensionless quantity broadly defined as the total one-sided leaf area per unit ground area, and is estimated over agriculture row crops by both direct and indirect methods. Direct methods, which involve destructive sampling, are laborious and time-consuming, while indirect methods such as remote sensing-based approaches have multiple sources of uncertainty. LiDAR (Light Detection and Ranging) remotely sensed data acquired from manned aircraft and UAVs' have been investigated to estimate LAI based on physical/geometric features such as canopy gap fraction. High-resolution point cloud data acquired with a laser scanner from any platform, including terrestrial laser scanning and mobile mapping systems, contain random noise and outliers. Therefore, outlier detection in LiDAR data is often useful prior to analysis. Applications in agriculture are particularly challenging, as there is typically no prior knowledge of the statistical distribution of points, description of plant complexity, and local point densities, which are crop dependent. This dissertation first explores the effectiveness of using LiDAR data to estimate LAI for row crop plants at multiple times during the growing season from both a wheeled vehicle and an Unmanned Aerial Vehicle (UAV). Linear and nonlinear regression models are investigated for prediction utilizing statistical and plant structure-based features extracted from the LiDAR point cloud data and ground reference obtained from an in-field plant canopy analyzer and leaf area derived from destructive sampling. LAI estimates obtained from support vector regression (SVR) models with a radial basis function (RBF) kernel developed using the wheel-based LiDAR system and UAVs are promising, based on the value of the coefficient of determination (R^2) and root mean squared error (RMSE) of the residuals.

This dissertation also investigates approaches to minimize the impact of outliers on discrete return LiDAR acquired over crops, and specifically for sorghum and maize breeding experiments, by an unmanned aerial vehicle (UAV) and a wheel-based ground platform. Two methods are explored to detect and remove the outliers from the plant datasets. The first is based on surface fitting to noisy point cloud data based on normal and curvature estimation in a local neighborhood. The second utilizes the deep learning framework PointCleanNet. Both methods are applied to individual plants and field-based datasets. To evaluate the method, an F-score and LAI are calculated both before and after outlier removal for both scenarios. Results indicate that the deep

learning method for outlier detection is more robust to changes in point densities, level of noise, and shapes. Also, the predicted LAI was improved for the wheel-based vehicle data based on the R^2 value and RMSE of residuals.

The quality of the extracted features depends on the point density and laser penetration of the canopy. Extracting appropriate features is a critical step to have accurate prediction models. Deep learning frameworks are increasingly being used in remote sensing applications. In the last objective of this study, a feature extraction approach is investigated for encoding LiDAR data acquired by UAV platforms multiple times during the growing season over sorghum and maize plant breeding experiments. LAI estimates obtained with these inputs are used to develop support vector regression (SVR) models using plant canopy analyzer data as the ground reference. Results are compared to models based on estimates from physically-based features and evaluated in terms of the coefficient determination (R^2). The effects of experimental conditions, including flying height, sensor characteristics, and crop type, are also investigated relative to the estimates of LAI.

1. INTRODUCTION

1.1 Motivation

Within the last decade, light detection and ranging (LiDAR) has been used for mapping, modeling, and spatial analysis in many applications. The advantage of the LiDAR compared to other remotely sensed data such as imagery is that it provides three-dimensional coordinates directly. In modeling biophysical characteristics, including vegetation height, above-ground biomass, canopy structure, and leaf area index (LAI), promising results have been obtained from LiDAR (Lefsky et al. 2002). LAI is an important biophysical parameter that acts as a primary control for energy, water, and gas exchange within a vegetated ecosystem (Jensen et al. 2008). Estimation of LAI is also important for studies of atmosphere-vegetation interaction (Jonckheere et al. 2004) and crop modeling (Akinseye et al. 2017).

LAI was initially defined as leaf area per unit area of a plant (Watson, 1947). This definition is suitable for plants with flat leaves but not for other types of the leaves, such as curly and needle-shaped. It also does not relate directly to the vertical distribution of the leaves in the canopy. Other explanations were proposed to clarify the concept of LAI across different applications. Other definitions include half of the total leaf area (J. M. Chen & Black, 1991; Fassnacht et al., 1994), half the total intercepting area (Jing M. Chen & Black, 1992), and the projected leaf area (Myneni et al., 1997). For example, the definition “half the total leaf area” relates to biological processes, such as gas exchange, whereas “total intercepting area” concerns physical processes, such as interception of radiation (Yan et al., 2019).

Both direct and indirect approaches are used to estimate LAI. Direct methods are based on measuring the leaves area directly, and are thus costly and time-consuming. Indirect methods have been used for large-scale areas including for remote sensing studies, based on imagery and LiDAR (Lefsky et al., 2002a; Richardson et al., 2009). Two types of LiDAR metrics have been commonly used in LAI prediction, the Beer-Lambert law (Richardson, Moskal, and Kim 2009) and allometric measurements (Pope and Treitz 2013). The unique characteristics of LiDAR data have contributed to the development of more useful metrics (Zhao and Popescu 2009) for diverse applications. Based on the literature, few studies have focused on LAI estimation of low-height vegetation such as maize (Nie et al. 2016) and sorghum, compared to taller canopies such as trees. Data for most

remote sensing-focused studies were acquired by airborne platforms, including manned aircraft and UAVs. Acquisition from wheel-based LiDAR systems is less frequent for vegetation mapping (Ravi et al., 2018) and has not been investigated for estimation of LAI, although these platforms can acquire data over shorter vegetation compared to airborne platforms and are not subject to localized changes in position, elevation, and look angle that are common with airborne platforms.

LiDAR data from any platform, including stationary LiDAR scanning and mobile mapping systems, contain random noise (Deschaud and Goulette 2010). Therefore, outlier detection in LiDAR data is useful before further analysis. However, it is not a straightforward task for vegetation-related applications because there is no prior knowledge of the statistical distribution of points, and local point densities are crop dependent (Sotoodeh 2006). Many approaches have been developed for outlier detection in point clouds, including methods with normal and curvature estimation, machine learning, pattern recognition, and data mining (Nurunnabi, West, and Belton 2015). However, they have focused on solid structures with simple geometry compared to plants.

Recently, applications of deep learning have increased, including for analysis of remote sensing data. Deep learning is now widely applied to image-based applications, including target recognition, pixel-based classification, and feature extraction (L. Zhang et al., 2016). Lately, automation, including deep learning and machine learning in point cloud data analysis, has become an area of interest for researchers (Charles R. Qi et al., 2016; Ge et al., 2018; Poux & Billen, 2019; X. Cheng et al., 2019; Apolo-Apolo et al., 2020; Guo et al., 2020; van Klompenburg et al., 2020). The majority of current deep learning architectures, especially convolutional neural networks (CNNs), are not designed to be used with unstructured or irregular point clouds. In this case, the point clouds are sorted to 3D voxels before feeding to the network (Boulch & Marlet, 2016; Poux & Billen, 2019). This approach has some drawbacks, including loss of spatial information, because preservation of geometry depends on the voxel size. For this reason, having an architecture that is able to directly use an irregular point cloud is preferable. For example, PointNet (Charles R. Qi et al., 2016) is a deep neural network that takes unstructured point clouds as input and uses two sub-networks for classification and segmentation. Some studies have applied PointNet in their frameworks to address the classification, outlier removal, and segmentation problems (Charles Ruizhongtai Qi et al., 2017; Guerrero et al., 2018a; Charles R. Qi et al., 2018; Rakotosaona et al., 2019; Aoki et al., 2019). Besides outlier removal, deep learning frameworks can be used for feature learning and feature extraction. Kohara and Nakazawa (2019) extracted features using an

autoencoder and combined them with PointNet. An autoencoder is a deep learning neural network that reduces the dimensionality of input data at the early stages of a network and then decodes it to reconstruct the original data (Hinton & Salakhutdinov, 2006). Appropriate features are required to have a robust and reliable predictive model.

Leaf Area Index ground reference measurements: As noted earlier, both direct and indirect approaches are used to LAI field measurements. Since direct measurements of LAI are laborious, destructive in nature, and extremely time-consuming, there is a growing tendency to measure LAI using indirect approaches (Chen et al., 1997). Many studies focused on comparing the gap fraction indirect approach and direct methods. Generally, they concluded that the indirect approach underestimates the LAI values due to the clumping factor (Chen et al., 1997; Bréda, 2003; Ariza-Carricondo et al., 2019; Küßner & Mosandl, 2000). Some instruments were developed to measure the clumping factor, including the Tracing Radiation and Architecture of Canopies (TRAC) sensor (Chen et al., 1997) and the Multiband Vegetation Imager (MVI) (Kucharik et al., 1997). Additionally, some modeling-based methods were developed to compute the clumping index from indirect optical measurements (Fang et al., 2018). In general, 'good' results are those which agree to within 20% of direct measurements, without application of empirical calibration (Welles & Cohen, 1996).

Indirect methods infer leaf area index from measurements of the transmission of radiation through the canopies and gap fraction concepts based on radiative transfer theory using optical instruments such as the LAI-2200C Plant Canopy Analyzer and digital hemispherical photography. These methods are widely used for ground reference measurements and validation in remote sensing-based studies (Chen & Cihlar, 1996; Dou et al., 2016; Nie et al., 2016; Qu et al., 2014; Zeng et al., 2015). Applications using indirect methods are typically in three categories: forests (Chen & Cihlar, 1996; Fournier & Hall, 2017; Jensen et al., 2008a), row crops (Ariza-Carricondo et al., 2019; Blancon et al., 2019; Lang, 1986; Nie, Wang, Dong, & Xi, 2016), and individual trees (Brenner et al., 1995; Chang, 2020; Lang & McMurtrie, 1992).

In this study, the primary ground reference is based on the indirect optical approach, which was collected during the growing season in 2020 using an LAI-2200C Plant Canopy Analyzer (LI-COR, Lincoln, NE, USA). The LAI-2200C measures the gap fraction in five zenith angles (7°, 23°, 38°, 53°, and 68°) using a fish-eye lens and provides a total gap fraction rather than a value of detailed gap distribution in each zenith angle. A reference reading was made above the canopy,

followed by four below canopy readings. Limited destructive sampling data were also collected during the 2019 and 2020 growing seasons. The data were collected and processed by measuring green leaf area, plot leaf dry weight, and leaf mass, then computing the LAI as described in (Yang et al., 2021). In this study, results from the LAI-2200C are compared to estimates of LAI obtained from destructive sampling based on near coincident sampling days. Rigorous investigation of the relationship between these two ground reference methods requires more destructive sampling data on coincident dates with the LAI-2200C data and was beyond the scope of this study.

1.2 Objectives

The first objective of this research is to investigate the capability of LiDAR data point clouds acquired by a low altitude UAV and a converted high-clearance tractor over row crop plant breeding experiments to predict LAI. Destructive sampling-based and a plant canopy analyzer are evaluated for one common date as ground reference as a target-of-opportunity to provide a rudimentary comparison.

The second objective is to explore two methods to remove the outliers from LiDAR data collected over field experiments focused on plant breeding of sorghum and maize, which are similar, especially during the early growth stages of the plants. First, the outlier removal method by (Wang and Feng, 2015) is implemented and applied to a laser scanning data of a greenhouse plant and synthetic point cloud sorghum plant generated by overlapped imagery in an exploratory study, whose primary goal is to gain an understanding of the characteristics of the LiDAR data and the associated outliers for this type of plant structure. Next, the PointCleanNet network is trained using the synthetic point cloud sorghum plant, then tested on the single plant and two-row datasets (sorghum and maize) from an agricultural research farm.

The third objective is to investigate estimation of LAI using the PointNet AutoEncoder-based features based on LiDAR data acquired by UAV platforms over sorghum and maize field trials. The results are compared to those obtained using physical features based on the R^2 value of the LAI prediction model. In addition, the effects of experimental conditions, including flying height, LiDAR sensor characteristics, and crop type, are investigated relative to the estimates of LAI.

The contributions of this study include a) investigation of predictive modeling of LAI from multiple platforms including UAVs and wheel-based platforms using physical features in

conjunction with classical machine learning, b) investigation of outlier removal approaches over complex field plants to improve these models using physically-based features and deep learning, and c) investigation of autoencoder feature extraction from LiDAR point clouds as an alternative to the physical feature extraction method.

1.3 Organization of the dissertation

In Chapter 2, the capability of using LiDAR data to estimate LAI sorghum throughout the growing season is investigated. Ground reference data based on both indirect and direct methods are investigated using linear and nonlinear regression approaches for developing models of LAI for diverse hybrids of sorghum.

In Chapter 3, two methods are investigated to detect and remove the outliers from plant-based point clouds. The first is an extension of a traditional approach based on surface fitting to noisy point cloud data. The second utilizes the PointCleanNet deep learning framework. Both approaches are applied to individual plants and field-based datasets of multiple plants in rows.

In Chapter 4, a feature extraction approach is investigated for encoding LiDAR data acquired by UAV platforms over sorghum and maize plant breeding experiments. LAI estimates obtained with these inputs are then used to develop support vector regression (SVR) models using plant canopy analyzer data as the ground reference. The results are compared to models based on estimates from physically-based features and evaluated in terms of the coefficient determination (R^2). Also, the effects of experimental conditions, including flying height, sensor characteristics, and crop type, are investigated relative to the estimates of LAI.

Chapter 5 contains a summary of the findings for each of the three studies, limitations encountered, and potential research directions for future research.

2. ESTIMATING LEAF AREA INDEX IN SORGHUM USING WHEEL-BASED AND AIRBORNE DISCRETE RETURN LIDAR DATA

2.1 Abstract

Leaf area index (LAI) is an important variable for characterizing plant canopy in crop models. It is traditionally defined as the total one-sided leaf area per unit ground area and is estimated by both direct and indirect methods. This paper explores the effectiveness of using LiDAR data to estimate LAI for sorghum at multiple times during the growing season from both a wheeled vehicle and an Unmanned Aerial Vehicle (UAV). Linear and nonlinear regression models are investigated for prediction utilizing statistical and plant structure-based features extracted from the LiDAR point cloud data using ground reference obtained from an in-field plant canopy analyzer (indirect method) and leaf area derived from destructive sampling (direct method). LAI estimates obtained from support vector regression (SVR) models with a radial basis function (RBF) kernel developed using the wheel-based LiDAR system and UAVs are promising, based on the value of the coefficient of determination (R^2) and root mean squared error (RMSE) of the models.

2.2 Introduction

Determination of LAI is essential for modeling the interaction between the atmosphere and the biosphere (Zhu et al., 2020). It is an important biophysical parameter that acts as a primary control for energy, water, and gas exchange within a vegetated ecosystem (Jensen et al., 2008b). Estimation of LAI is also important for crop modeling (Akinseye et al., 2017; Lobell et al., 2015) and plant breeding (Blancon et al., 2019). Both direct and indirect approaches have been investigated to estimate LAI. Direct methods, which are based on measuring the area of the leaves directly, are accurate but costly, labor-intensive, and time-consuming. In destructive sampling, plants are defoliated within a specific area, and the one-sided leaf surface area is measured from imagery or with an electronic area meter (White et al., 2019) such as an LI-3100C. The average leaf biomass fraction and sample leaf weight (SLW) are used to compute LAI, as shown in Eqn. 2.1. for each plot and sampling date based on the method described by (Hammer et al., 2010; Yang et al., 2021).

$$LAI = \frac{\text{Plot leaf dry weight } (\frac{g}{m^2})}{SLW (\frac{g}{m^2})} \quad (\text{Eqn. 2.1})$$

where SLW is $\frac{\text{leaf dry weight } (g)}{\text{green leaf area}(m^2)}$ per plant.

Indirect optical methods estimate LAI from the canopy gap fraction that is defined as effective LAI (LAI_{eff}), assuming there is a random distribution of the leaves within the canopy volume (J. M. Chen et al., 2005; Ryu et al., 2010). The relationship between LAI_{eff} and true LAI derived from a direct method is shown in Eqn. 2.2.

$$LAI_{eff}(\theta) = \Omega(\theta) \times LAI \quad (\text{Eqn. 2.2})$$

where $\Omega(\theta)$ is the canopy clumping index, which describes the non-randomness of the leaf foliage distribution, it can be estimated through the non-random distribution of gap fractions using the logarithmic gap fraction averaging method, and θ is the solar zenith angle (Fang et al., 2019).

Digital cover photography (DCP), digital hemispherical photography, and the LAI-2200C plant canopy analyzer are all used to obtain indirect optically-based estimates of LAI (Fang et al., 2019; Fournier & Hall, 2017). Direct measurement methods and some optical methods are also used as references for indirect measurement techniques (Richardson et al., 2009). Indirect methods have been developed for determining LAI over large-scale areas using remote sensing based on both passive and active sensors. Within the last decade, light detection and ranging (LiDAR) has been used for mapping, modeling, and spatial analysis in many applications, including estimation of LAI. The advantage of the LiDAR compared to other remote sensing technologies is that it directly provides three-dimensional coordinates. Promising results have been obtained using LiDAR (Jimenez-Berni et al., 2018) and in combination with hyperspectral imagery (Masjedi et al., 2018, 2019) in modeling biophysical characteristics, including vegetation height and above-ground biomass for agriculture applications. LiDAR has also been used in forest canopy structure modeling (Lefsky et al., 2002) and for estimation of LAI in forests (Alonzo et al., 2015; Jung & Crawford, 2012; Korhonen et al., 2011; Zhao & Popescu, 2009), and agriculture (Nie, Wang, Dong, Xi, et al., 2016a; ten Harkel et al., 2020).

To estimate LAI from LiDAR, empirical models are developed to represent the relationship between the ground reference LAI and LiDAR-derived metrics. Two types of LiDAR metrics are commonly used in LAI prediction, the Beer-Lambert law based on the laser penetration index (LPI) (Richardson et al., 2009) and allometric measurements that are statistically-based features (Pope & Treitz, 2013a). Allometric related features include the mean height and standard deviation, maximum height of all returns, and the coefficient of variation of height. Features based on the Beer-Lambert law include gap fraction and the laser penetration index (LPI) (Nie et al., 2016). Pope and Treitz (2013) demonstrated the combined use of airborne discrete return LiDAR data and WorldView-2 high-resolution imagery to predict LAI in a boreal mixed wood forest. Digital hemispherical photos were used as a ground reference. Statistically significant LiDAR-based inputs for a stepwise linear regression model included the ratio of the first return and total return, the vertical distribution ratio (VDR), crown closure, and a vertical complexity index (VCI) that represents structural homogeneity with height (Ludwig et al., 1988; Pope & Treitz, 2013a; van Ewijk et al., 2011a).

Few studies have focused on estimating LAI for row crops, such as maize, e.g., (Nie et al. 2016) and sorghum, e.g., (Lang, 1986). In addition, in most remote sensing-focused studies, discrete return LiDAR data are acquired by manned aircraft and UAVs, which have lower point density and laser penetration than ground-based platforms. Ground-based LiDAR data can acquire data at a very high spatial resolution over shorter crops compared to airborne platforms, and depending on the plant structure, can potentially penetrate deeper into the canopy. Further, these platforms are not subject to localized changes in position, elevation, and look angle that are common with airborne platforms, but are restricted to operation in field conditions during which they can drive and collect data.

This study is an exploratory study of LAI prediction using LiDAR point cloud data acquired by a converted high-clearance tractor/sprayer with a custom sensor boom and by low altitude UAVs over sorghum plant breeding experiments. Remote sensing acquisitions were matched to the field-based LAI measurements using near-coincident data acquisitions. Multiple strategies for feature extraction were investigated for developing predictive models using regression-based methods, including stepwise multiple linear regression (SMLR), partial least squares regression (PLSR), and support vector regression (SVR). The models were evaluated based on the resulting R^2 value and RMSE of the residuals. Contributions of the study include investigation of multiple

LiDAR-based features for multitemporal prediction of LAI via regression models and evaluation of the capability of LiDAR sensors and platforms for acquiring data to predict sorghum LAI at multiple times during the growing season. Predictions based on direct and indirect methods for determining LAI were compared for a single common date.

2.3 Materials and Methods

2.3.1 Study Area and Experiment Setting

The experiments for this study were conducted at the Agronomy Center for Research and Education (ACRE) at Purdue University, West Lafayette, Indiana, USA, to evaluate the potential of sorghum varieties for biomass production. Both ground reference and LiDAR data were acquired during the 2019 and 2020 growing seasons. In this study, near concurrent ground-based and UAV LiDAR data were analyzed. The LiDAR data were collected from the Sorghum Biodiversity Test Cross Calibration Panel (SbDivTc_Cal), which contained 80 varieties. The experimental design included two replicates in a randomized block design planted in 160 plots (plot size: 7.6m \times 3.8m), ten rows per plot (row number is counted from the west to east). Figure 2.1 shows the layout of the plots in 2020 based on the respective genotypes.

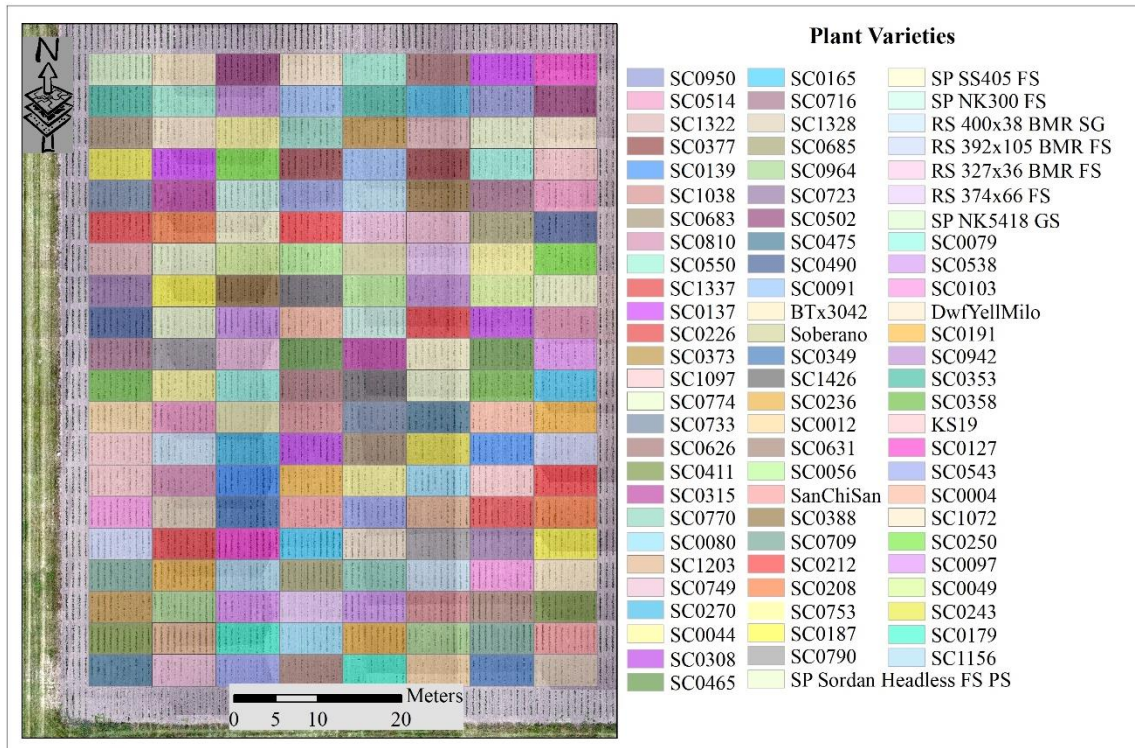


Figure 2.1. Plot variety layout for 2020 SbDivTc_Cal panel

Differences between varieties can be seen clearly in a photograph of the SbDivTc_Cal in 2020 in terms of physical characteristics such as size (short or tall), panicle structure, and color (Figure 2.2).



Figure 2.2. Photograph of the SbDivTc_Cal panel (July 20, 2020)

In both years, all 160 plots were included in the analysis for the SbDivTc_Cal data, as LAI ground reference data were acquired for all the plots in the experiment. Figure 2.3 shows a LiDAR height map from data acquired by a UAV on 7/20/2020, 68 days after sowing (DAS).

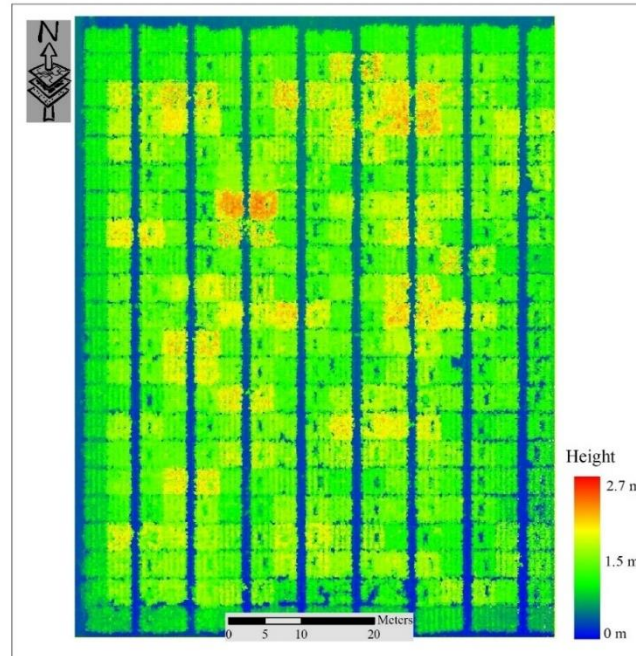


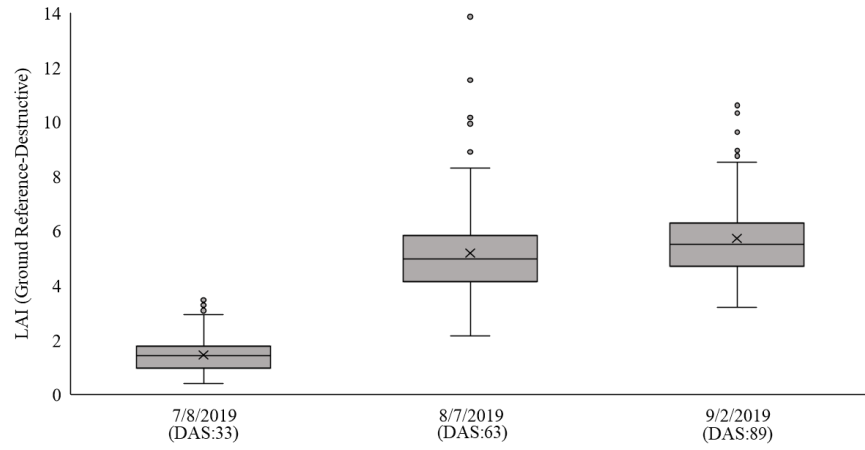
Figure 2.3. LiDAR-Based Height Map of SbDivTc_Cal Sorghum Panel (7/20/2020)

2.3.2 Field Ground Reference Data

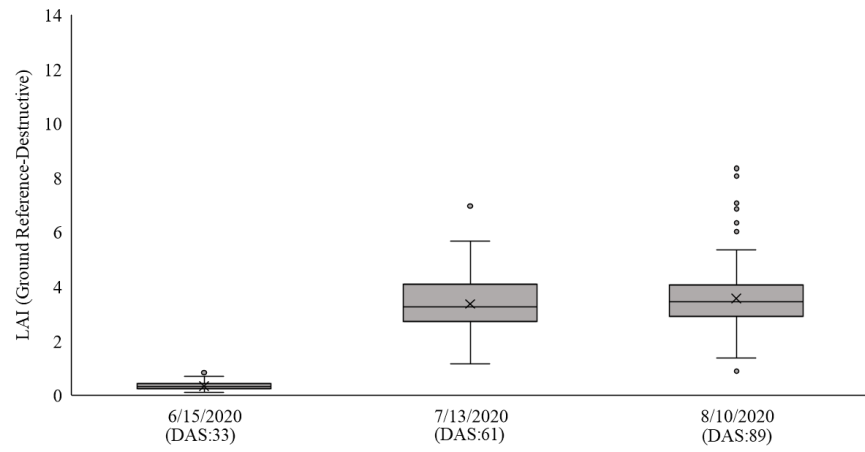
In 2019, three sets of manual destructive sampling data were collected by the Purdue team as ground reference data to parameterize a crop growth model. The data were also evaluated as a potential ground reference for developing predictive models of LAI based on LiDAR remote sensing data. The first collection was from July 5th to July 9th, the second was acquired from Aug 6th to Aug 8th, and the third from Aug 29th to Sep 4th. Two plants were harvested manually from plot rows 5 and 6. The leaves were then separated from the stems and scanned individually with an LI-3100C leaf area meter (LI-COR Inc., Lincoln, Nebraska, USA) to determine leaf size distribution. The average leaf biomass fraction and specific leaf weight (SLW) were used to compute LAI for each plot and sampling date (Eqn. 2.1) as described in detail by (Yang et al., 2021). Three remotely sensed data acquisitions that occurred within a week of these data collections were used to develop predictive models. To avoid the impact of adjacent plots and

destructive sampling, LiDAR data from Rows 2 and 3 of each plot were associated with each reference value for developing the predictive models.

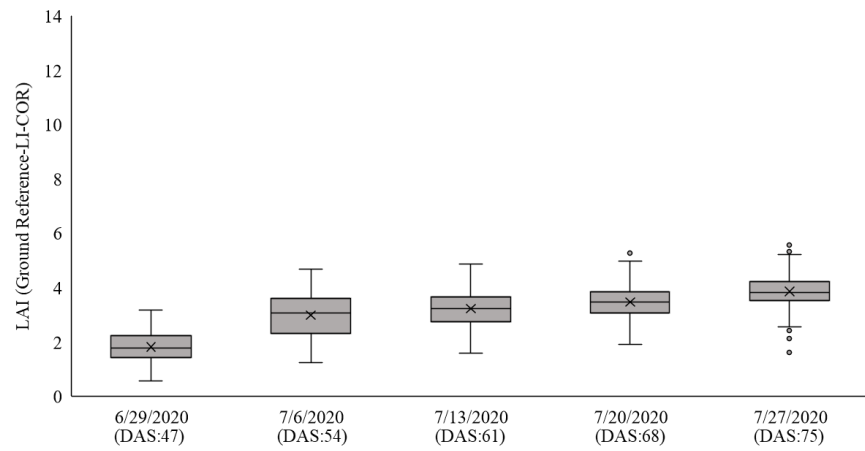
In 2020, reference data were collected weekly from June 29th to July 27th using a handheld plant canopy analyzer (LAI-2200C). The LAI-2200C is a portable instrument for acquiring an indirect measurement of LAI_{eff} based on canopy gap fraction analysis (Černý et al., 2019; Sonnentag et al., 2007; Welles & Cohen, 1996). Two sets of five measurements (one measurement above the canopy and four measurements below the canopy near the ground between rows 2 and 3 in the direction of the rows (north-south) were made according to the recommended protocol, then one value per plot was calculated using the Field Viewer 2200 (FV2200) software. These values were used as the primary reference data for developing predictive models of LAI based on the LiDAR remote sensing data. The ground reference values ranged from 0.5 to 6, increasing during the growing season. Three sets of destructive sample data were also collected on June 15th (rows 8 and 9), July 13th (rows 5 and 6), and Aug 10th (rows 2 and 3). The July 13th acquisition coincided with the plant canopy analyzer data, providing an opportunity to compare the plant canopy analyzer and destructive sampling approaches. The box plots in Figure 2.4 show the range of values of ground reference data within ± 1.96 standard deviations for 2019 and 2020 based on the date of data collection and corresponding DAS. The values of LAI exceeding the 95% box were from photoperiod sensitive varieties, whose characteristics increasingly differ from the rest of the experiment as the season progresses. The sequence of 2020 plant canopy analyzer data was used as a ground reference for evaluating the LiDAR-based metrics. Remotely sensed LiDAR data and ground reference acquisitions were separated by no more than three days. Table 2.1 summarizes the two years of experiments over SbDivTc_Cal 2019 and 2020.



(a) 2019 Ground reference (destructive sampling)



(b) 2020 Ground reference (destructive sampling)



(c) Ground reference LAI-2200C

Figure 2.4. Measured ground reference LAI using: (A) Destructive sampling (2019), (B) Destructive sampling (2020), (C) LAI-2200C (2020)

Table 2.1. Experimental design for the 2019 and 2020 growing seasons

Experiment	Year	Genotype	# of plots	# of varieties	Sowing Date	Harvest Date
SbDivTc_Cal	2019	hybrid	160	80	June 4	September 5
SbDivTc_Cal	2020	hybrid	160	80	May13	August 15

2.3.3 LiDAR Point Cloud Data Acquisitions

2.3.3.1 Platforms and Sensors

Remote sensing data were collected by the UAV weekly, first prior to planting to develop the baseline terrain model and at intervals of ~ 1 week thereafter, depending on the weather, throughout the growing season. In 2019, the UAV-based data collection platform was a Dà-Jiāng Innovations (DJI) Matrice 600 Pro (M600P) UAV that carried a Velodyne VLP-Puck LITE LiDAR sensor and a Sony α 7R III (ILCE-7RM3) RGB camera (Hasheminasab et al., 2020). The Velodyne VLP-Puck LITE has 16 channels that are aligned vertically from -15° to $+15^\circ$, resulting in a total vertical field of view (FOV) of 30° . The point capture rate in single return mode is ~300,000 points per second. The range accuracy is typically ± 3 cm, with a maximum measurement range of 100m (Velodyne VLP-Puck LITE, n.d.). The system was flown at an altitude of 44 meters and a speed of 3-5 m/s. In 2020, two M600P UAV platforms with sensors were flown over the study area at altitudes of 20 and 40 meters and speeds of 3-5 m/s. The UAVs were equipped with a Velodyne VLP-Puck Lite and a Velodyne VLP-32C, respectively. The Velodyne VLP-32C has 32 channels that are aligned vertically from -15° to $+25^\circ$, in a total vertical FOV of 40° . The point capture rate in a single return mode is ~600,000 points per second. The range accuracy is typically ± 3 cm, with a maximum measurement range of 200m (Velodyne VLP-32C, n.d.). The UAVs were equipped with an integrated global navigation satellite system/inertial navigation system (GNSS/INS) Trimble APX-15v3 for direct georeferencing. LiDAR data were also acquired by a wheel-based system, a LeeAgra Avenger agricultural high-clearance tractor/sprayer with a custom boom and mounted sensors, referred to in this study as the PhenoRover, on an experimental basis. The boom is constructed from T-slot structural aluminium framing with a 2.75 meters width, and the top of the boom can be raised to a maximum of 5.5 meters height from the ground. Sensors mounted on the boom include a Headwall hyperspectral VNIR machine vision camera, two FLIR

RGB cameras, and a Velodyne VLP-Puck Hi-Res LiDAR, as well as the GNSS/INS navigation system. The VLP-Puck Hi-Res has similar sensor specifications to the VLP-Puck LITE. Its FOV is -10° to $+10^{\circ}$ (Velodyne VLP-Puck Hi-Res, n.d.). The platform speed in the field was 1.5 miles per hour. Figure 2.5 shows the PhenoRover and UAV platforms for the 2020 data collection. PhenoRover data were acquired three times in 2020, subject to field conditions; 2019 was an extremely wet year, and no LiDAR data which could be associated temporally with destructive sampling were acquired by the PhenoRover over the sorghum. Table 2.2 details the platforms and their mounted sensor specifications for both 2019 and 2020.



(a)



(b)

Figure 2.5. (a) PhenoRover platform with RGB/LiDAR/Hyperspectral/GNSS/INS sensors, (b) UAV-2 with RGB/LiDAR/GNSS/INS sensors in 2020

Table 2.2. Platforms and mounted sensors specification in 2019 and 2020

Year	Platform	Sensor	Unit	Description
2019	UAV-1	RGB camera	1	36.4 MP Sony Alpha 7R (ILCE-7R)
		LiDAR sensor	1	Velodyne 16-Puck Lite-range accuracy of ± 3 cm
		GNSS/INS	1	Trimble APX-15 v2
2020	UAV-1	RGB camera	1	36.4 MP Sony Alpha 7R (ILCE-7R)
		LiDAR sensor	1	Velodyne VLP 16-Puck Lite-range accuracy of ± 3 cm
		GNSS/INS	1	Trimble APX-15 v2
		hyperspectral Camera	1	Nano Hyperspectral (VINIR)
	UAV-2	RGB camera	1	36.4 MP Sony Alpha 7R (ILCE-7R)
		LiDAR sensor	1	Velodyne VLP 32-range accuracy of ± 3 cm
		GNSS/INS	1	Trimble APX-15 v2
	PhenoRover	RGB camera	2	9.1MP FLIR Grasshopper3 GigE
		hyperspectral camera	1	Headwall Machine Vision 270 band line-scanning with 4.8 mm lens
		LiDAR sensors	1	Velodyne VLP-Puck Hi-Res
		GNSS/INS	1	Applanix POS-LV 125

Table 2.3 summarizes the LiDAR data collection and the corresponding ground reference measurements in terms of Days After Sowing (DAS) relative to the data collection dates and ground reference measurements.

Table 2.3. Days After Sowing (DAS) relative to the available ground reference and LiDAR data in two experiments over SbDivTc_Cal

Experiment	Year	Platform	Flying Height	Sowing Date	LiDAR Data Collection Date	DAS ¹	Ground Reference Date	DAS ²
1	2019	UAV-1	44 m	06/04	07/12	37	07/05, 07/08, and 07/09	30, 33 and 34
		UAV-1	44 m		08/10	66	08/06 to 08/08	62 to 64
		UAV-1	44 m		09/05	92	08/29 to 09/04	86 to 91
2	2020	PhenoRover	N/A	05/13	06/26	44	06/29	47
		UAV-1	40 m		07/02	50	06/29	47
		UAV-2	20 m		07/07	55	07/06	54
		UAV-2	20 m		07/13	61	07/13	61
		UAV-1	40 m		07/17	65	07/20	68
		PhenoRover	N/A		07/20	68	07/20	68
		UAV-1	40 m		07/20	68	07/20	68
		UAV-2	20 m		07/20	68	07/20	68
		PhenoRover	N/A		07/24	72	07/27	75
		UAV-1	40 m		07/28	76	07/27	75
		UAV-2	20 m		07/28	76	07/27	75

DAS¹: DAS with respect to data collection data; DAS²: DAS with respect to ground reference data

2.3.3.2 PhenoRover and UAV LiDAR Data

The average point densities of the LiDAR data acquired by the sensors on the UAVs depend on the type of sensor, the platform flying height, field of view, and mission characteristics such as the number of overlapping strips. In this study, point density is investigated based on flying height and sensor type, and it is presumed that the rest of the characteristics are consistent across the data acquisitions; these values are significantly lower than the LiDAR point density from the PhenoRover because the sensor on the PhenoRover operates at a much lower height (approximately 5m from the ground). Table 2.4 shows the point density of the sensors based on flying height. Figure 2.6 illustrates the resulting 3D point cloud from the UAV platforms and PhenoRover over a sample row. As expected, the canopy penetration achieved by the UAV sensors was lower than the PhenoRover due to the higher platform altitude. UAV-2 with a Velodyne VLP-32C (that was flown for other experiments) had a higher point density, resulting in greater canopy penetration compared to UAV-1 with a Velodyne VLP-Puck Lite as UAV-2. This was attributed

both to the higher pulse rate of the sensor and the lower altitude, as other characteristics affecting point density were identical in on both platforms.

Table 2.4. Point density of sample data on 7/20/2020

Platform	Flying Height	DAS	Point density (Points/ m ²)
UAV-1	40 m	68	70
UAV-2	20 m	68	500
PhenoRover	N/A	68	1400

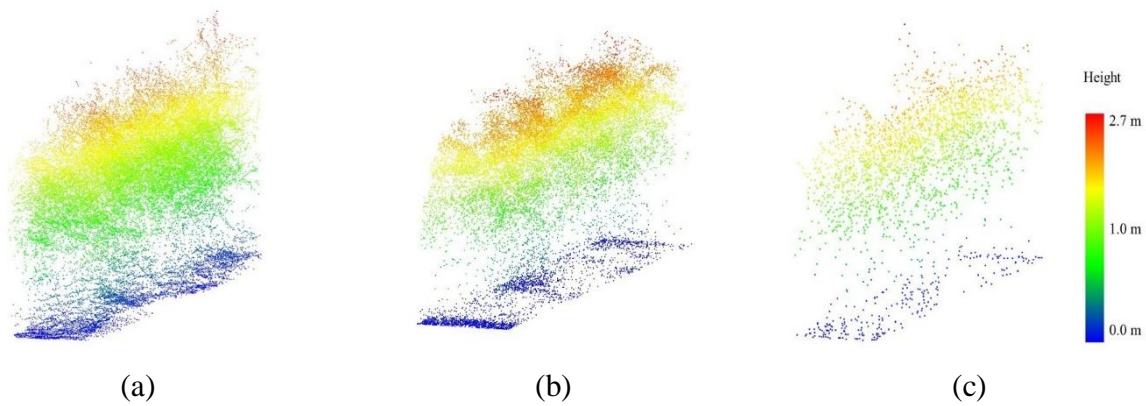


Figure 2.6. Example sensor point cloud sample data from (7/20/2020) from (a) PhenoRover (Bb) UAV-2, and (c) UAV-1.

2.4 Methodology

2.4.1 Feature Extraction from LiDAR Data

For this study, LiDAR features were extracted at the row-level within ten-row plots. Rows four, seven, and eight were adjacent to rows that were destructively sampled. Rows one and ten were “border” rows, so they were not necessarily representative of conditions within the plot, and particularly for light accessibility when plots with tall varieties were adjacent to plots with short varieties. Rows 2 and 3 were extracted from the remotely sensed data and analyzed for this study. Features were extracted from rows 2 and 3 as a spatially contiguous two-row block (essentially

equivalent to a two-row plot) where the ground reference was collected. Figure 2.7 shows a typical plot of the data set, where rows 5 and 6 were destructively sampled via machine harvesting, and manual destructive harvesting was performed in row 9.

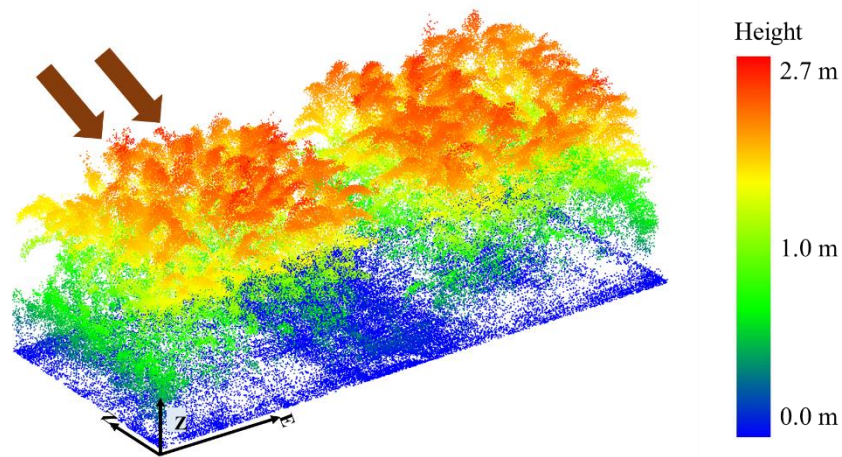


Figure 2.7. Typical plot; Rows 2 and 3 selected to extract features. The two arrows indicate rows 2 and 3. The orientation of the plot is shown with arrows (E: Easting, N: Northing, Z: Elevation).

Three varieties (ATx623xDwfYellMilo, ATx623xSC0044, and SP SS405 FS) are photoperiod sensitive, and as noted previously, and have a different plant structure than the rest of the varieties, especially later in the growing season. For example, “SP SS405 FS” was taller than the surrounding plots by approximately 1.3m on 7/28/2020 (Figure 2.8). The impact of these varieties on the predictive models was investigated.

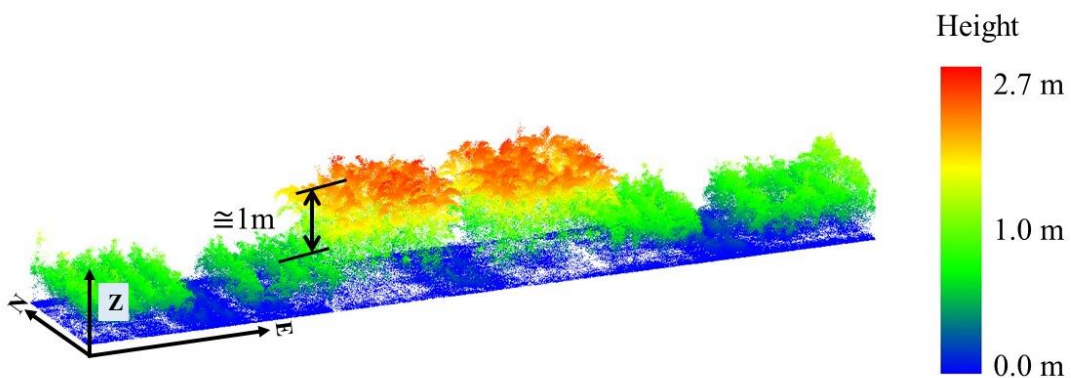


Figure 2.8. Height of photoperiod sensitive variety SP SS405 FS relative to the surrounding plots 7/28/2020

As noted in the Introduction, most LiDAR-based features proposed in the literature are based on the height or moments of the histograms of point cloud values in a 3D volume classified as vegetation. The Digital Terrain Model (DTM) required to determine plant heights was derived from a bare earth field using UAV-based LiDAR point cloud data before planting and assumed to be constant throughout the growing season. The height of points was estimated by subtracting the DTM from the “z” coordinate of each point in the dataset. Points with a height of less than 10 cm were considered as ground points and not included in the statistical analysis of the vegetation. The following physically-based features were explored for this study.

LPI is defined as the fraction of laser points that penetrate the canopy. The index can be calculated in many ways. In this study, it is computed as the ratio between the number of ground points (N_{Ground}) and the total number of points in a given area ($N_{Ground} + N_{vegetation}$), which is assumed here to be a row of a plot (Eqn. 2.3). The number of non-ground points is assumed to be equal to the number of points identified as vegetation ($N_{vegetation}$):

$$LPI: \frac{N_{Ground}}{N_{Ground} + N_{vegetation}} \quad (\text{Eqn. 2.3})$$

Features commonly used for allometric relationships include various statistically-based height features extracted from the non-ground point cloud, including plant height at various percent quantiles, mean height, standard deviation of the point cloud height, coefficient of variation of height, skewness of height, and Vegetation Complexity Index (VCI) as it is described in Eqn. 2.4 (van Ewijk et al., 2011a).

$$VCI = \frac{(-\sum_{i=1}^{HB} [p_i * \ln(p_i)])}{\ln(HB)} \quad (\text{Eqn. 2.4})$$

where HB = total number of height bins associated with vegetation (>10 cm), p_i = proportional abundance ($\frac{\text{N of returns}}{\text{Total N of returns}}$) in a height bin (i).

A new feature referred to as the Clusters' Area Plane (CAP), which is based on horizontal characteristics of the point cloud at a given height in a row, was proposed and evaluated in the study. To obtain the CAP feature, a plane is intersected with the point cloud within a row at a given plant height quartile, and the associated points are extracted. The points are clustered using a

region-growing approach based on the distance between points and the k-nearest neighbors as follows: the points are structured with a KD tree data structure, and the k-nearest neighbors to each point are determined within a defined radius and assigned to the respective clusters. Then, the clusters with common points are joined, and the cluster number is updated iteratively until no further changes occur in the clusters (Figure 2.9).

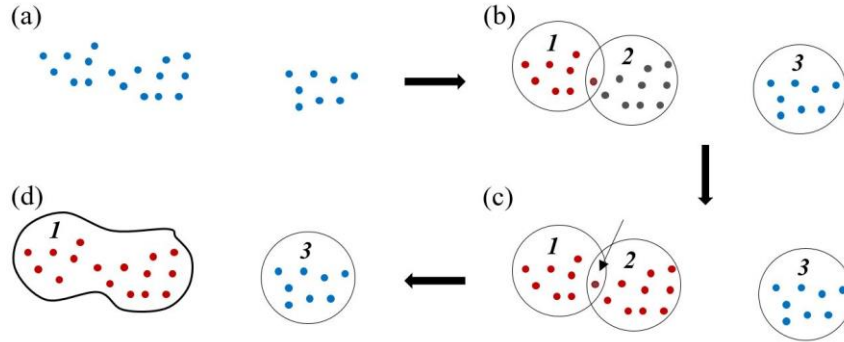


Figure 2.9. Thematic region growing clustering steps: (a) Sample points. (b) Initial clustering. (c) Finding common points in two candidate clusters. (d) Connecting and joining two clusters.

Finally, the area of clusters that is larger than a user-defined threshold is calculated, and the total area is defined as the CAP feature (Eqn. 2.5).

$$CAP = \sum_{i=1}^n A_i \quad (\text{Eqn. 2.5})$$

While the feature does not have a direct physical interpretation, it contains information for predicting LAI based on the horizontal distribution of the plants within the canopy at a given quartile (75% in this study). The CAP feature was also calculated in other quartiles, e.g., 50% and 25%, but only the 75% quartile provided statistically significant results for the data in these experiments. The 50% and 25% quartiles did not have adequate samples to evaluate the index, both due to penetration of the canopy and its geometric structure. Figure 2.10 shows a typical example of the CAP feature.

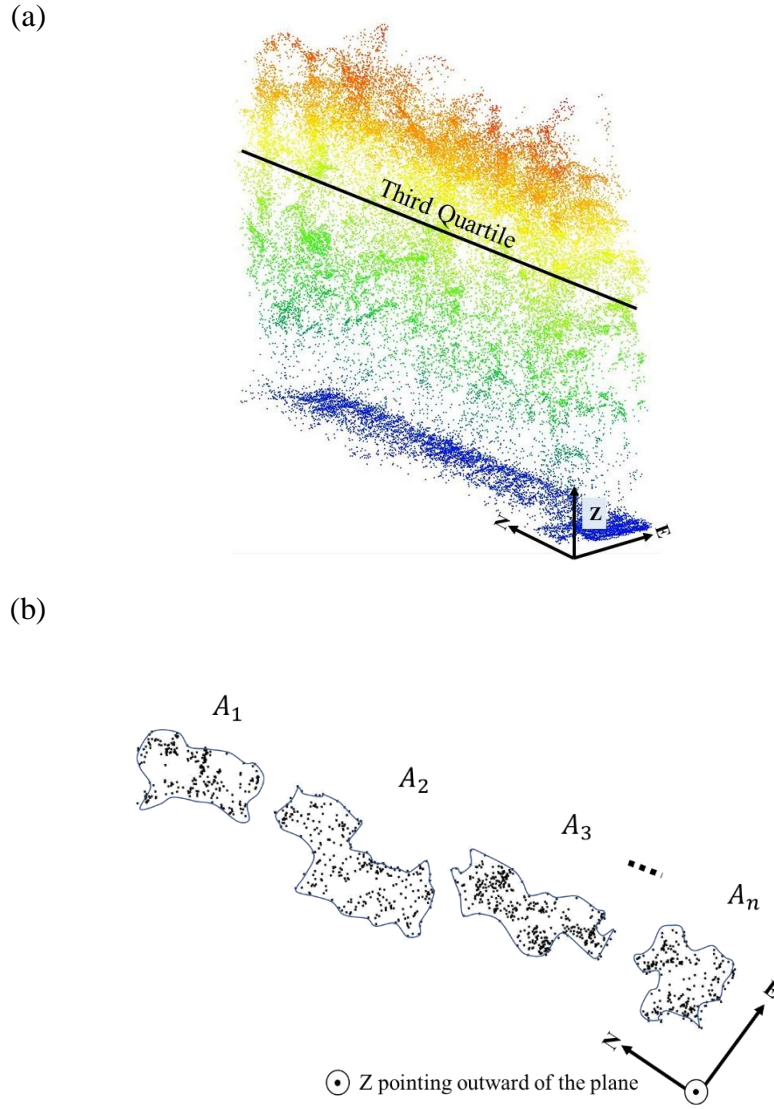


Figure 2.10. Example of Clusters Area Plane (CAP) feature; (a) The third quartile of a row and (b) cross-section at the third quartile.

Correlation between features and LAI indicated that LPI has the highest correlation with LAI. The CAP feature has the second-highest correlation with LAI. The correlation matrix in Figure 2.11 also indicates that there is a significant correlation between many of the features. For example, standard deviation height has more than 0.8 correlation with mean and third quartile height.

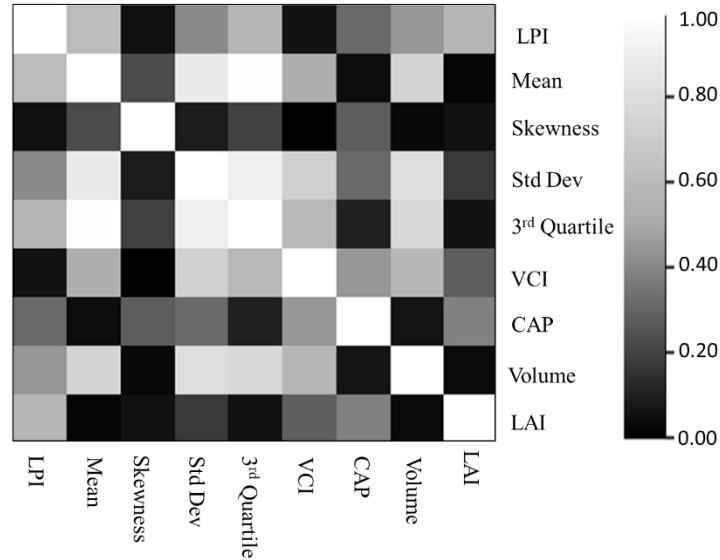


Figure 2.11. Sensitivity analysis: Feature correlation matrix (zero is the lowest correlation and 1 is the highest correlation)

2.4.2 Predictive Models of LAI

Predictive models were developed using stepwise multiple linear regression (SMLR) (Johnsson, 1992), partial least squares regression (PLSR) (Rosipal & Krämer, 2005), and support vector regression (SVR) (Feng & Li, 2014). For SVR models, the radial basis function (RBF) kernel parameters were obtained via grid search. Eight features were considered as input variables, including LPI, Height_mean, standard deviation, and skewness, Height (3rd Quartile), VCI, Volume of the vegetation in a row based on the convex hull of the points, and CAP. In this study, the training and test data were chosen randomly by 75% training and 25% test. Both replicates of each genotype variety were randomly assigned to either training or test. Ten-fold cross-validation was performed on the training set. The values of R^2 for the respective models are reported in the results section.

2.5 LAI Predictive Model Results

The results of the LAI predictive models are included for each year based on the date and the platform. SMLR, PLSR, and SVR models were developed with four kernels (linear, polynomial, RBF, and sigmoid) for the 2019 and 2020 sorghum data and illustrated via bar charts. Figure 2.12 shows that the mean and standard deviation of R^2 values obtained using 2019

destructively sampled data as ground reference. Models based on SVR with RBF kernels had consistently higher values of R^2 compared to other kernels.

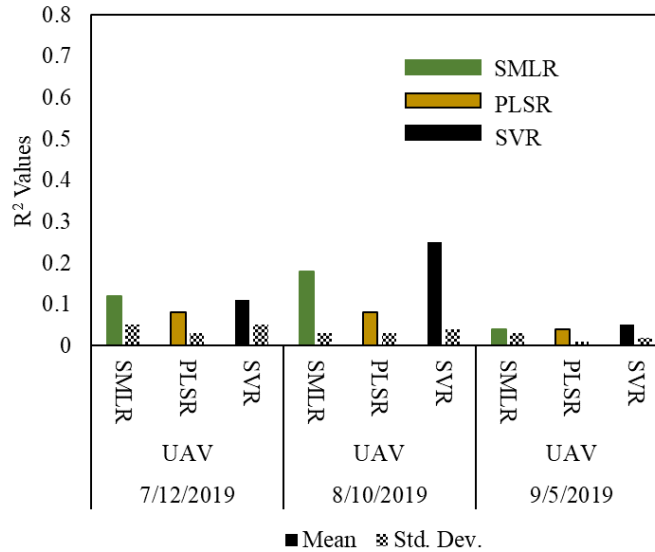


Figure 2.12. R^2 values for 2019 UAV regression models for LAI estimation based on reference data from destructive sampling

Results indicate that the relationship between the LiDAR data and LAI computed using destructively sampled ground reference data is weak. The results were not unexpected, as the LiDAR data is physically more closely related to the gap fraction than the assumptions in the LAI calculations based on destructive sampling (Fang et al., 2019; Hammer et al., 2010; Yang et al., 2021).

For the 2020 based predictions, the plant canopy analyzer data was used as a ground reference. Figure 2.13 shows the results for all datasets. The values of R^2 for the models were consistent throughout the period, even as the plant heights increased rapidly until flowering. UAV-2 (VLP32C, flown at 20m) data on 7/20/2020 resulted in the highest R^2 and lowest RMSE values. The results also did not indicate significant differences between the R^2 values from UAV-1 (VLP 16, flown at 40m), UAV-2, and the PhenoRover. However, the Phenorover fit was dramatically worse on 7/24/2020 compared to results prior and subsequent to this date. As noted earlier, the height of the platform is roughly 5 m from the ground, and some of the plants were tall enough to touch the boom and move. This movement could have contributed to the anomalous estimates.

Because of their height, the impact of the photoperiod sensitive varieties on the model fit was investigated.

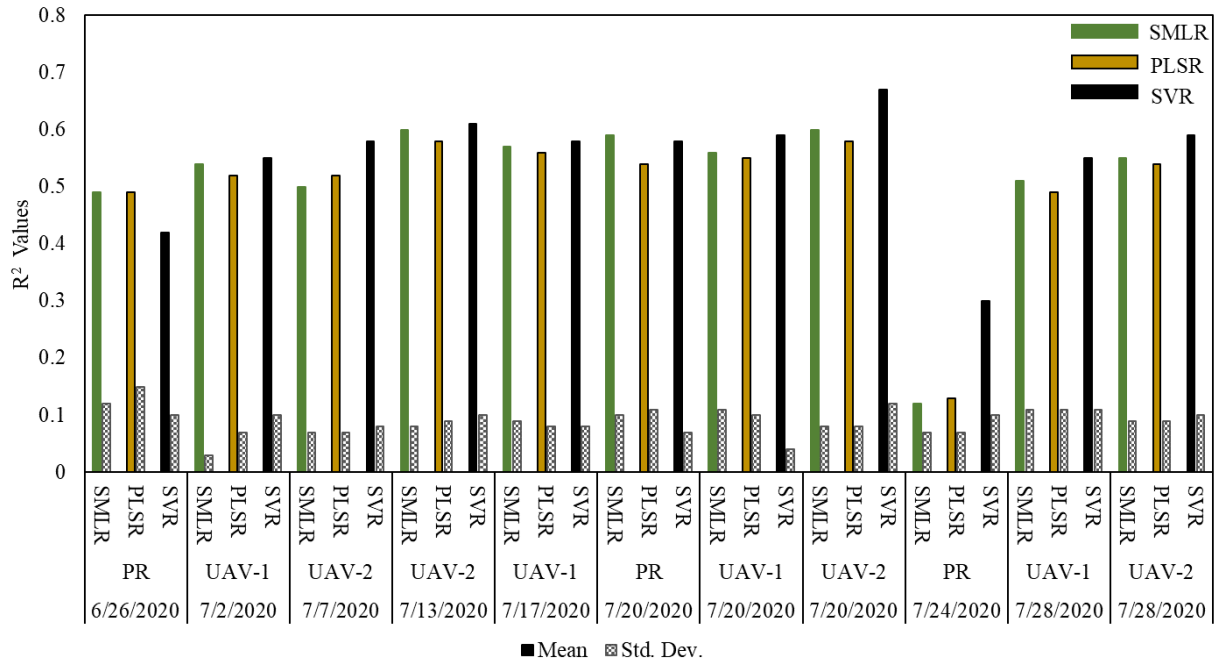


Figure 2.13. R^2 values for 2020 regression models for LAI estimation; (PR: PhenoRover)

The three photoperiod sensitive varieties were removed from the data set, resulting in increases in R^2 values of the models, and particularly for the PhenoRover data. For example, the R^2 of the PhenoRover 7/24/2020 model, when the photoperiod sensitive plants were the tallest during the PhenoRover acquisitions, increased from 0.30 to 0.56. Additionally, 7/24/2020 was a windy day (2.6 m/s) compared to other dates of data collection that had wind speeds less than 2.0 m/s. The R^2 values improved for all models after the photoperiod sensitive varieties were removed, with the greatest impact being on the SVR model obtained for the PhenoRover data (Figure 2.14).

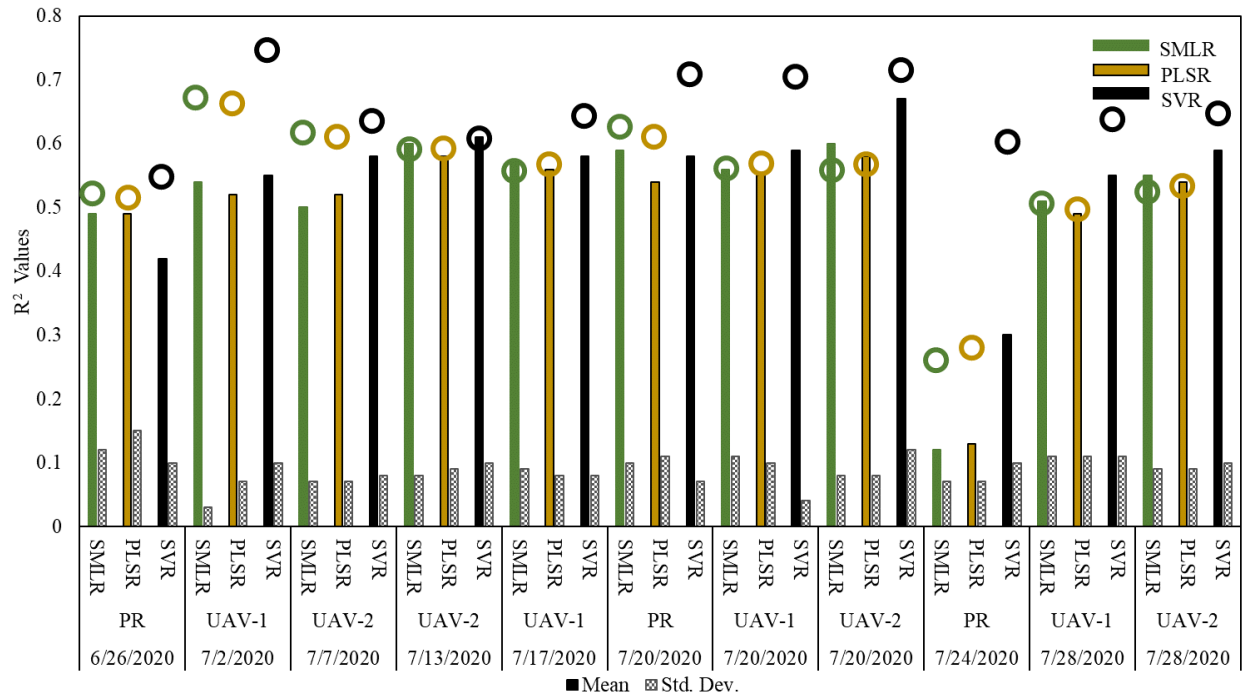


Figure 2.14. R^2 values for 2020 regression models (Circles): Removal of photoperiod sensitive varieties (ATx623xDwfYellMilo, ATx623xSC0044, and SP SS405 FS). (PR: PhenoRover).

The plots of the R^2 and RMSE of the models of the reference vs. the predicted values of the UAV and PhenoRover on 7/20/2020 before and after removing the photoperiod sensitive varieties from the datasets are provided in Figure 2.15. Removal of the photoperiod sensitive varieties also reduced the variability (std error) in the estimated LAI, and particularly for the late-season high values. Given the significant structural differences between the photoperiod sensitive and other forage and grain varieties, which increased as the year progressed, this reduction in standard deviation is consistent with expectations.

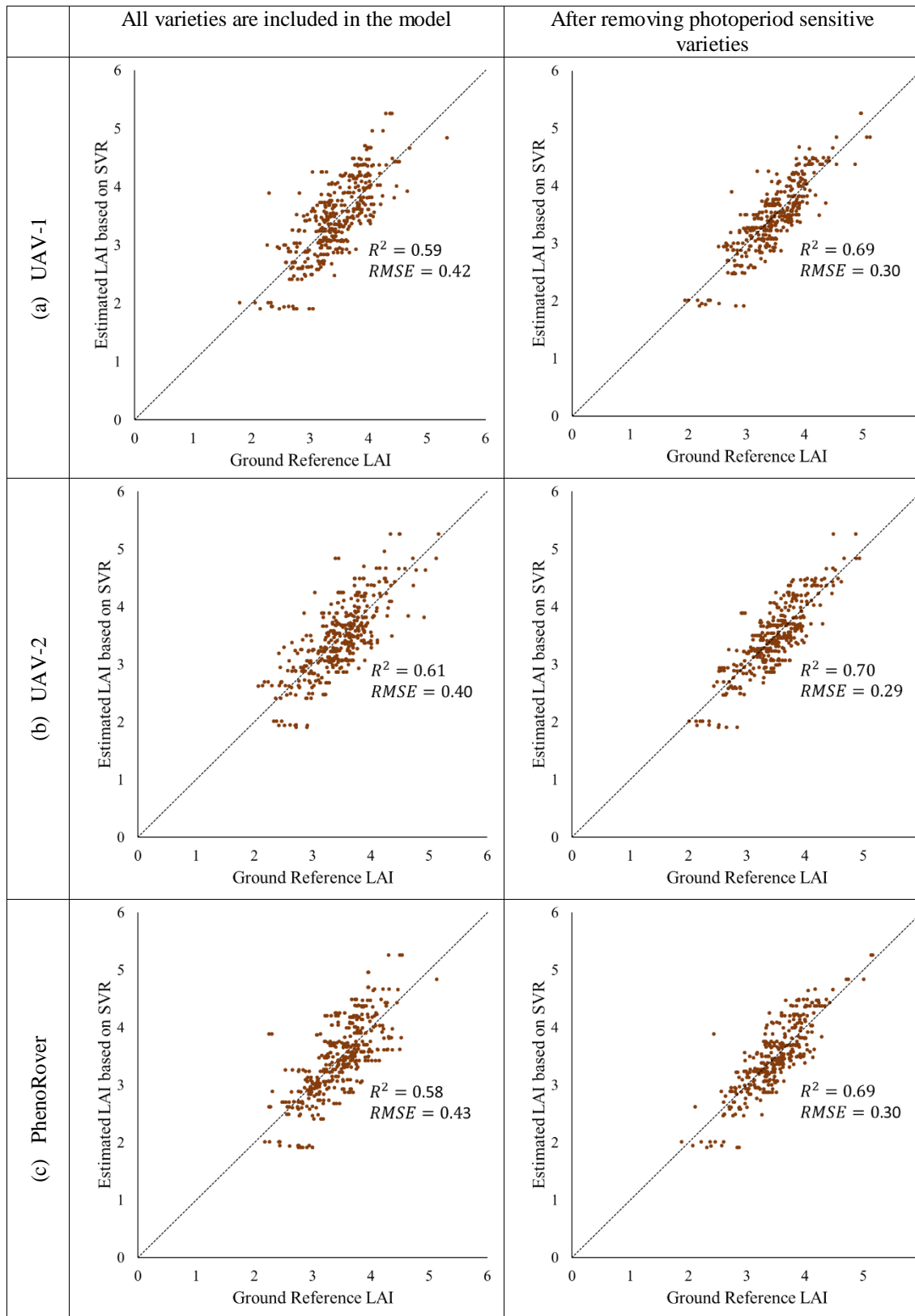


Figure 2.15. Predictions based on SVR RBF models showing R^2 values and RMSE at midseason (7/20/2020) before and after removing photosensitive varieties for three platforms: a) UAV-1, b) UAV-2, and c) PhenoRover.

Estimates of ground reference obtained from the LAI-2200C and destructive sampling were compared for the common sampling date, 7/13/2020. The correlation between the values of LAI derived from the two reference methods was only about 0.50. The R^2 of the corresponding model obtained using the LAI-2200C based LAI is higher than from destructive sampling (Figure 2.16). This is primarily attributed to the fact that both LAI_{eff} and LiDAR responses are related to the concept of gap fraction, while the LAI based on destructive sampling is based on other inputs such as sample leaf weight and leaf mass. Data from both ground reference approaches were available only in 2020, which was not adequate to thoroughly investigate the empirical relationship between the two ground reference values of LAI.

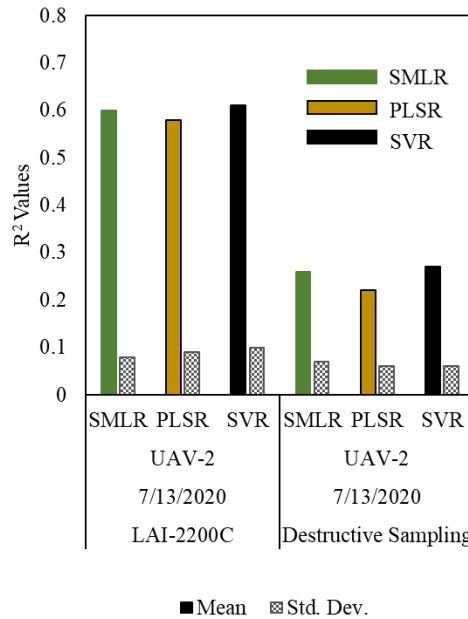


Figure 2.16. R^2 values for 7/13/2020: comparison of predictions based on the two ground reference methods (LI-2200C vs. destructive sampling)

To evaluate the importance of the features, a leave-one-out procedure was used with the SVR-RBF model, which had the highest R^2 value, and the resulting R^2 (R_{new}^2) was calculated (Eqn. 2.5)

$$Weight\ of\ feature = 1 - \frac{R_{new}^2}{R_{original}^2} \quad (Eqn. 2.6)$$

where R_{new}^2 is an R^2 of the model fit without the feature, and $R_{original}^2$ is the R^2 of the model with all features.

Figure 2.17 shows the feature importance in the models developed for the three platforms on July 20th 2020.

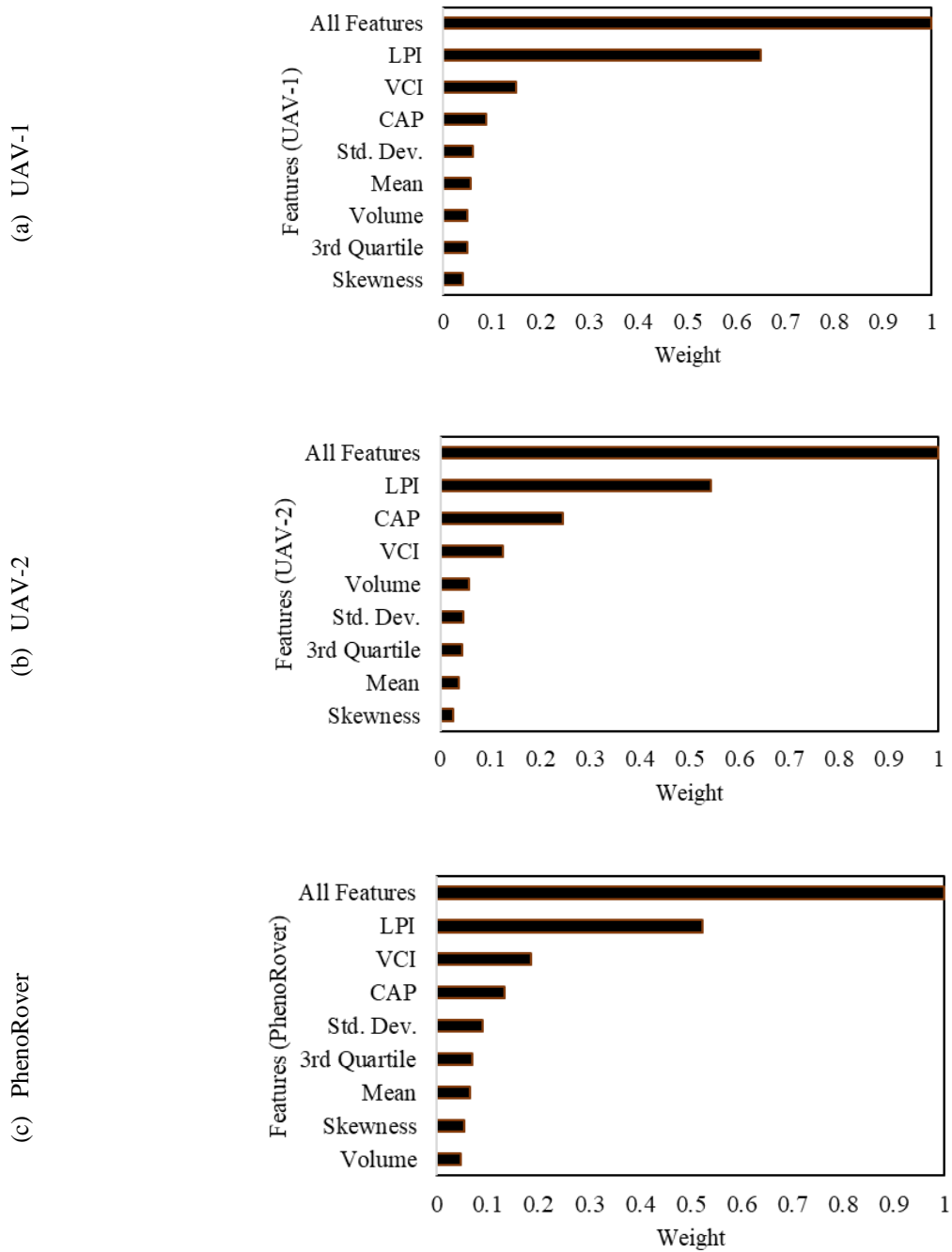


Figure 2.17. Feature weight evaluation using SVR (RBF) on July 20th 2020: (a) UAV-1, (b) UAV-2, (c) PhenoRover

LPI is the most highly ranked feature, as expected, based on the correlation with the plant canopy analyzer data, and the 2nd and 3rd ranked features are CAP and VCI, both of which are indicative of penetration of the canopy. The CAP feature further has some relationship to the horizontal distribution of the canopy, as noted previously. The height-related features are correlated and individually have a lower impact on the model, while LPI and CAP represent different characteristics. In complex vegetation such as sorghum, which is planted at high density and has tillers, many laser points are concentrated in the upper canopy, and few laser points penetrated deeper in the canopy.

Although the sensor on the PhenoRover was much closer to the canopy, typically between 2 and 5 meters depending on the date, and the speed of the PhenoRover was much slower, resulting in increased point density and penetration of the canopy, R^2 values of the models (Figures 2.14 and 2.15) based on using data from UAV-1 (flying height 40 m) and UAV-2 (flying height 20 m) were similar for comparable dates. In most cases, multiple stepwise linear regression models had the lowest R^2 value. In this model, just LPI and VCI features were significant at a p -value of 0.01. The R^2 value for the PLSR model is generally greater than or equal to linear regression but still lower than consistently achieved by SVR models with an RBF kernel. R^2 values from the middle stages in the growing season are higher than in the later-season in 2020 for all platforms. Earlier in the season, there was increased laser penetration of the shorter canopy, while later in the season, there was increased multi-path scattering when the canopy was more complex, and tillers contributed significantly to the LAI. The UAV-based models had a different pattern in R^2 value in 2019 compared to 2020. In 2020, the R^2 values were more consistent during the season. The platform in 2019 was flown higher (44) than the flight heights in 2020 (20 m and 40 m). However, the most important difference was that the ground reference in 2019 was based on the destructive sampling method, which was not as strongly related to LiDAR remote sensing data as the LAI-2200C based LAI.

2.6 Summary and Conclusions

In this exploratory study, the capability of discrete return LiDAR data acquired in the field at plot scale was investigated for predicting LAI_{eff} . Our contribution was to develop predictive models of LAI based on physical features from data acquired by multiple platforms during the growing season. Three LiDAR datasets that were collected in 2019 from a UAV platform were

post-processed and used to develop LAI predictive models based on available destructive sampling ground reference data. Due to low point density, limited canopy penetration, and use of destructive sampling-based LAI as a ground reference, the LAI models had low R^2 values. In 2020, UAV and wheel-based LiDAR datasets were collected and analyzed using a plant canopy analyzer, as well as destructive sampling for ground reference. LiDAR data acquired from UAV-2 with a Velodyne VLP-32C were higher density, and there was greater penetration of the canopy compared to UAV-1 with a Velodyne VLP-Puck Lite. This was due both to the sensor and the lower flight altitude. However, results indicate that the point density and canopy penetration did not have a significant impact on the resulting models for LAI, implying that the relationship to LAI was likely dominated by the upper canopy structure. Inclusion of data from photoperiod sensitive varieties had a significant impact on the results, particularly in the late season for the PhenoRover (R^2 for PhenoRover model increased from 0.30 to 0.57 by removal of these varieties).

The features used in this study were based on height-related statistical values and a canopy gap fraction feature (LPI), as well as a proposed horizontal feature. In most of the datasets, the UAV-based models had higher R^2 values than wheel-based data in 2020, especially later in the growing season when the complex scattering between the near range LiDAR and the canopy appeared to impact the models. The nonlinear regression model SVR with an RBF kernel had the highest R^2 and lowest RMSE of all other methods used in this study. The study encountered multiple challenges, including that the method for acquiring ground reference data was not consistent throughout the two-year period, as this was not a pre-planned study. The more frequent remote sensing data acquisitions and investigation of the plant canopy analyzer data in 2020 were motivated by the need for more frequent data acquisitions during the vegetative stages of the growth cycle when the plants were growing rapidly and during flowering. The data were also impacted by noise because of the complexity of plants in terms of dense planting and geometry, motivating subsequent research on denoising approaches. In addition, data encoding approaches may prove useful as an alternative to traditional structure-based approaches. Finally, further study is also needed to investigate the sensitivity of the different methods in providing ground reference data in terms of quality control and their impact on prediction models.

3. DETECTION OF OUTLIERS IN DISCRETE RETURN LIDAR DATA ACQUIRED BY MULTIPLE PLATFORMS OVER MAIZE AND SORGHUM

3.1 Abstract

High-resolution point cloud data acquired with a laser scanner from any platform, including terrestrial laser scanning and mobile mapping systems, contain random noise and outliers. Therefore, outlier detection in LiDAR data is often necessary prior to analysis. Applications in agriculture are particularly challenging, as there is typically no prior knowledge of the statistical distribution of points, plant complexity, and local point densities, which are crop dependent. The goal of this study is to investigate approaches to minimize the impact of outliers on discrete return LiDAR acquired over agricultural row crops, and specifically for sorghum and maize breeding experiments, by an unmanned aerial vehicle (UAV) and a wheel-based ground platform. Two methods are investigated to detect and remove the outliers from the plant datasets. The first is based on surface fitting to noisy point cloud data via normal and curvature estimation in a local neighborhood. The second utilizes the PointCleanNet deep learning framework. Both methods were applied to individual plants and field-based datasets. To evaluate the method, an F-score was calculated for synthetic data in the controlled conditions, and Leaf Area Index (LAI), the variable being predicted, was computed both before and after outlier removal for both scenarios. Results indicate that the deep learning method for outlier detection is more robust to changes in point densities, level of noise, and shapes. Also, the prediction of LAI was improved for the wheel-based vehicle data based on the coefficient of determination (R^2), and the root mean squared error (RMSE) of the residuals.

3.2 Introduction

In the last decade, light detection and ranging (LiDAR) sensors have become widely used to acquire three-dimensional (3D) point clouds for mapping, modeling, and spatial analysis. The data are impacted by systematic and random noise from various sources, including the movement of the laser scanner platform and/or reflection of the laser beam to the sensor from unwanted or multiple objects. Outlier detection is an important step in processing laser scanner data

contaminated by noise. Researchers have investigated multiple approaches to remove noise from LiDAR data, both for fundamental and applications focused studies.

Outlier detection and denoising are often used interchangeably. Noisy data refers to valid points that are displaced from their proper location. Denoising, in this case, involves moving these points as close as possible to their correct location. Outlier detection and removal is a process to detect and remove the points that are captured “mistakenly”. Denoising and outlier detection in a dataset depends on the point distribution and density of a point cloud. Deschaud and Goulette (2010) described denoising algorithms as either preprocessing a laser point cloud before reconstruction or post-treatment directly on meshes. Fleishman et al. (2003) proposed mesh denoising based on smooth surfaces, including filtering vertices in the normal direction using local neighborhoods as an adaptation of bilateral filtering for image denoising. Hanqi Fan et al. (2009) investigated post-processing of meshes using a feature preserving strategy. Points were categorized as sharp features, interior points, and points close to the boundary of a smooth region. The outliers were detected as anomalies from sub-neighborhoods, which were consistent in the normal orientation and geometry with the vertices. If the local neighborhood contains a large number of outliers, the surface estimated by these approaches could be biased and may not detect outliers associated with a dense outlier cluster. Other algorithms evaluate the surface normal and curvature at each point of data for outlier detection. Nurunnabi et al. (2015) proposed a neighborhood-based approach, where the maximum consistent subset of a neighborhood is generated; outliers are detected based on searching for the model best fit by the most homogenous and consistent points within the neighborhood. The method focuses on plane fitting, denoising, and sharp feature preservation.

Wang and Feng (2015) categorize the outliers in 3D laser scanning data as sparse outliers, which are distributed sparsely in the dataset, or in clusters that are characterized as isolated and non-isolated. Non-isolated clusters are connected to the main body of the scanned object, and it is not possible to remove them based on simple distance criteria and/or neighboring points. These outliers are the most challenging to separate from points that should be retained. To remove non-isolated outliers, they developed a method based on majority voting using local surface properties. Cluster surfaces that intersect with the main body surface as isolated outliers are then marked. The authors indicate that this algorithm performs better for shapes that have regular geometry and

smooth surfaces (Wang and Feng, 2015). For complex shapes and geometries like plants where many surfaces (leaves) intersect, this isolated outlier detection approach may not be effective.

Outliers are affected by the system characteristics (e.g., platform type and sensor) and the objects being scanned (e.g., geometric complexity and size of the objects). Successful outlier detection from a LiDAR dataset using conventional approaches is strongly related to these characteristics. Deep learning frameworks, which have been explored recently for this purpose, provide a fundamentally different strategy. Classical machine learning methods seek to explore the structure of the data or to estimate the relationship between variables. Deep learning automatically learns low and high-level features that are both representative and discriminative from data being modeled for classification and prediction. The models are learned iteratively using extensive quantities of training data, which are sometimes difficult to obtain (Bengio, 2012; Lauzon, 2012).

Recently, applications of deep learning have increased dramatically, including in remote sensing. Deep learning is now widely used in image-based applications, including target recognition, pixel-based classification, and feature extraction (Liangpei Zhang et al., 2016; G. Cheng et al., 2018; Ma et al., 2019; Petrovska et al., 2020). It has also been explored in the analysis of laser scanner data, such as data denoising, classification, and segmentation. Boulch and Marlet (2016) used a convolutional neural network architecture to estimate the normal to each point in its neighborhood as the first step in segmentation and point cloud classification. Conventional geometry-based algorithms were then used to detect objects in LiDAR data via clustering. Li, Zhang, and Xia (2016) proposed a five-layer convolutional network to detect vehicles scanned by a Velodyne 64E laser scanner. The LiDAR data were projected to 2D maps similar to depth maps of RGBD data.

Agresti et al. (2019) developed a method for denoising time-of-flight sensor data acquired by a range imaging camera that was contaminated with noise, had sparse spatial resolution, and multipath interference. They introduced a transfer learning architecture that was able to denoise real data by training on SYNTH3 (Agresti et al., 2017) synthetic data, which had been generated using the Blender3D rendering software. The network architecture includes a coarse-fine CNN that extracts features from raw data and then estimates a noise-free depth map. The coarse network applies down-sampling with pooling layers, and the fine network provides a detailed accurate representation. Cheng et al. (2019) proposed a deep learning architecture for the fusion of LiDAR

data and stereo images to develop an accurate 3D scene. The method could also handle misalignment between the sensors and noisy LiDAR data (X. Cheng et al., 2019).

Processing point cloud or LiDAR data is problematic for deep neural networks due to the characteristics of point sets in \mathbb{R}^n , including interaction among points, invariance under transformation, and unordered points, unlike pixel arrays in images or voxel arrays in volumetric grids. The majority of current deep learning architectures, and especially CNN, are not designed to work with unstructured or irregular point clouds. Most researchers have resorted to assigning point clouds to 3D voxels before inputting them to the network. This approach has drawbacks, including loss of spatial information. For this reason, having an architecture that can directly use an irregular point cloud is preferred.

The PointNet (Charles R. Qi et al., 2016) deep neural network accommodates unstructured point clouds as input without voxelization (Garcia-Garcia et al., 2017). It provides a unified architecture for a wide variety of applications, including object classification, part segmentation, and scene semantic parsing. PointNet accommodates these characteristics of point sets in its architecture using a symmetric function for unordered input, aggregating local and global features to solve point interactions, and adding an alignment network to make the model invariant to transformation. The PointNet network has three main components: a max-pooling layer as a symmetric function to aggregate information from all the points, a local and global information combination structure, and two joint alignment networks (Jaderberg et al., 2015) for making input points and feature points invariant to transformation.

Some other networks, such as Hand PointNet (Ge et al., 2018), which can be applied to hand pose estimation, were derived from PointNet. It uses the normalized point cloud as the input and regresses it to a low dimensional representation of a 3D hand pose. PCPNet (Guerrero et al., 2018b) is an approach for estimating local shape properties in point clouds. The PCPNet architecture is based on local batch learning, as two adjacent patches may have different types of structures in terms of edges and corners. Thus, it can use a small dataset of labeled shapes for training. The training dataset contains eight shapes, including man-made objects, geometric constructs, and scanned figurines. This approach is suitable for estimating local surface properties such as normal and curvature, which are classical geometric characteristics. Although PCPNet has achieved promising results for a variety of objects, it can fail in some settings, such as large flat areas, due to a lack of adequate information to determine the normal orientation. PointCleanNet

(Rakotosaona et al., 2019) is adapted from PCPNet, with the goal of producing a clean point cloud by removing outliers and denoising a noisy, dense point cloud. The network has two stages: it first removes the outliers from the dataset and then estimates the correction vectors for the rest of the points to move the points toward the original surface. Figure 3.1 illustrates the outlier removal architecture.

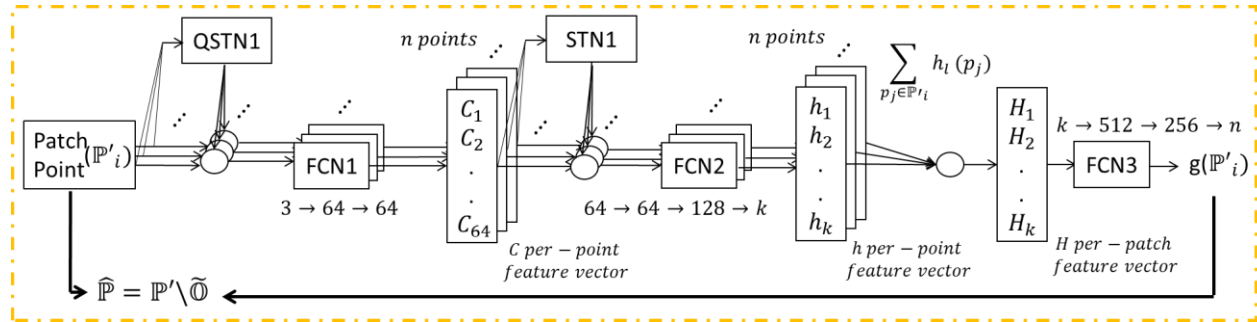


Figure 3.1. PointCleanNet outlier removal architecture; \mathbb{P}' , $\hat{\mathbb{P}}$, and $\tilde{\mathbb{O}}$ denote a dataset contaminated with outliers as input, the dataset after outlier removal, and outliers, respectively. FCN and (Q)STN stand for Fully Connected and (Quaternion) Spatial Transformer Networks. The input is a patch point, and output is a label for each point regarding outliers (Rakotosaona et al., 2019).

The objective of this study is to explore both a physical, geometric-based strategy and a deep learning architecture to remove the outliers from LiDAR data collected for experiments focused on plant breeding of sorghum and maize, which are similar, especially during the early growth stages of the plants. First, the outlier removal method by (Wang & Feng, 2015) was implemented and applied to laser scanning data of a single sorghum plant in an exploratory study, whose primary goal was to gain understanding of the characteristics of the LiDAR data and the associated noise and outliers over this type of plant structure. The PointCleanNet network was also investigated. It was trained using synthetic point cloud sorghum plant generated by overlapped imagery derived from data acquired in a controlled facility, then tested on datasets (sorghum and maize) from an agricultural research farm.

Because there is no ground reference over field-based data, a surrogate measure was used to evaluate the results. Leaf Area Index (LAI), a characteristic related to plant structure, was estimated over the sorghum field using the original data and data from which outliers had been removed. LAI is defined as the total one-sided leaf area per unit ground area; it is widely used in

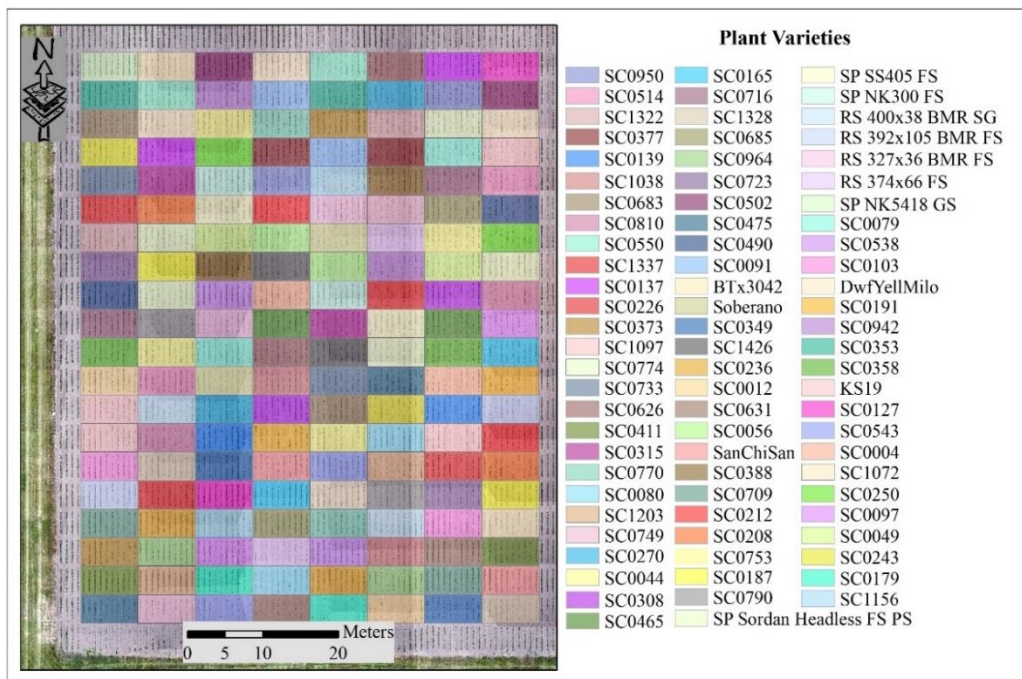
agriculture and forestry as a measure of canopy characteristics (Lobell et al., 2015; Akinseye et al., 2017; Blancon et al., 2019). It is commonly measured by indirect methods such as optical sensing via hand-held plant canopy analyzers and remote sensing data, including LiDAR data, are based on the concept of gap fraction (Fang et al., 2019). LiDAR data from the UAV and a wheel-based platform (PhenoRover) that were matched to field-based LAI acquisitions were used to estimate LAI using regression models. Field data were collected for phenotyping experiments at the Purdue Agronomy Center for Research and Education (ACRE), where extensive manual measurements were also being made. The models from the data prior and subsequent to outlier removal were evaluated based on the resulting R^2 statistic and RMSE of the residuals.

3.3 Materials

3.3.1 Experimental Setting

The experiments for this study were conducted at the Agronomy Center for Research and Education (ACRE) at Purdue University, West Lafayette, Indiana, USA, to evaluate the potential of sorghum varieties for biomass production. LiDAR data utilized in this study were acquired during the 2020 growing season. The approaches to outlier removal were evaluated using LiDAR data that were collected from the Sorghum Biodiversity Test Cross Calibration Panel (SbDivTc_Cal) and the maize High-Intensity Phenotyping Sites (HIPS) in comparison to Leaf Area Index (LAI). In the early stages, maize and sorghum have very similar plant structures, although sorghum was planted at a higher density (~200,000 plants/hectare) compared to maize (~75,000 plants/hectare). The geometric structure of sorghum becomes more complex as tillers develop during the season, decreasing canopy penetration. SbDivTc_Cal in 2020 contained 80 varieties). The experimental design included two replicates in a randomized block design planted in 160 plots (plot size: 7.6m × 3.8m), ten rows per plot. The HIPS maize experiment contained 44 varieties of maize with two replicas, including hybrid and inbred. This experiment included 88 plots (plot size: 1.5m × 5.3m), two rows per plot. Figure 3.2 shows the layout of the plots for the SbDivTc_Cal and HIPS experiments in 2020 based on the respective genotypes. Table 3.1 shows a summary of the field experiments.

(a)



(b)

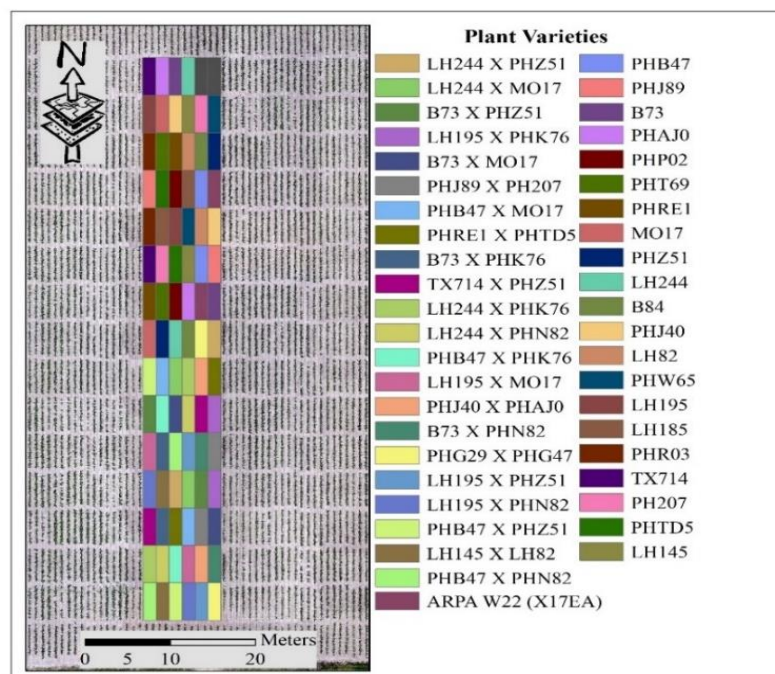


Figure 3.2. Plot variety layout for 2020 (a) SbDivTc calibration panel and (b) HIPS

Table 3.1. Experimental fields in 2020

Farm	# of plots	# of varieties	Sowing Date	Harvest Date
HIPS	88	44	May 12	October 1
SbDivTc_Cal	160	80	May 13	August 15

3.3.2 Experimental Data

LiDAR data acquired by multiple sensors and platforms were used to evaluate the outlier removal methods. The following sections describe the sources and characteristics of the data.

3.3.2.1 Stationary Scanning of Plants

A stationary LiDAR dataset was collected over a single sorghum plant in a greenhouse at Purdue University using a FARO terrestrial laser scanner. The FARO Focus^{3D} X 330 single beam range is between 0.6 m and 330 m indoor or outdoor with a range accuracy of ± 2 mm. The total vertical field of view (FOV) and horizontal FOV are 300° and 360° , respectively. The point capture rate is $\sim 122,000$ points per second (FARO Focus3D X 330). The average point distance (the distance of a point from its neighbors) in this dataset is 1.5 mm/10 m, and the scanner was located 2 m from the plant. The data were used to investigate the characteristics of the plant and associated noise and explore geometric methods for outlier removal before applying them to field data. Figure 3.3 shows an example of the raw scan.

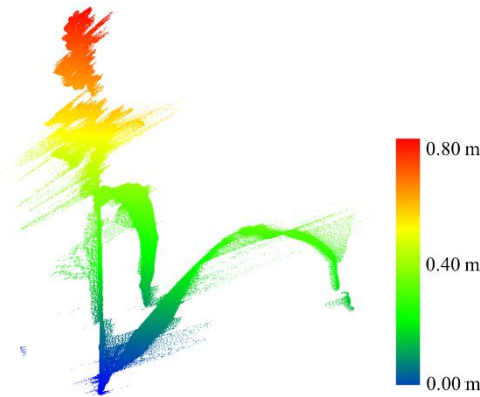


Figure 3.3. Original single sorghum plant collected in the greenhouse

3.3.2.2 Image-based Point Clouds for the Sorghum Training Dataset

A synthetic training set was developed to investigate the use of PointCleanNet for the outlier removal task. Collecting clean LiDAR data over plants in a farm environment without noise and outliers for the purpose of training is difficult and time-consuming, and is only possible at the edge of the field. In this study, the point cloud training dataset was obtained from overlapped RGB images on individual sorghum plants in a greenhouse. The images were acquired of plants at different stages of growth from 4/11/2018 to 5/19/2018 using a Basler piA 2400-17gc camera in a chamber in a controlled environment at the Crop in Silico project facility at the University of Nebraska, Lincoln. A set of images for each plant covered angles 0° , 72° , 144° , 216° , 288° , and a top view. Some datasets also included images at 36° and 216° . A volume carving method was used to generate the point cloud from the resulting images (Scharf et al., 2017; Gaillard et al., 2020). Figure 3.4 shows a sample of the overlapped images and the generated point cloud.



Figure 3.4. Overlapped images acquired for generating point clouds

Thirty-five sets of generated point clouds from images were separated into 28 objects for training, and seven objects were chosen for validation. Outliers were generated as Gaussian noise with a standard deviation of 20% of the shape's bounding box diagonal. The resulting training set had point clouds where 20%, 40, 50%, 70%, and 90% of the points were converted to outliers. To simulate the field scenario, some pairs and triplets of plants with different levels of outliers were joined, then added to the training set. Figure 3.5 illustrates some samples of the dataset.

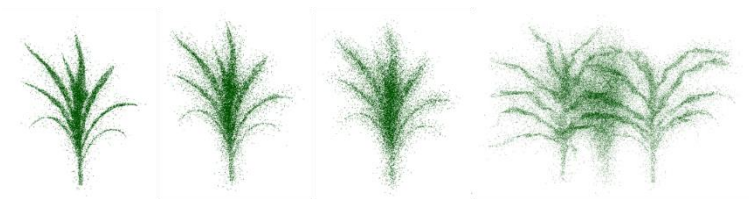


Figure 3.5. Left to right: samples with 20%, 50%, and 70% outliers; three plant grouping

3.3.2.3 LiDAR Remote Sensing Data

Three platforms collected LiDAR in the field for plant breeding related experiments. Two M600P UAVs were flown over the study area at an altitude of 20 and 40 meters and speeds of 3-5 m/s. One UAV was equipped with a Velodyne VLP-Puck Lite and the other with a Velodyne VLP-32C. The Velodyne VLP-Puck LITE has 16 channels that are aligned vertically from -15° to $+15^{\circ}$, thus resulting in a total vertical field of view (FOV) of 30° . The point capture rate in a single return mode is $\sim 300,000$ points per second. The range accuracy is typically ± 3 cm, with a maximum measurement range of 100m (Velodyne VLP-Puck LITE, n.d.). The Velodyne VLP-32C has 32 channels that are aligned vertically from -15° to $+25^{\circ}$, in a total vertical FOV of 40° . The point capture rate in a single return mode is $\sim 600,000$ points per second. The range accuracy is typically ± 3 cm, with a maximum measurement range of 200m (Velodyne VLP-32C, n.d.). The UAVs were equipped with an integrated global navigation satellite system/inertial navigation system (GNSS/INS) Trimble APX-15v3 for direct georeferencing. Data were also acquired by a wheel-based system, a LeeAgra Avenger agricultural high-clearance tractor/sprayer with a custom boom and mounted sensors. It is referred to as the PhenoRover in these experiments. The boom is constructed from T-slot structural aluminium framing with a 2.75 meters width, and the top of the boom can be raised to a maximum of 5.5 meters height from the ground. The sensors mounted on the boom include a Headwall machine vision VNIR hyperspectral camera, an RGB camera, a Velodyne VLP-Puck Hi-Res, as well as a GNSS/INS navigation system. VLP-Puck Hi-Res has a similar sensor specification to the VLP-Puck LITE. Its FOV is -10° to $+10^{\circ}$ (Velodyne VLP-Puck Hi-Res, n.d.). The speed of the platform was 1.5 miles per hour in the field. Figure 3.6 shows the platforms used for the 2020 experiments. Table 3.2 details the UAV platforms and the PhenoRover, and their respective sensor specifications. Table 3.3 summarizes the LiDAR data collection and the corresponding ground reference measurements in terms of Days After Sowing (DAS) relative to the data collection dates and ground reference measurements.



(a) PhenoRover



(b) M600 UAV

Figure 3.6. (a) PhenoRover platform with RGB/LiDAR/Hyperspectral/GNSS/INS sensors, (b) UAV-2 with RGB/LiDAR/GNSS/INS sensors in 2020

Table 3.2. Platforms and mounted sensors specification in 2020

Platform	Sensor	Unit	Description
UAV-1	RGB camera	1	36.4 MP Sony Alpha 7R (ILCE-7R)
	LiDAR sensor	1	Velodyne VLP 16-Puck Lite-range accuracy of ± 3 cm
	GNSS/INS	1	Trimble APX-15 v2
	Hyperspectral camera	1	Nano Hyperspectral (VNIR)
UAV-2	RGB camera	1	36.4 MP Sony Alpha 7R (ILCE-7R)
	LiDAR sensor	1	Velodyne VLP 32-range accuracy of ± 3 cm
	GNSS/INS	1	Trimble APX-15 v2
PhenoRover	RGB camera	2	9.1MP FLIR Grasshopper3 GigE
	Hyperspectral camera	1	Headwall Machine
	LiDAR sensors	1	Velodyne VLP-Puck Hi-Res
	GNSS/INS	1	Applanix POS-LV 125

Table 3.3. LiDAR data and corresponding ground reference data in two experiments with associated DAS in 2020

Experiment	Platform	Flying Height	Sowing Date	LiDAR Data Collection Date	DAS ¹	Ground Reference Date	DAS ²
Maize	PhenoRover	N/A	05/12	06/26	45	06/29	48
	UAV-2	20 m		07/07	56	07/06	55
	UAV-1	20 m		07/11	60	07/13	62
	UAV-2	20 m		07/11	60	07/13	62
	UAV-2	20 m		07/13	62	07/13	62
	PhenoRover	N/A		07/13	62	07/13	62
Sorghum	PhenoRover	N/A	05/13	06/26	44	06/29	47
	UAV-2	20 m		07/07	55	07/06	54
	UAV-2	20 m		07/13	61	07/13	61
	PhenoRover	N/A		07/20	68	07/20	68
	UAV-2	20 m		07/20	68	07/20	68
	PhenoRover	N/A		07/24	72	07/27	75
	UAV-2	20 m		07/28	76	07/27	75

DAS¹: DAS with respect to data collection data; DAS²: DAS with respect to ground reference data

3.4 Methodology

The study included detection and removal of outliers from the experiments conducted in controlled facilities and the field. Data with low noise subsequent to outlier removal are considered as valid points. This section includes descriptions of the geometric approach for outlier removal and the deep learning PointCleanNet method for outlier removal.

3.4.1 Geometric Approach

In Wang and Feng (2015), isolated and non-isolated outliers occur in the point cloud. The nearest neighbors of each point, p , in the defined radius search are determined, and the principal components of the covariance matrix of the k -nearest neighbors are computed to determine curvature. The curvature describes the rate of change of a curve or plane at the chosen point, so a smooth surface has a lower curvature value. Small surface variation indicates that the neighborhood is regular; zero curvature implies a perfect plane. When the curvature values of each

point in the defined neighborhood are calculated, k-means clustering with $k=2$ as noted in Wang and Feng (2015) is applied to the curvature values to separate them into regular points with low curvature and irregular points with high curvature. Pseudo planes and surfaces in the dataset associated with outliers are filtered via thresholding. The remaining regular and irregular points are designated as “good” (gp) and “bad” (bp) points. Points on sharp edges or at the extremum of curved surfaces may be classified as irregular points because of high curvature. Points are excluded via majority voting by regular points (gp_i) in the neighborhood of irregular points (bp) with a radius search of a bp and each regular point (gp_i). This process is continued until all gp_i s vote for bp , resulting in the point cloud being separated into bad points and good points. In the experiments in the current research, not many points were transferred from bp to gp because there are not many sharp surfaces in the point cloud geometry. Figure 3.7 shows the process of the majority voting method.

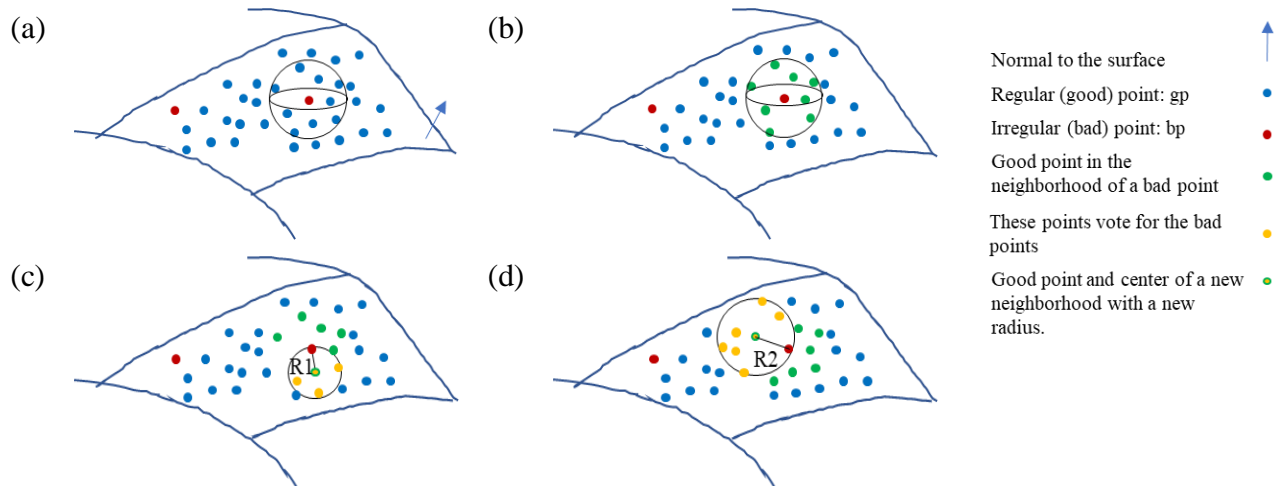


Figure 3.7. Majority voting procedure: (a) create a radius search around each bad point (b) determine the good points within the radius search (c) a new radius search is defined in the center of a good point and a radius of a distance between a good point and corresponding bad point (d) this step is repeated for all good points within a neighbor of bad point

In Wang and Feng (2015), isolated points were removed by checking the intersection of the planes which were created on isolated points. This method can be applied to objects with a solid body. However, it does not perform well on complex objects with separate parts that have many intersecting planes, such as plants. To deal with this issue, we proposed a region growing method

based on the distance between points and k -nearest neighbors (Figure 3.8) to detect and remove the sparse and isolated outlier points remaining in the dataset.

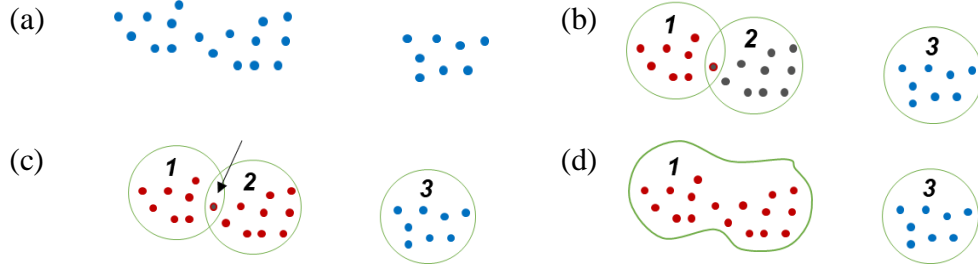


Figure 3.8. Region growing clustering steps: (a) Point cloud. (b) Initial clustering. (c) Finding common points in two close clusters. (d) Connecting and joining two clusters.

The points are structured with a k -d tree data structure, and the k -nearest neighbors to each point are determined within a defined radius. The points are assigned to the clusters based on the nearest neighbors. The clusters with common points are joined, and the cluster number is updated iteratively until no additional changes occur in the clusters. The clusters with fewer points than a specified threshold are removed as isolated outliers, and the remaining clusters are retained. In the end, the remaining points in the dataset are considered inliers. The workflow in Figure 3.9 shows the proposed procedure for outlier removal, with the Wang and Feng (2015) component outlined.

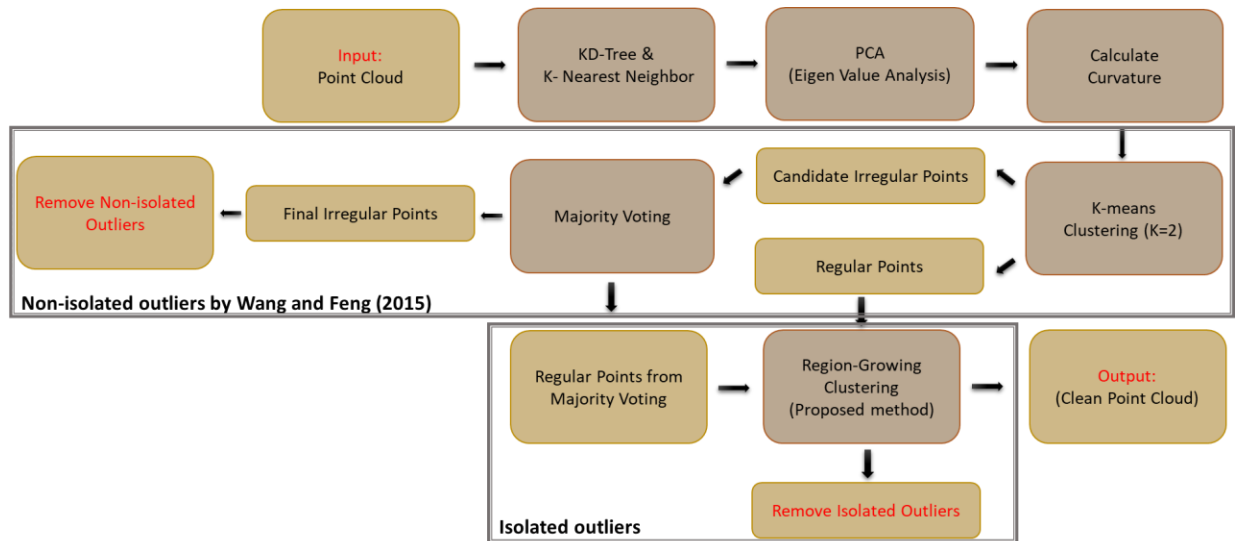


Figure 3.9. The workflow of geometric outlier detection in two steps; non-isolated outliers were removed by the Wang and Feng (2015) method, and isolated outliers were removed by a clustering proposed method

As noted previously, the noise depends on both the characteristics of the system (e.g., platform type and sensor) and the objects being scanned (e.g., geometric complexity and size of the objects). Also, in the geometric approach, some parameters, including best search radius, number of the nearest neighbor points, number of the points in the clusters, and thresholds related to point density and object complexity, are typically obtained by grid search.

3.4.2 PointCleanNet Based Outlier Removal

A deep learning framework may be more effective in removing outliers as the deep learning model trains iteratively using extensive quantities of training data with different types of objects in terms of shape, point density, and percentage of outliers. In this section, PointCleanNet outlier removal is investigated with synthetic data. PointCleanNet input is comprised of patches of points in the dataset. The network is invariant to rotation via the use of the sub-network Spatial Transformer Network (STN), as well as to permutation as it determines the sum of each point's features in the patch. The output is a label for each input point (See Figure 3.1). The network was trained from scratch, and the loss was obtained using an augmented dataset that included the scanned data from a single sorghum plant, two and three joined plants with proportions of 20%, 40%, 50, 70%, 90% as outliers, using the default parameter values. The pre-trained model from (Rakotosaona et al., 2019), which is based on the point clouds of geometric and sculpture objects, was lightly retrained by incorporating the plant data in the input using the default parameters. The loss obtained from the augmented pre-trained network was lower than from the self-trained network due to the limited diversity of the characteristics of the training data associated with the network trained from scratch on the plant data (Figure 3.10).

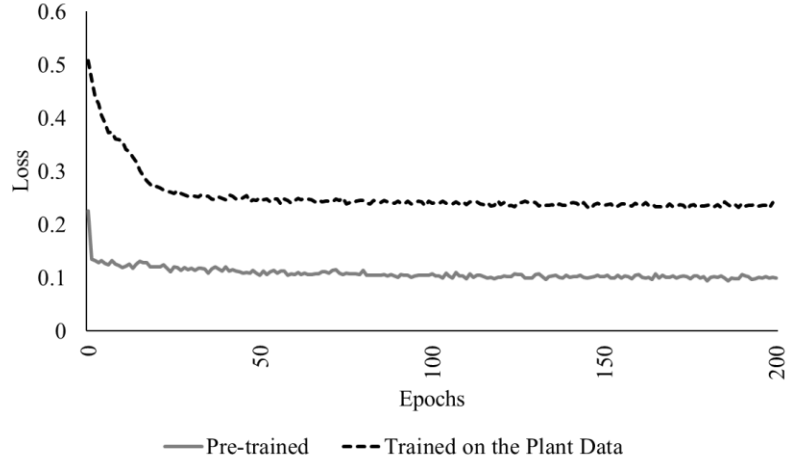


Figure 3.10. Pre-trained vs. the network trained on the plant data loss in 200 epochs (the number of iterations). The loss range is between 0 and 1. If the model's prediction is perfect, the loss is zero

In terms of parameter tuning, the range of learning rate (0.00001 to 0.001 with a step of 10) and patch size (0.01, 0.05, and $0.10 \times$ bounding box) was evaluated using grid search. The default setting had the lowest loss, so the augmented pre-trained model with default parameters was selected as the final model.

The model was evaluated using the LiDAR dataset from the individual greenhouse plant with synthetic outliers and some of the synthetic datasets described in Section 3.3.2. The performance of the approach on these datasets was evaluated using the F_1 -score derived from precision (Eqn. 3.1) and recall (Eqn. 3.2) of the test data; F_1 -score (Eqn. 3.3) has a value between zero and one. Zero indicates a poor result for the F_1 -score if either precision or recall becomes zero. The best result is when there are no false outliers and false inliers in the result, with an F_1 -score of one.

$$Precision = \frac{T_o}{T_o + F_o} \quad (\text{Eqn. 3.1})$$

$$Recall = \frac{T_o}{T_o + F_i} \quad (\text{Eqn. 3.2})$$

$$F_1\text{-score} = 2 \cdot \frac{Precision * Recall}{Precision + Recall} \quad (\text{Eqn. 3.3})$$

where (T_O) is the number of true outliers, (F_O) is the number of outliers including false outliers, and (F_I) is the false inliers. A false inlier is defined as an outlier point that is considered as an inlier by the algorithm.

The methods were also applied to the row crop data obtained from the UAV and PhenoRover platforms. The point density and canopy penetration varied across the platforms due to LiDAR sensor types, the field of view, and mission characteristics (platform height and the overlap of successive strips). In this study, point density is investigated based on flying height and sensor type. Tables 3.4 and 3.5 show the point density of the LiDAR over both fields based on the platform and flying height for the example dates.

Table 3.4. Ground point density for the HIPS maize experiment

Date	Platform	Flying Height	DAS	Point density (Points/ m ²)
7/11/2020	UAV-1	20 m	60	244
7/11/2020	UAV-2	20 m	60	617
7/13/2020	PhenoRover	N/A	62	1500

Table 3.5. Ground point density of sorghum over SbDivTc_Cal sorghum experiment

Date	Platform	Platform Height	DAS	Point density (Points/ m ²)
7/20/2020	UAV-2	20 m	68	500
7/20/2020	PhenoRover	N/A	68	1400

It is extremely difficult to have an appropriate ground reference in row crop data for evaluating the outlier removal methods as many factors can affect the quality of the data, including environmental conditions at the time of data collection, density and arrangement of the plants, and row geometry, as well as the platform and sensor. As a surrogate, the effect of the outlier removal algorithms on an estimated phenotyping parameter was estimated for the various experiments. Here, as noted earlier, the LAI was estimated before and after outlier removal over sorghum and maize experiments and used as the basis of comparison.

3.4.3 LAI Estimation

Geometric features were extracted from row crop LiDAR data, including the Laser Penetration Index (Richardson et al., 2009), Vertical Complexity Index (Pope and Treitz, 2013), Mean height, standard deviation, and skewness (Nie et al., 2016), Cluster Area Plane Index (CAPI), 3rd Quartile of height, Row-level plant volume (rows 2 and 3) within plots (See 2.4.1).

An optical indirect method based on an LAI-2200C plant canopy analyzer was used for ground reference. Empirical models were developed to represent the relationship between ground reference and LiDAR-based features. Predictive models were developed using stepwise multiple regression, partial least squares regression, and support vector regression with a radial basis function (RBF) kernel. The data were randomly sampled as 75% and 25% to training and test sets, respectively, and ten-fold cross-validation was performed on the training set (See 2.4.2). Results obtained for the original data and after outlier removal by the two approaches were evaluated based on the R^2 statistic, and root mean squared error (RMSE) of residuals (Eqns. 3.4 and 3.5).

$$R^2 = 1 - \frac{\sum(y - \hat{y})^2}{\sum(y - \bar{y})^2} \quad (\text{Eqn. 3.4})$$

$$RMSE = [\sum(y - \hat{y})^2 / n]^{1/2} \quad (\text{Eqn. 3.5})$$

where y and \hat{y} denote the LAI ground reference and estimated LAI respectively, \bar{y} is the sample mean of ground reference LAI; the number of samples is denoted by n .

3.5 Results

Results obtained using the geometric method (modified Wang and Feng (2015) method) and the PointClearNet deep learning approach are presented in the following sections for data acquired in the control facilities and the field.

3.5.1 Geometric Outlier Removal from Individual Plants and Field Data

The point cloud obtained by the stationary scanner (see 3.3.2.1) was adequately dense to distinguish the plant structure. As noted in the previous section, outlier removal was achieved

using two steps: removal of irregular points (bad points) connected to the main body of the plant and removal of sparse and isolated outliers. Figure 3.11 shows the original data with outliers and output from the two-step process. The search radius for the nearest neighbors was selected by grid search based on the point density (one centimeter), and the threshold for removing points in a cluster was six. The noise pattern seems to be associated with interference that tends to obscure the main body of the plant. While there is no control on this type of noise, the algorithm was able to remove these points effectively.

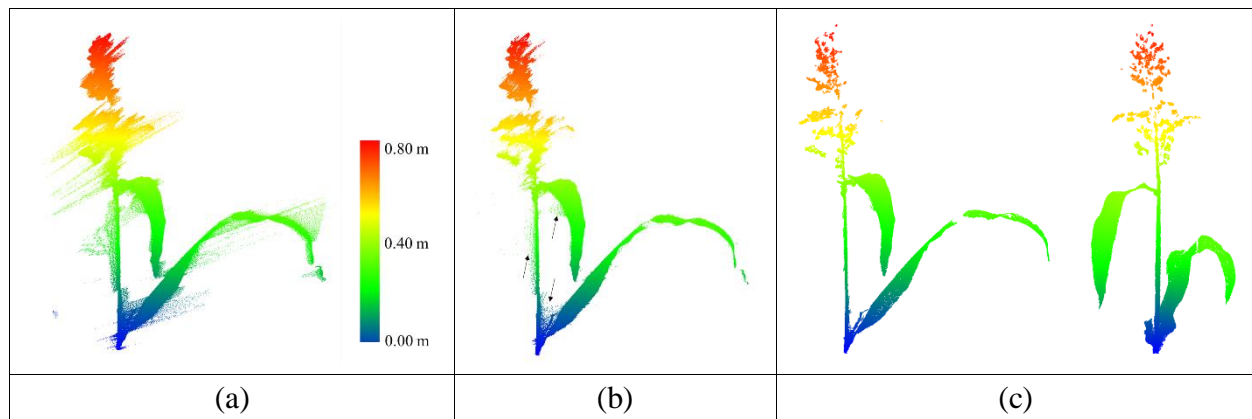


Figure 3.11. (a) Original LiDAR data with natural outliers. (b) Coarse level outlier removal from a sorghum plant. Arrows show the residual outliers from this step (c) Result of removal of residual outliers with two different views

The synthetic datasets were generated from point clouds with three levels of outliers 20%, 50%, and 70%, a radius search of one cm, a cluster size threshold of 6. Three plant groupings with different level of outliers, including (40% - 90% - 40%) and (70% - 90% - 70%) were evaluated using this method, as well with the radius search of two cm and a cluster size threshold of 10 that were selected by grid search for each. Figures 3.12 and 3.13 show the results and F_1 -score of each of the synthetic datasets.



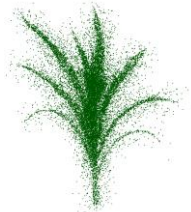

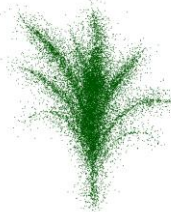
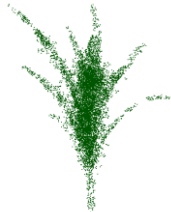
Single plant 20% outliers	Single plant, outliers removed	Evaluation						
		<table><tr><td>Precision</td><td>0.19</td></tr><tr><td>Recall</td><td>0.37</td></tr><tr><td>F₁-score</td><td>0.25</td></tr></table>	Precision	0.19	Recall	0.37	F ₁ -score	0.25
Precision	0.19							
Recall	0.37							
F ₁ -score	0.25							
Single plant 50% outliers	Single plant, outliers removed							
		<table><tr><td>Precision</td><td>0.30</td></tr><tr><td>Recall</td><td>0.39</td></tr><tr><td>F₁-score</td><td>0.34</td></tr></table>	Precision	0.30	Recall	0.39	F ₁ -score	0.34
Precision	0.30							
Recall	0.39							
F ₁ -score	0.34							
Single plant 70% outliers	Single plant, outliers removed							
		<table><tr><td>Precision</td><td>0.74</td></tr><tr><td>Recall</td><td>0.40</td></tr><tr><td>F₁-score</td><td>0.51</td></tr></table>	Precision	0.74	Recall	0.40	F ₁ -score	0.51
Precision	0.74							
Recall	0.40							
F ₁ -score	0.51							

Figure 3.12. Geometric method outlier removal for a synthetic point cloud

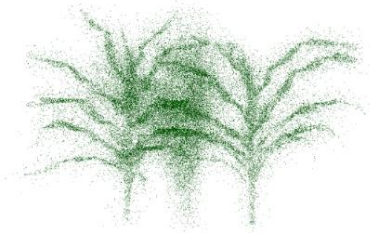
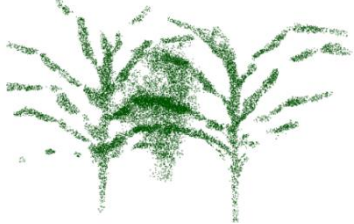
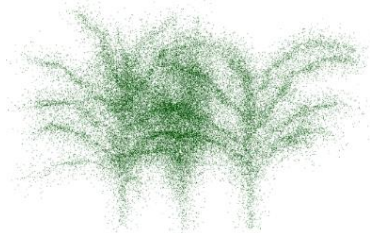
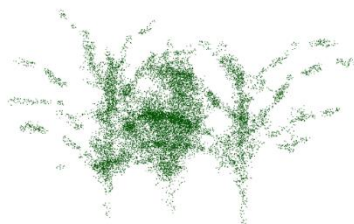
Three plant grouping (40% - 90% - 40% outliers)	Three plant grouping, outliers removed	Evaluation						
		<table><tr><td>Precision</td><td>0.55</td></tr><tr><td>Recall</td><td>0.53</td></tr><tr><td>F₁-score</td><td>0.54</td></tr></table>	Precision	0.55	Recall	0.53	F ₁ -score	0.54
Precision	0.55							
Recall	0.53							
F ₁ -score	0.54							
Three plant grouping (70% - 90% - 70% outliers)	Three plant grouping, outliers removed							
		<table><tr><td>Precision</td><td>0.66</td></tr><tr><td>Recall</td><td>0.47</td></tr><tr><td>F₁-score</td><td>0.55</td></tr></table>	Precision	0.66	Recall	0.47	F ₁ -score	0.55
Precision	0.66							
Recall	0.47							
F ₁ -score	0.55							

Figure 3.13. Geometric method outlier removal on joint three sorghum plants generated point cloud

The precision score for the plant with 20% outliers (0.19) is lower than for the plant with 70% outliers (0.74). The total number of the points is the same in both; the plant with 20% outliers has potentially more false outliers due to having more inlier points (80% inliers).

The method was sensitive to radius search in a local neighborhood, as well as the number of points in the clusters, especially when the randomly distributed outliers were sparse. It is a trade-off between removing points as outliers and preserving points as the main structure of the plant. When precision is low, some true points were considered as outliers and removed, so parts of the plant structure are removed. Similarly, when the recall is low, some outliers remained in the main structure of the plant and were considered as true points. Thus, the gap between the points is smaller, but the number of outliers is larger. Also, when the points are distributed uniformly and are so sparse, the method cannot discriminate the outliers from inliers.

For the HIPS maize experiment, data collected by the PhenoRover and UAV-2 were available. A radius search of 4 cm for the nearest neighbor was selected by a grid search, and the threshold for removing points in a cluster was ten points for PhenoRover data; the radius search and the threshold for UAV data were six centimeters and six points, respectively. The radius search in UAV data is larger than for the PhenoRover data because the UAV point cloud was more sparse than the PhenoRover point clouds. (Figures 3.14 and 3.15).

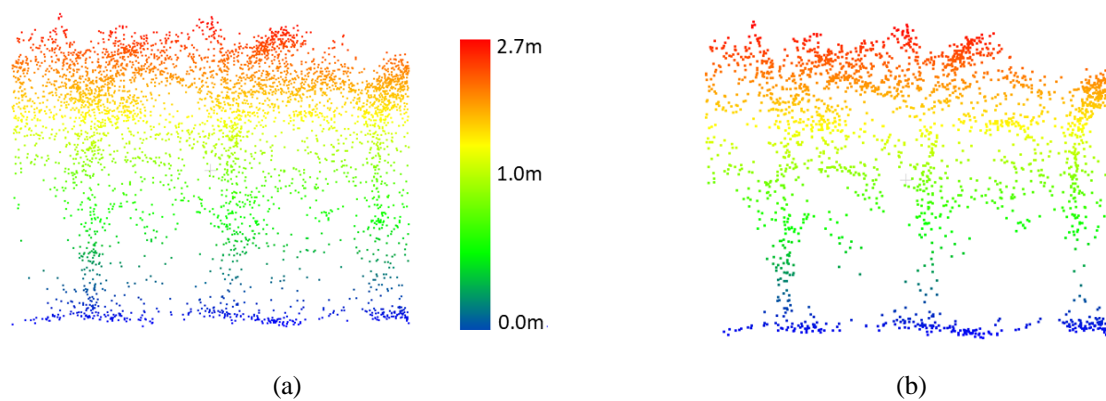


Figure 3.14. UAV-2 LiDAR data of Maize (DAS:60) (a) Original data, (b) Point cloud after outlier removal

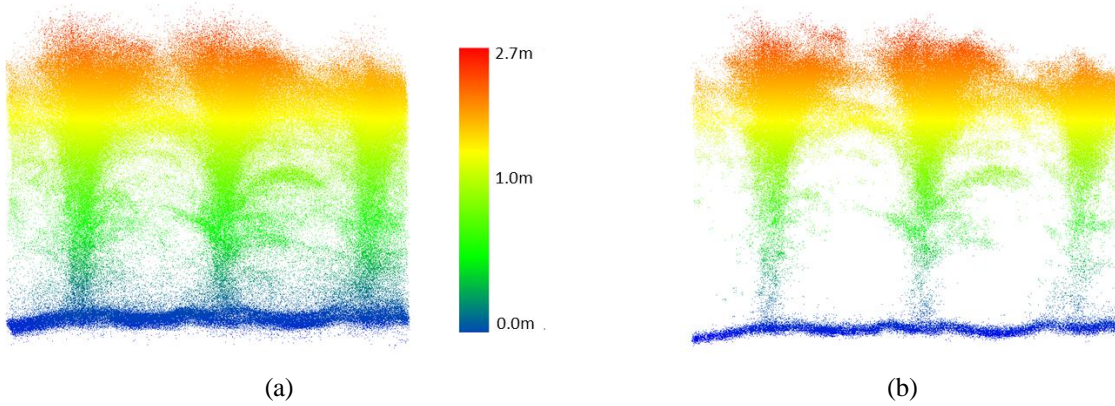


Figure 3.15. PhenoRover LiDAR data over Maize (DAS:62) (a) Original data, (b) Point cloud after outlier removal

The geometric method requires prior knowledge about the data in terms of point density and canopy penetration to select the thresholds, as well as trial-and-error experimentation to finalize the parameters. As shown visually in this section, the proposed geometric approach performed well on greenhouse data, where the plant was isolated from other objects, but the field data were much more difficult to denoise.

3.5.2 PointCleanNet Outlier Removal from Individual Plants and Field Data

The PointCleanNet method was applied to the point cloud single plants contaminated with multiple levels of outliers and investigated for row plants of sorghum and maize. The results obtained for both datasets are described and evaluated in this section.

3.5.2.1 Single Plants

First, the dataset of the single sorghum plant from the greenhouse contaminated with different levels of Gaussian outliers and used to evaluate the PointCleanNet based on the F_1 -score. The red points are outliers generated for each dataset (Figure 3.16).



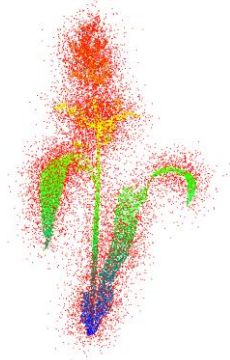

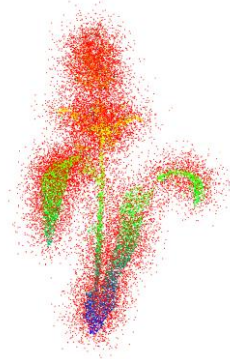

Single plant 20% outliers	Single plant, outliers removed	Evaluation						
		<table><tr><td>Precision</td><td>0.81</td></tr><tr><td>Recall</td><td>0.87</td></tr><tr><td>F₁-score</td><td>0.84</td></tr></table>	Precision	0.81	Recall	0.87	F ₁ -score	0.84
Precision	0.81							
Recall	0.87							
F ₁ -score	0.84							
Single plant 50% outliers								
		<table><tr><td>Precision</td><td>0.95</td></tr><tr><td>Recall</td><td>0.74</td></tr><tr><td>F₁-score</td><td>0.83</td></tr></table>	Precision	0.95	Recall	0.74	F ₁ -score	0.83
Precision	0.95							
Recall	0.74							
F ₁ -score	0.83							
Single plant 70% outliers								
		<table><tr><td>Precision</td><td>0.97</td></tr><tr><td>Recall</td><td>0.58</td></tr><tr><td>F₁-score</td><td>0.73</td></tr></table>	Precision	0.97	Recall	0.58	F ₁ -score	0.73
Precision	0.97							
Recall	0.58							
F ₁ -score	0.73							

Figure 3.16. outlier removal on individual plant LiDAR

After removal of the three levels of outliers, the structure of the plant is detectable, and especially for the 20% and 50% experiments. However, when the outliers are 70% of the data for the single plant, the recall dropped significantly.

Datasets obtained from the generated point clouds were evaluated, and the F₁-score evaluated for the multiple scenarios (Figures 3.17 and 3.18).



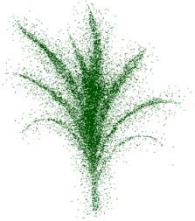

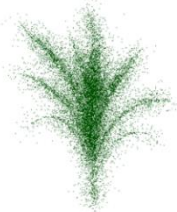

Single plant 20% outliers	Single plant, outliers removed	Evaluation						
		<table><tr><td>Precision</td><td>0.63</td></tr><tr><td>Recall</td><td>0.77</td></tr><tr><td>F₁-score</td><td>0.70</td></tr></table>	Precision	0.63	Recall	0.77	F ₁ -score	0.70
Precision	0.63							
Recall	0.77							
F ₁ -score	0.70							
Single plant 50% outliers								
		<table><tr><td>Precision</td><td>0.79</td></tr><tr><td>Recall</td><td>0.80</td></tr><tr><td>F₁-score</td><td>0.79</td></tr></table>	Precision	0.79	Recall	0.80	F ₁ -score	0.79
Precision	0.79							
Recall	0.80							
F ₁ -score	0.79							
Single plant 70% outliers								
		<table><tr><td>Precision</td><td>0.86</td></tr><tr><td>Recall</td><td>0.82</td></tr><tr><td>F₁-score</td><td>0.84</td></tr></table>	Precision	0.86	Recall	0.82	F ₁ -score	0.84
Precision	0.86							
Recall	0.82							
F ₁ -score	0.84							

Figure 3.17. PointCleanNet outlier removal for a point cloud based on a single plant

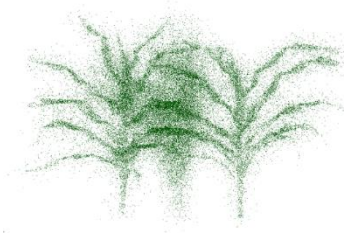
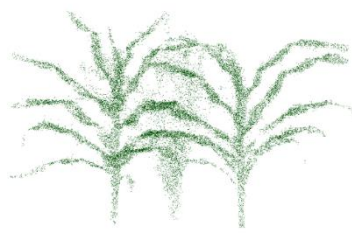
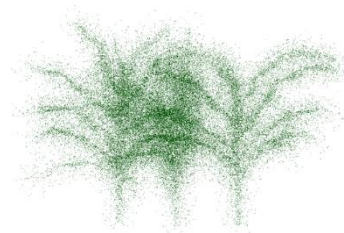
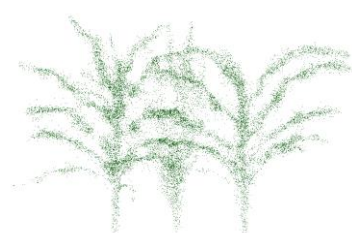
Three plant grouping (40% - 90% - 40% outliers)	Three plant grouping, outliers removed	Evaluation						
		<table><tr><td>Precision</td><td>0.82</td></tr><tr><td>Recall</td><td>0.78</td></tr><tr><td>F₁-score</td><td>0.80</td></tr></table>	Precision	0.82	Recall	0.78	F ₁ -score	0.80
Precision	0.82							
Recall	0.78							
F ₁ -score	0.80							
Three plant grouping (70% - 90% - 70% outliers)								
		<table><tr><td>Precision</td><td>0.80</td></tr><tr><td>Recall</td><td>0.78</td></tr><tr><td>F₁-score</td><td>0.79</td></tr></table>	Precision	0.80	Recall	0.78	F ₁ -score	0.79
Precision	0.80							
Recall	0.78							
F ₁ -score	0.79							

Figure 3.18. PointCleanNet outlier removal on joint three sorghum plants generated point cloud

The F_1 -score value from the individual plant with 70% outliers (0.84) is higher than the value from the plant with 20% outliers (0.70). This is because the number of false outliers in the 20% outlier case results in the value of precision of the plant with 20% outliers lower than the plant with 70% outliers. The total number of the points in both datasets are the same; the plant with 20% outliers has more inliers (80%), which causes the higher value of false outliers. The two sets of three plant grouping with different levels of outliers have a similar F_1 -score (0.79 and 0.80). The level of the outliers is high in the middle plant, and its structure is not detectable, while the structure of the plants on the side is completely detectable as the level of the outliers is lower. Comparing deep learning results with geometric results, it is clear that there are some missing parts of leaves in the geometric approach, while in the deep learning method, the leaves are complete and are visible.

3.5.2.2 Outlier Removal from Maize and Sorghum Field Data

As noted previously, field data are planted densely (maize ~75,000 plants/hectare vs. sorghum ~200,000 plants/hectare) in multiple row plots, and the canopy closes between the rows as the growing season progresses. Figures 3.19-3.22 show selected multi-row subsets of plots where outliers were removed from UAV-1, UAV-2, and PhenoRover data.

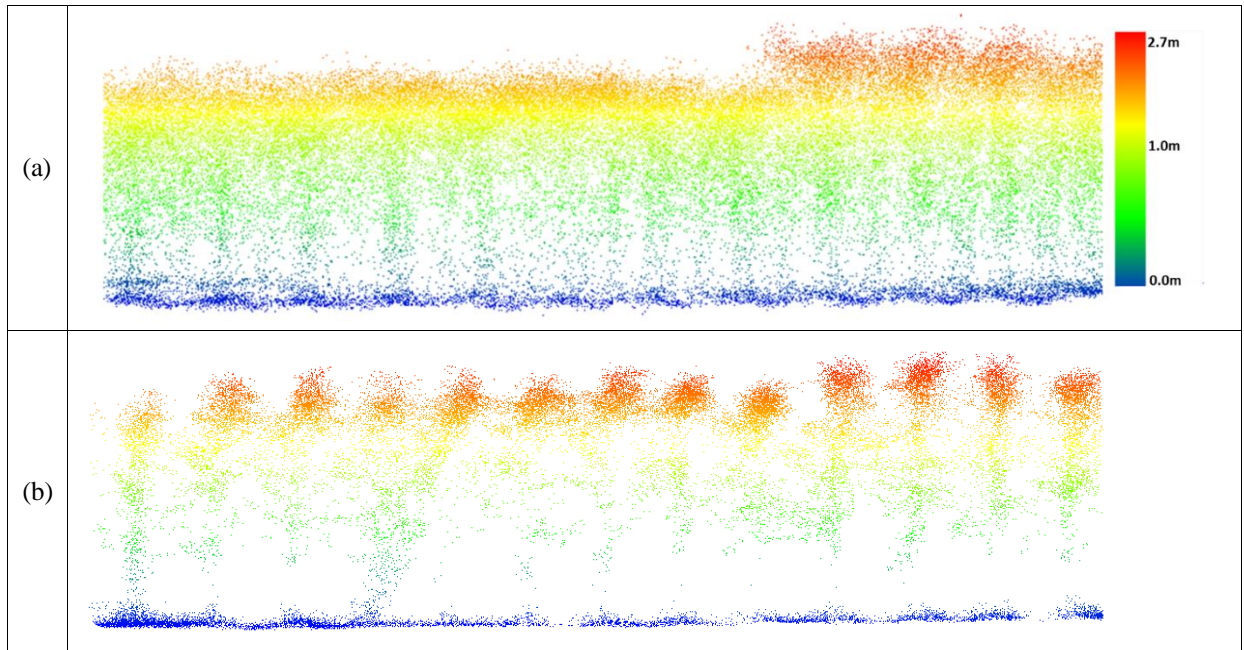


Figure 3.19. Data from UAV-1 at 20 m altitude over maize (DAS: 60) (a) original data (b) outlier removal with PointCleanNet

When the UAV-1 acquired data at 20 m altitude with a VLP-Puck Lite (16 channels), penetration through the canopy was inadequate to identify the structure of plants beneath the top layer of the canopy, and plants from which outliers had been removed did not provide additional information (Fig. 3.19)

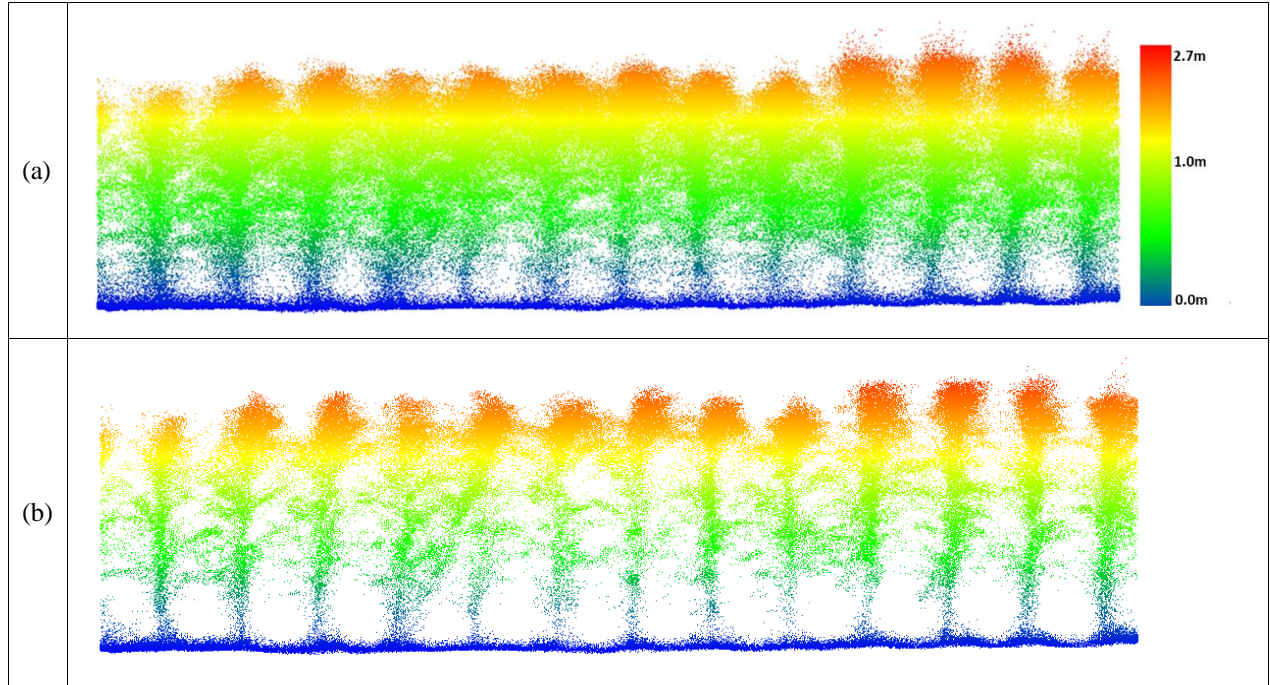


Figure 3.20. Data UAV-2 at the altitude of 20 m over maize (DAS: 60) (a) original point cloud perpendicular to the direction of the rows; (b) results of outlier removal using PointCleanNet

The sample result in Fig. 3.20 shows that the method removed outliers from UAV-2 data flying at 20 m, while many structure-related points were retained below the canopy. The resulting plant structure is more complete than the UAV-1 output shown in Figure 3.19. These results, while limited, indicate that significant increases in penetration are achieved at 20m flying height, and that the VLP-32C has significantly better penetration than the 16 channel VLP-Puck Lite under these conditions.

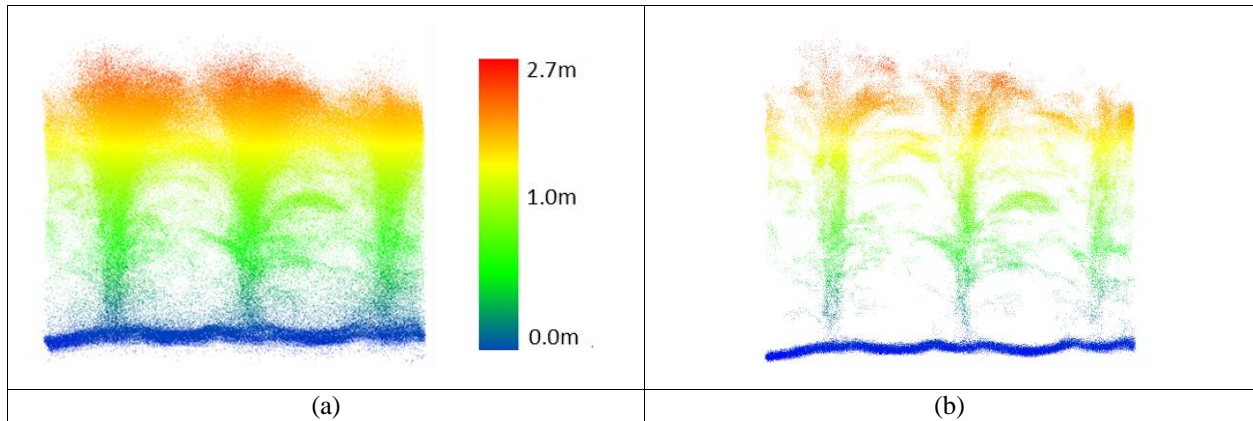


Figure 3.21. PhenoRover LiDAR data of maize (DAS:62) (a) Original data, (b) Outlier removal PointCleanNet

While the PhenoRover point cloud data were more dense, there are additional sources of outliers, including the vibration of the boom and interaction of the platform with the plants. The method removed some outliers but also removed some of the actual plant structure, although significant structure of the maize canopy was retained after denoising. The percentage of the removed points over maize was approximately 35% to 45% of UAV data and 25% to 30% of PhenoRover data. Figure 3.22 shows a sample of sorghum data collected by UAV-2 flown at the altitude of 20 m.

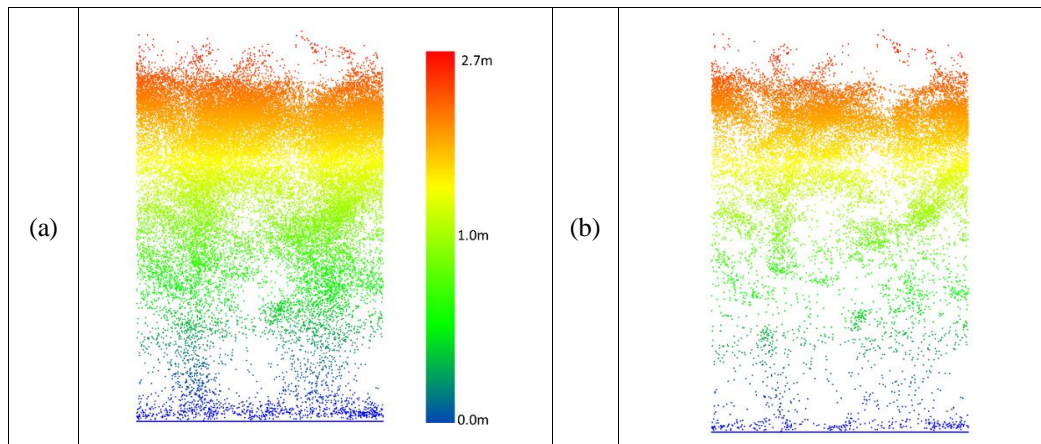


Figure 3.22. UAV-2 LiDAR data of sorghum (DAS:68) (a) Original data, (b) Outlier removal PointCleanNet

Due to the complexity and density of sorghum, the point clouds remaining after denoising did not characterize the structure of the individual plants well. The percentage of the removed points over sorghum was approximately 40% to 50% of UAV data and 30% to 35% of PhenoRover data.

In the deep learning method, when the plants (greenhouse and field) had very similar characteristics, and samples from all the cases were considered in the training set, there was no need to change any parameters when the shape, point density, and percentage of outliers varied within the bounds of these parameters. Although the results of synthetic plants from geometric and PointCleanNet methods are visually similar, PointCleanNet denoising yielded better results based on the F_1 -score (e.g., 0.25 vs. 0.70 for 20% outliers on single plant). Therefore, the PointCleanNet method was applied to all the plots in the field data (maize and sorghum) to remove the outliers, and the impact was evaluated based on estimated LAI. The results are discussed in section 3.5.3.

3.5.3 Impact of PointCleanNet Outlier Removal method on LAI Estimation

The impact of outlier removal for both the UAV-2 (VLP-32C) flown at 20m and PhenoRover data acquired over sorghum and maize fields is illustrated in this section relative to LAI (Figure 3.23).

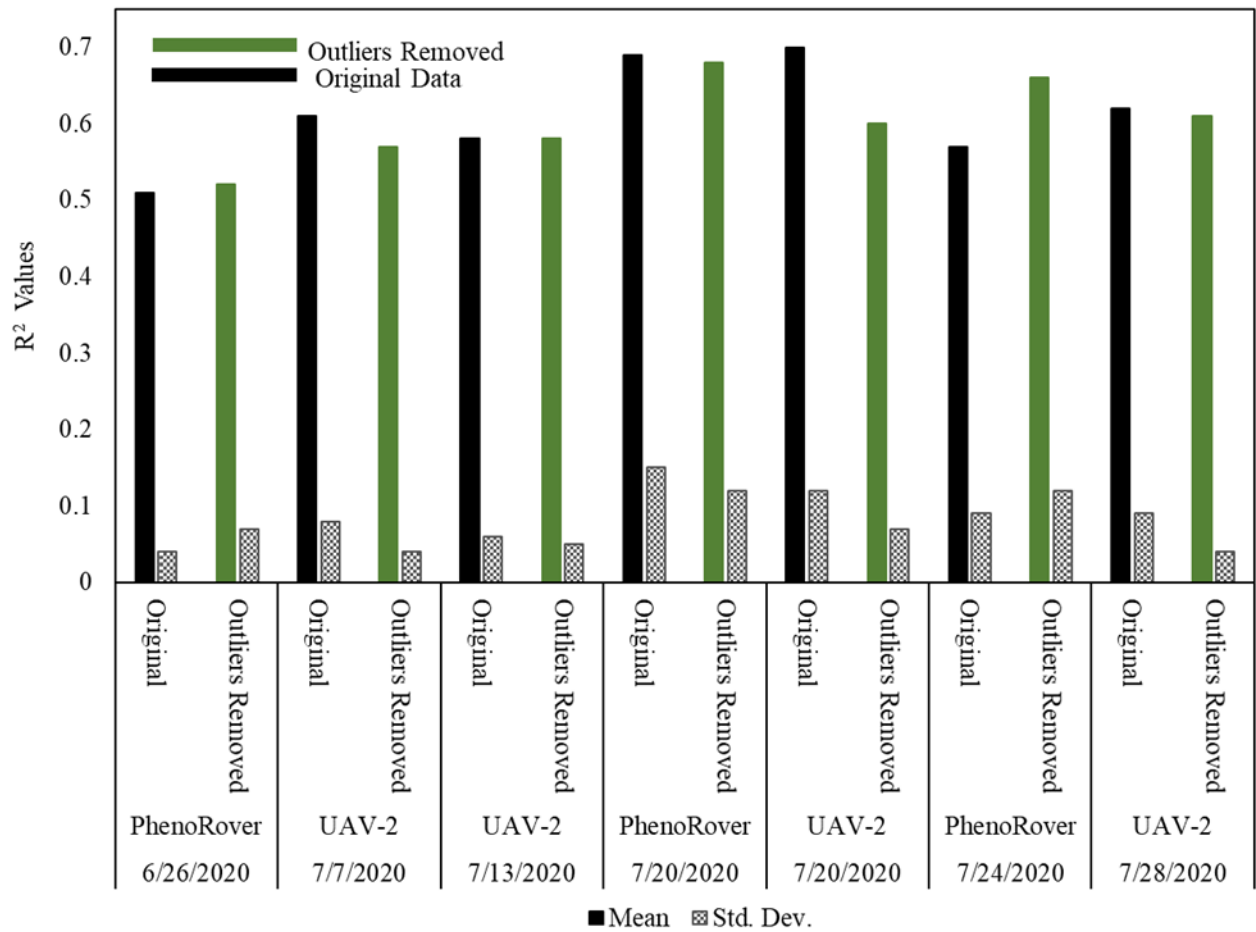


Figure 3.23. Estimates of LAI for original data and after PointCleanNet based outliers removed from data acquired by the UAV and Phenorover

The impact of outlier removal on estimates of LAI was investigated for data acquired by UAV-2 and the Phenorover data using an SVR model with an RBF kernel. The mean and standard deviation of the respective R^2 values are shown in the bar chart in Figure 23. After removing outliers from data (from which the photoperiod sensitive varieties had been removed as discussed in Ch 2), the R^2 value of the model increased for the Phenorover for both 6/26/2020 and 7/24/2020 and was slightly lower for 7/20. The standard deviation of the estimated R^2 value was inconsistent for the Phenorover. The impact of outlier removal was larger on 7/24/2020 in part because that day was windy (about 2.5 m/s) compared to other days with lower wind speed. Figure 24 shows a sample plot of estimated LAI vs. the ground reference for 7/24/2020 Phenorover data. In addition to improving the R^2 value, the RMSE decreased slightly after outlier removal.

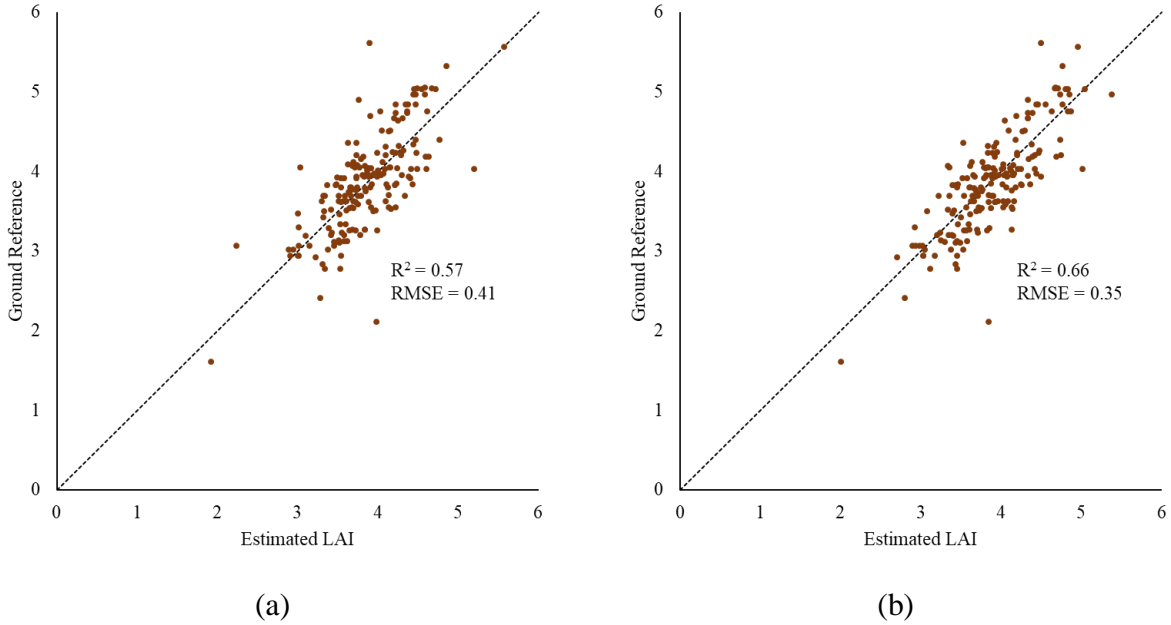


Figure 3.24. Plot of estimated LAI vs. ground reference (a) original and (b) with outliers removed from PhenoRover data (7/24/2020) using PointCleanNet method

The results showed that the effect of outliers on PhenoRover data is higher than the UAV data based on the R^2 value improvement after outlier removal. The R^2 values for resulting from denoising the UAV data decreased, but the standard deviation of R^2 was also reduced. This implies that outlier removal reduced the anomalous data in terms of improving the LAI estimation, but that useful points were also removed. Overall, t-tests of the improvement related to the impact of outlier removal indicated that the change was not statistically significant at the 95% level (p -value = 0.79) based on the sample mean of R^2 .

The impact of the PointCleanNet outlier removal algorithm was also evaluated on maize field data (HIPS) from UAVs at a flying height of 20 m and for the PhenoRover data (Figure 3.25).

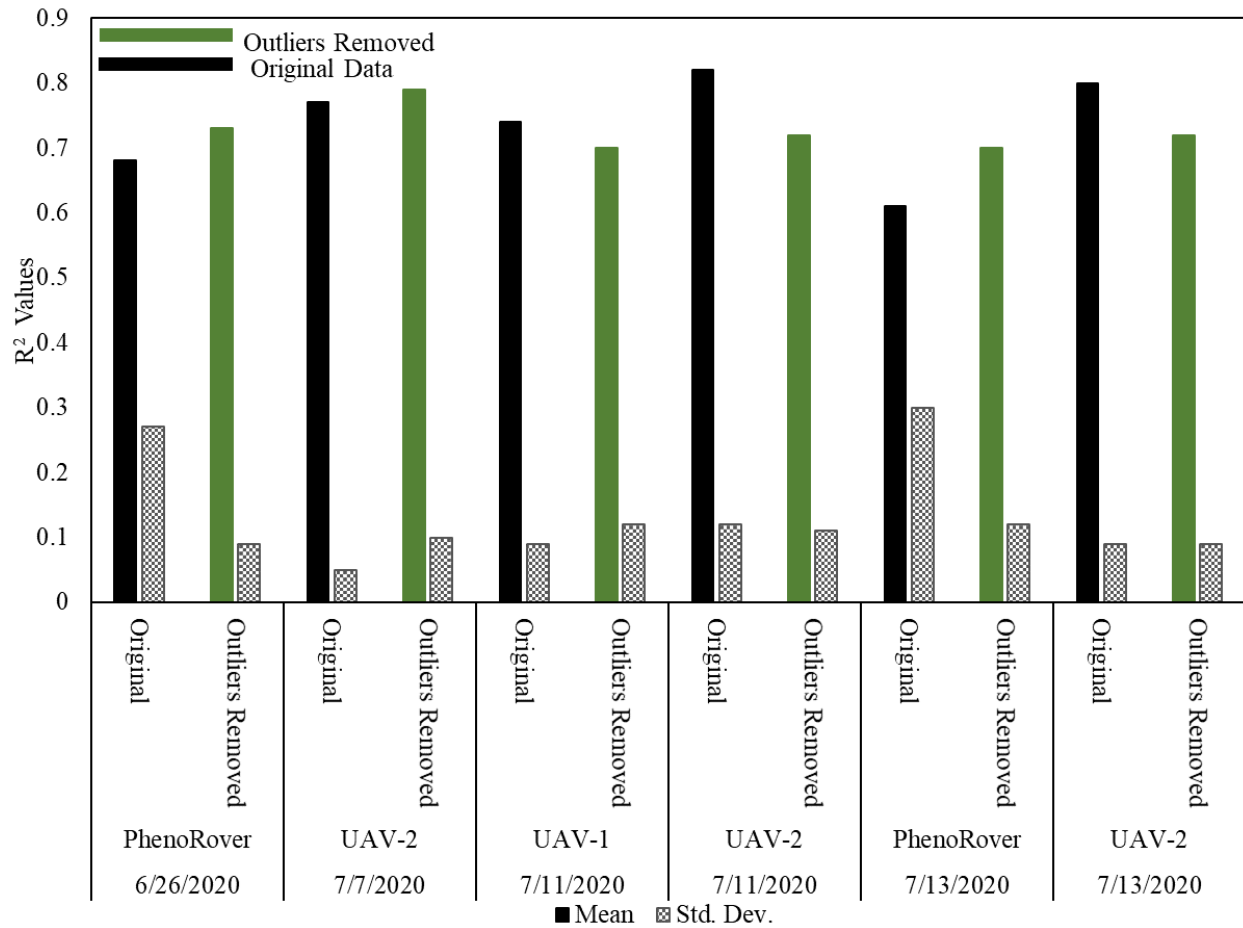


Figure 3.25. Maize LAI estimation on original and datasets with PointCleanNet outliers removed during the growing season on UAV and PhenoRover

The bar chart in Figure 3.25 shows that the R^2 value of the maize LAI predictions based on the three platforms was generally higher than for sorghum (e.g., values vary between 0.61 and 0.82 while R^2 values of sorghum LAI estimation varied from 0.51 to 0.70). The models based on data from which outliers had been removed by PointCleanNet had higher R^2 values for PhenoRover datasets (e.g., on July 13th R^2 value was improved from 0.61 to 0.70). The R^2 values from the original data also have a higher standard deviation of R^2 compared to the values for the UAV datasets. Similar to the sorghum models, the outliers did not have a significant impact on the LAI estimates for the UAV-based models. Although the maize is planted at a lower density, and the plant canopy is somewhat more open, the point density and penetration were still significantly lower for the UAVs than the PhenoRover. The p -value (0.78) of the t-test statistic indicates that

the impact of the outlier removal method was also not statistically significant for maize at the 95% level for either the UAV-2 or the PhenoRover.

3.6 Summary and Conclusions

In this chapter, a geometric method and a deep learning-based approach (PointCleanNet) for outlier removal were investigated on a greenhouse plant and image-based point clouds plants. The impact of outlier removal was also investigated for plants grown in field plots. For the geometric method, outliers were categorized as non-isolated or isolated; non-isolated outliers were removed by the Wang and Feng (2015) algorithm, and isolated outliers were removed by extending this method. The geometric method requires specification of input parameters, including radius search and number of points in a neighborhood of a point of interest. These parameters were sensitive to the distribution and density of the points in the dataset. When a platform is stationary, and the distribution of the points is uniform through the dataset, as in the example of the single plant in this study, finding the parameters is straightforward, as the density of points is adequate to detect the outliers. When the platform moves, the points are distributed sparsely. Coupled with the irregular shape of the objects, it is challenging for this method to remove the outliers. When the method was applied to maize and sorghum datasets acquired from UAVs and the PhenoRover wheeled vehicle, the geometric method did not perform well due to the extreme sparsity of points deeper in the canopy. In the maize dataset, the structure of the plants became more clear and could be detected visually from both platforms. Although some outliers were removed from the sorghum dataset, the plant structure was not recognizable after outlier removal. This implies that the sparsity of the points in the datasets was a significant problem for this outlier removal approach.

The PointCleanNet deep learning framework was investigated for removing outliers from image-based point clouds derived from images in greenhouses and for field data. . When the model was retrained using point clouds generated from overlapped images that were contaminated with different levels of simulated outliers, the loss was lower than when the model was trained solely on point clouds from plants. Based on the F-score, the network successfully removed different levels of outliers in the greenhouse data. PointCleanNet was also applied to both maize and sorghum data from field experiments, where the outliers included the impact of the complex plant structure and the movement of the platforms. LAI was estimated over field plots before and after PointCleanNet outlier removal using the sorghum and maize data from both platforms. The

changes in the R^2 values of the models were not statistically significant improvement based on t-test results. This may in part be due to the fact that LAI is based on gap fraction, which relates to the distribution of points through the vertical space, not to overall structural characteristics, which had been improved by denoising, based on visualization. Although the p -values from t-test statistics (sorghum:0.79, maize:0.78) indicated that there is not a significant difference between results prior to and after outliers are removed, the R^2 values of estimated LAI from the PhenoRover improved both in terms of increasing the sample means and decreasing the standard deviations of R^2 (e.g., sorghum on 7/24/2020 before 0.57 and after 0.66). Based on these experiments, removal of outliers based on PointCleanNet appears to be justified for plant structures in greenhouses and for field data when the point density is greater than ~ 600 points per m^2 , as was the case for the low altitude UAV and PhenoRover acquisitions where canopy penetration was higher. It may also be useful for denoising LiDAR data acquired from a gantry. An indoor gantry would be close to the plants but would not interfere with them or be subject to the weather. An outdoor gantry would provide an “intermediate” platform which would have improved penetration but not be subject to interference with the plants. It should be noted that the outlier removal may prove more effective for applications related to extraction of specific geometric features such as the number of leaves, leaf angle, etc.

4. ESTIMATION LEAF AREA INDEX BY DEEP LEARNING-BASED FEATURE EXTRACTION FROM DISCRETE RETURN LIDAR DATA OVER AGRICULTURAL ROW CROPS

4.1 Abstract

Leaf Area Index (LAI) is an important phenotyping variable but is difficult to estimate over agricultural row crops using either direct and indirect methods. Direct methods are laborious and time-consuming, while indirect methods such as remote sensing-based approaches have multiple sources of uncertainty. LiDAR (Light Detection and Ranging) remotely sensed data acquired from manned aircraft and UAVs' have been investigated to estimate LAI based on physical/geometric features such as canopy gap fraction. The quality of the extracted features depends on the point density and laser penetration through the canopy. Deep learning frameworks are increasingly being used in remote sensing applications for prediction. In this chapter, the PointNet based AutoEncoder is investigated for feature extraction from LiDAR data acquired by UAV platforms over sorghum and maize plant breeding experiments. LAI estimates based on these inputs were used to develop support vector regression (SVR) models using plant canopy analyzer data as the ground reference. Results were compared to models based on estimates from physically-based features and evaluated in terms of the coefficient of determination (R^2). The effects of experimental conditions, including flying height, sensor characteristics, and crop, were also investigated relative to the estimates of LAI.

4.2 Introduction

Leaf area index (LAI) is defined as the leaf area per unit area projected on the ground. It is an important biophysical crop variable that provides information about plant structure for a wide range of agricultural applications, including plant breeding, management of cropping systems, and crop modeling (Jonckheere et al., 2004; Apolo-Apolo et al., 2020). LAI can be obtained by both direct and indirect methods. Indirect methods, including those that utilize optical remote sensing data, are based on the canopy gap fraction and allometric relationships estimated using empirical regression models. The ground reference for optical methods is provided by plant canopy analyzers focused on effective LAI (Fang et al., 2019).

LiDAR is an active sensing technology, which provides a point-wise 3-dimensional (3D) representation of objects (Estrada et al., 2017). Its usage has increased in precision agriculture for estimation of crop phenotypes, such as height (Ravi et al., 2018; Li et al., 2020), LAI (Nie, Wang, Dong, Xi, et al., 2016b), and biomass (Masjedi et al., 2020), as it can provide information related to the vertical structure of vegetation (Korhonen et al., 2011). The primary features extracted from the LiDAR point cloud data are related to either the canopy gap fraction or statistical moments of the distribution of points in the canopy (Fang et al., 2019). Canopy gap fraction features, such as the laser penetration index (LPI), are based on the proportion of points that penetrate the canopy (Pope & Treitz, 2013b; Alonzo et al., 2015; Nie, Wang, Dong, Xi, et al., 2016b). Allometric relationships are typically based on features derived from the statistical moments of the vertical distribution of points (e.g., the mean, standard deviation, and skewness of the height) (Richardson et al., 2009; Zhao & Popescu, 2009; Peduzzi et al., 2012; Nie, Wang, Dong, Xi, et al., 2016b). Other features investigated in the literature based on the point distribution include the vertical complexity index (VCI) (van Ewijk et al., 2011b) and the cluster area plane index (CAPI), which are both described in Chapter 2. To extract these features, preprocessing and analysis are required, including classification of points as ground and nonground points and determining the point density related to laser penetration through the canopy over a given area. A method of feature extraction that is simply derived from the pattern of the input data would be desirable and potentially more robust.

Recently, applications of deep learning have increased, including in remote sensing. Deep learning is now widely applied to image-based problems, including target recognition, pixel-based classification, and feature extraction (L. Zhang et al., 2016). Lately, end-to-end processing, including deep learning and machine learning for point cloud data analysis, has become an area of interest to researchers (Charles R. Qi et al., 2016; Ge et al., 2018; Poux & Billen, 2019; X. Cheng et al., 2019; Apolo-Apolo et al., 2020; Guo et al., 2020; van Klompenburg et al., 2020). The majority of current deep learning architectures, especially convolutional neural networks (CNN), are not designed to be utilized with unstructured data or irregular point clouds. The point clouds are typically sorted into 3D voxels before being input to the network (Boulch & Marlet, 2016; Poux & Billen, 2019). This approach has drawbacks, including loss of spatial information, because preservation of geometry depends on the voxel size. Having an architecture that can directly use an irregular point cloud would be preferable. For example, the PointNet (Charles R. Qi et al., 2016)

architecture provides the capability for taking unstructured point clouds as input and utilizing one subnetwork for classification and the other for segmentation. Researchers have investigated PointNet (Charles Ruizhongtai Qi et al., 2017; Guerrero et al., 2018a; Charles R. Qi et al., 2018; Rakotosaona et al., 2019; Aoki et al., 2019) to address classification, outlier removal, and segmentation problems. Kohara and Nakazawa (2019) extracted features using the PointNet AutoEncoder to reduce the dimensionality of the input data. The PointNet AutoEncoder (Charles R. Qi, 2018/2020) is based on PointNet in the encoder portion of the network and fully connected layers in the decoder portion (Figure 4.1). It extracts global features from n input points and converts them to n output points using its decoder. Kohara and Nakazawa (2019) used the PointNet AutoEncoder to extract features from a single laser range finder and applied a support vector machine (SVM) with a radial basis function kernel (RBF) for body part detection (Kohara & Nakazawa, 2019).

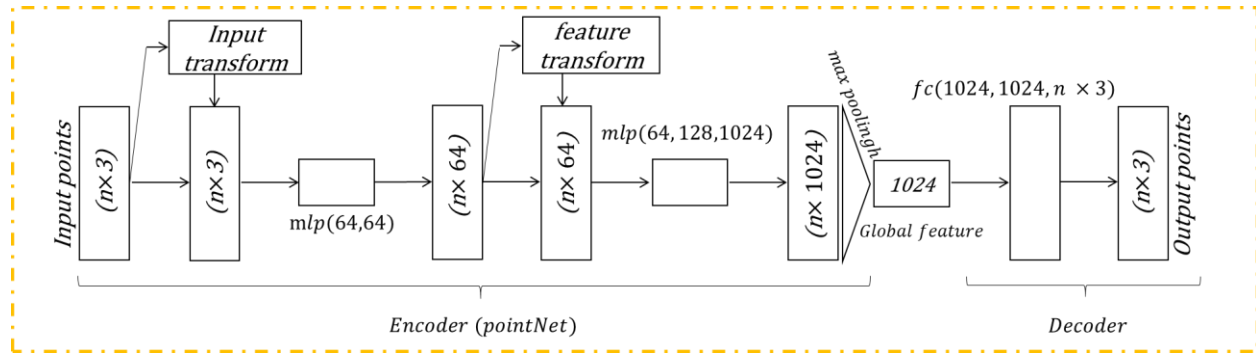


Figure 4.1. PointNet Autoencoder architecture: the encoder part is PointNet, and the decoder is a fully connected network (FNN). The input of the network is all points in the dataset, and the output is the reconstructed input (Charles R. Qi, 2018/2020).

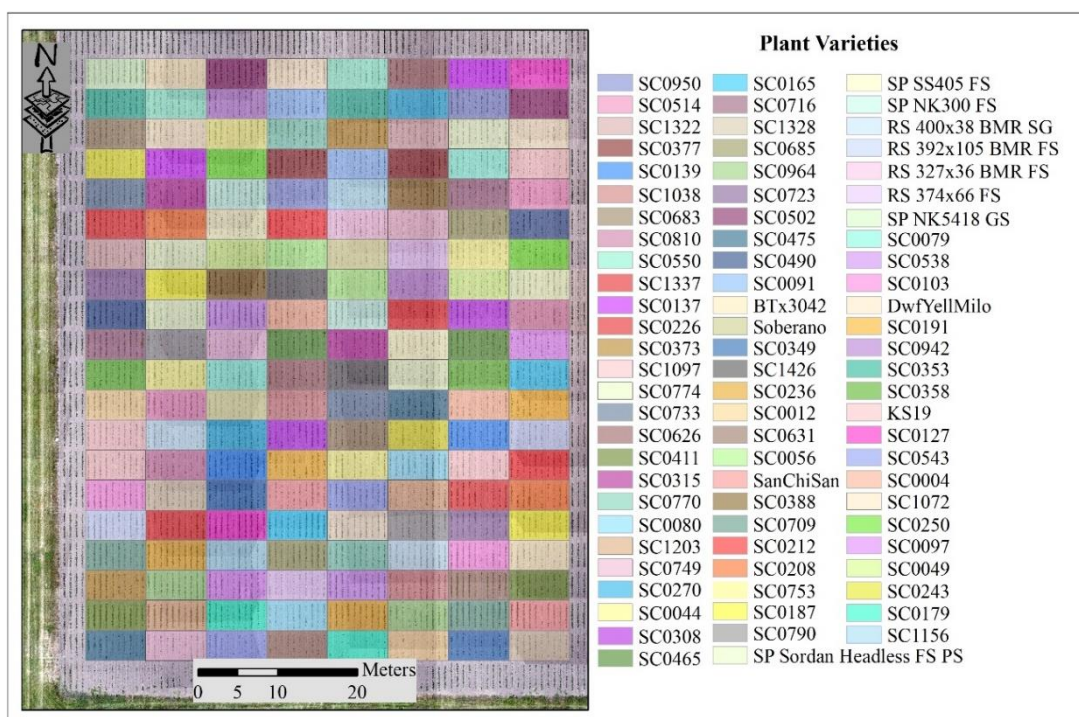
In this chapter, we investigate using PointNet AutoEncoder feature extraction instead of physical/geometric features to estimate LAI using LiDAR data acquired by UAV platforms over sorghum and maize field trials. A support vector regression (SVR) model with an RBF kernel is used to estimate LAI based on the extracted features and plant canopy analyzer-based reference data. The results are compared to those obtained using physical features based on the R^2 value of the model. To our knowledge, this is the first application of the PointNet Autoencoder to plants, whose complex geometry is difficult to characterize.

4.3 Materials

4.3.1 Experimental Setting

The experiments for this study were conducted in two fields containing test plots of sorghum and maize at the Agronomy Center for Research and Education (ACRE) at Purdue University, West Lafayette, Indiana, USA. LiDAR data were acquired during the 2020 growing season over the Sorghum Biodiversity Test Cross Calibration Panel (SbDivTc_Cal) and the maize High-Intensity Phenotyping Sites (HIPS). The planting density for sorghum was ($\sim 200,000$ plants/hectare), and ($\sim 75,000$ plants/hectare) for maize. The SbDivTc_Cal experiment contained two replicates of 80 varieties in a randomized block design (plot size: $7.6\text{m} \times 3.8\text{m}$), ten rows per plot. The HIPS experiment contained two replicates of 44 varieties. (plot size: $1.5\text{m} \times 5.3\text{m}$), two rows per plot. Figure 4.2 shows the layout of the plots over SbDivTc_Cal and HIPS in 2020 based on the respective genotypes. Table 4.1 summarizes the field information for the experiments.

(a)



(b)

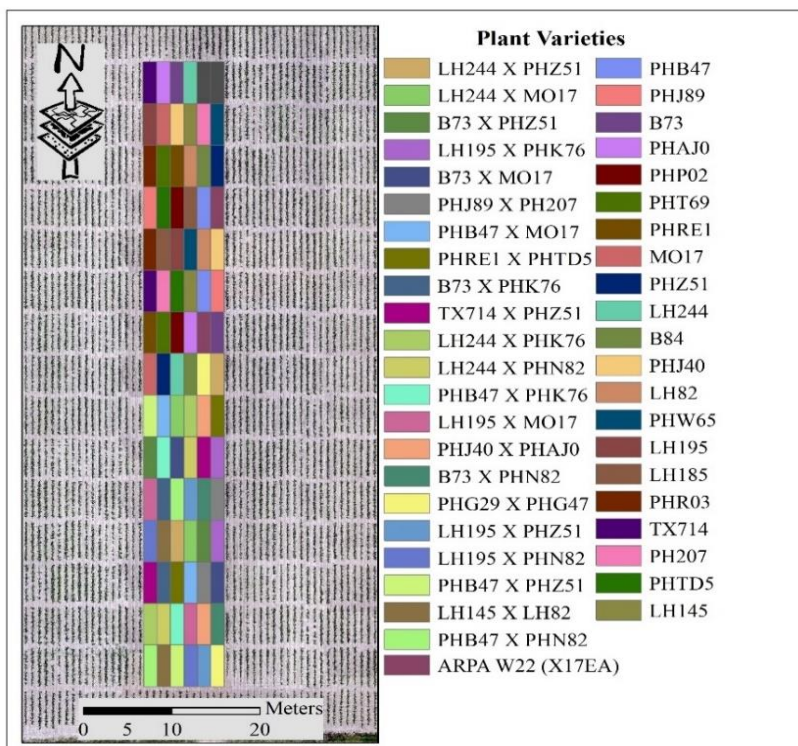


Figure 4.2. Plot variety layout for 2020 (a) SbDivTc_Cal panel and (b) HIPS experiments.

Table 4.1. Experimental design for the 2020 growing seasons

Experiment	# of plots	# of rows	# of varieties	Sowing Date	Harvest Date
HIPS	88	2	44	May 12	October 1
SbDivTc_Cal	160	10	80	May 13	August 15

4.3.2 Experimental Data

4.3.2.1 LiDAR Point Cloud Data Acquisition

Two M600P UAVs equipped with a Velodyne VLP-Puck Lite and a Velodyne VLP-32C, respectively, were flown over the study area at altitudes of 20 and 40 meters and velocities of 3-5 m/s. The Velodyne VLP-Puck LITE has 16 channels that are aligned vertically from -15° to $+15^{\circ}$, resulting in a total vertical field of view (FOV) of 30° . The point capture rate in single return mode is $\sim 300,000$ points per second. The range accuracy is typically ± 3 cm, with a maximum measurement range of 100m (Velodyne VLP-Puck LITE). The Velodyne VLP-32C has 32 channels that are aligned vertically from -15° to $+25^{\circ}$, in a total vertical FOV of 40° . The point capture rate in single return mode is $\sim 600,000$ points per second. The range accuracy is typically ± 3 cm, with a maximum measurement range of 200m (Velodyne VLP-32C, n.d.). Both UAVs were equipped with an integrated global navigation satellite system/inertial navigation system (GNSS/INS) Trimble APX-15v3 for direct georeferencing. The LiDAR data over the HIPS maize experiment were collected weekly using the two platforms from June 12th, 2020 (thirty-one days after sowing (DAS)) to July 13th, 2020 (sixty-two DAS). The LiDAR data over the SbDivTc_Cal sorghum experiment were collected from June 26th, 2020 (forty-four DAS) to July 28th, 2020 (seventy-six DAS). Data collection in both experiments was completed around the flowering date, as the plant growth essentially terminates at that time. Table 4.2 details the specifications of the platforms and mounted sensors.

Table 4.2. Platforms and mounted sensors specification

Platform	Sensor	Unit	Description
UAV-1			
	RGB camera	1	36.4 MP Sony Alpha 7R (ILCE-7R)
	LiDAR sensor	1	Velodyne VLP 16-Puck Lite-range accuracy of ± 3 cm
	GNSS/INS	1	Trimble APX-15 v2
	hyperspectral camera	1	Headwall Nano Hyperspect (VINIR)
UAV-2			
	RGB camera	1	36.4 MP Sony Alpha 7R (ILCE-7R)
	LiDAR sensor	1	Velodyne VLP 32-range accuracy of ± 3 cm
	GNSS/INS	1	Trimble APX-15 v2

The point density and canopy penetration varied with the sensor types and the mission protocols. Tables 4.3 and 4.4 summarize the point density of the LiDAR over both fields for comparison of the impact of the sensor and flying height. Figure 4.3 shows sample data acquired by the VLP32C at 20m height over sorghum and maize.

Table 4.3. Ground point density of sorghum over SbDivTc_Cal

Date	Platform	Platform Height	DAS	Point Density (Points/m ²)
7/20/2020	UAV-1	40 m	68	70
7/20/2020	UAV-2	20 m	68	500

Table 4.4. Ground point density of maize over HIPS

Date	Platform	Flying Height	DAS	Point Density (Points/m ²)
7/11/2020	UAV-1	40 m	60	65
7/11/2020	UAV-1	20 m	60	244
7/11/2020	UAV-2	40 m	60	122
7/11/2020	UAV-2	20 m	60	617

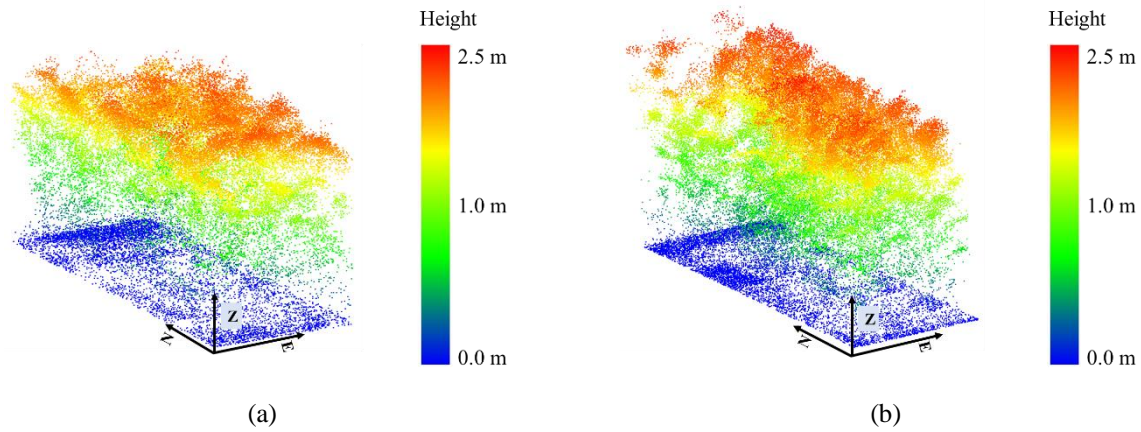


Figure 4.3. Example point clouds acquired from UAV-2 (a) sorghum rows 2 and 3 from SbDivTc_Cal on July 13th, 2020 (61 DAS), and (b) from maize from HIPS on July 11th, 2020 (60 DAS).

4.3.2.2 Ground Reference Data

Reference data were collected weekly over the two field experiments from 6/15/20 to 7/27/20 using a LI-COR handheld plant canopy analyzer (LAI-2200C). The instrument provides an indirect measurement of effective LAI based on canopy gap fraction analysis (Welles and Cohen, 1996; Sonnentag et al., 2007; Černý et al., 2019).

Two sets of five measurements (one measurement above the canopy and four measurements below the canopy near the ground) in the direction of the rows were acquired, then averaged to provide one value per plot, then one value per plot was calculated using the Field Viewer 2200 (FV2200) software. These values were used as the reference data set for developing predictive models of LAI based on remote sensing data.

Table 5 summarizes the LiDAR data collection for two experiments with their corresponding ground reference measurements. Both the UAV and wheel-based platforms carried other sensors, and data were acquired operationally at 40m altitude for multiple purposes. Lower altitude flights were conducted more frequently to monitor flowering in July, providing the opportunity to evaluate the impact of flying height on the penetration of the canopy.

Table 4.5. Days After Sowing (DAS) relative to the available ground reference and LiDAR data in 2020

Experiment	Platform	Flying Height	Sowing Date	LiDAR Data Collection Date	DAS ¹	Ground Reference Date	DAS ²
HIPS	UAV-2	40 m	05/12	06/12	31	06/15	34
	UAV-1	40 m		06/17	36	06/15	34
	UAV-1	40 m		06/25	44	06/22	41
	UAV-1	40 m		07/02	51	06/29	48
	UAV-2	20 m		07/07	56	07/06	55
	UAV-2	20 m		07/11	60	07/13	62
	UAV-1	20 m		07/11	60	07/13	62
	UAV-2	20 m		07/13	62	07/13	62
SbDivTc_Cal	UAV-1	40 m	05/13	07/02	50	06/29	47
	UAV-2	20 m		07/07	55	07/06	54
	UAV-2	20 m		07/13	61	07/13	61
	UAV-1	40 m		07/17	65	07/20	68
	UAV-1	40 m		07/20	68	07/20	68
	UAV-2	20 m		07/20	68	07/20	68
	UAV-1	40 m		07/28	76	07/27	75
	UAV-2	20 m		07/28	76	07/27	75

DAS¹: DAS with respect to data collection data; DAS²: DAS with respect to ground reference data

4.4 Methodology

4.4.1 AutoEncoder Feature Extraction from LiDAR Data

4.4.1.1 SbDivTc_Cal (Sorghum)

The SbDivTc_Cal field was planted in ten-row plots. Features were extracted from rows 2 and 3, as the other rows were either adjacent to rows that were destructively sampled or were border rows, where the associated plants did not have consistent conditions in terms of accessibility to solar radiation. The PointNet AutoEncoder was used to reconstruct the input point cloud from the rows and extract the global features. All inputs to the network should have the same number of samples per plot. As the number of LiDAR points in each dataset and each plot was different, the number of common points in the plots dictated the maximum number of inputs (for UAV-1 datasets: 9000 points and UAV-2: 29,000 points). For plots where the number of points exceeded the minimum, the points were selected randomly. Three other subsets of all datasets (2000, 5000, and 7000 points) were also selected randomly and analyzed to evaluate the required time for training and the loss value. Figure 4.4 shows the loss of training in 1000 epochs for three subsets.

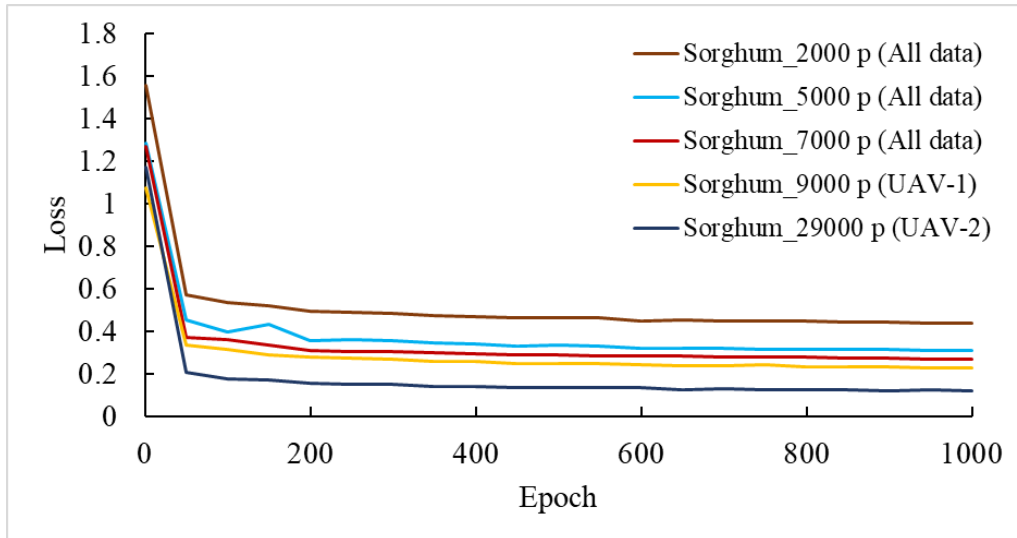


Figure 4.4. Evaluation of the loss between sorghum datasets with 2000, 5000, 7000 points.

Table 4.6 details the associated training time. All experiments were carried out on a cluster node equipped with an Intel 16-core CPU with 192 GB memory and one NVIDIA GeForce P100 GPU.

Table 4.6. Sorghum training time			
No	Data	Number of Points	Training Time (HH:MM)
1	UAV-1 and UAV-2	2000	00:36
2	UAV-1 and UAV-2	5000	01:30
3	UAV-1 and UAV-2	7000	02:04
4	UAV-1	9000	00:58
5	UAV-2	29000	03:43

The 29,000-point subset of UAV-2 datasets had the lowest loss and highest training time, although it was quite reasonable. Figure 4.5 shows a sample of the minimum (2000), 7000, and maximum (29,000) points with their respective reconstructed point clouds.

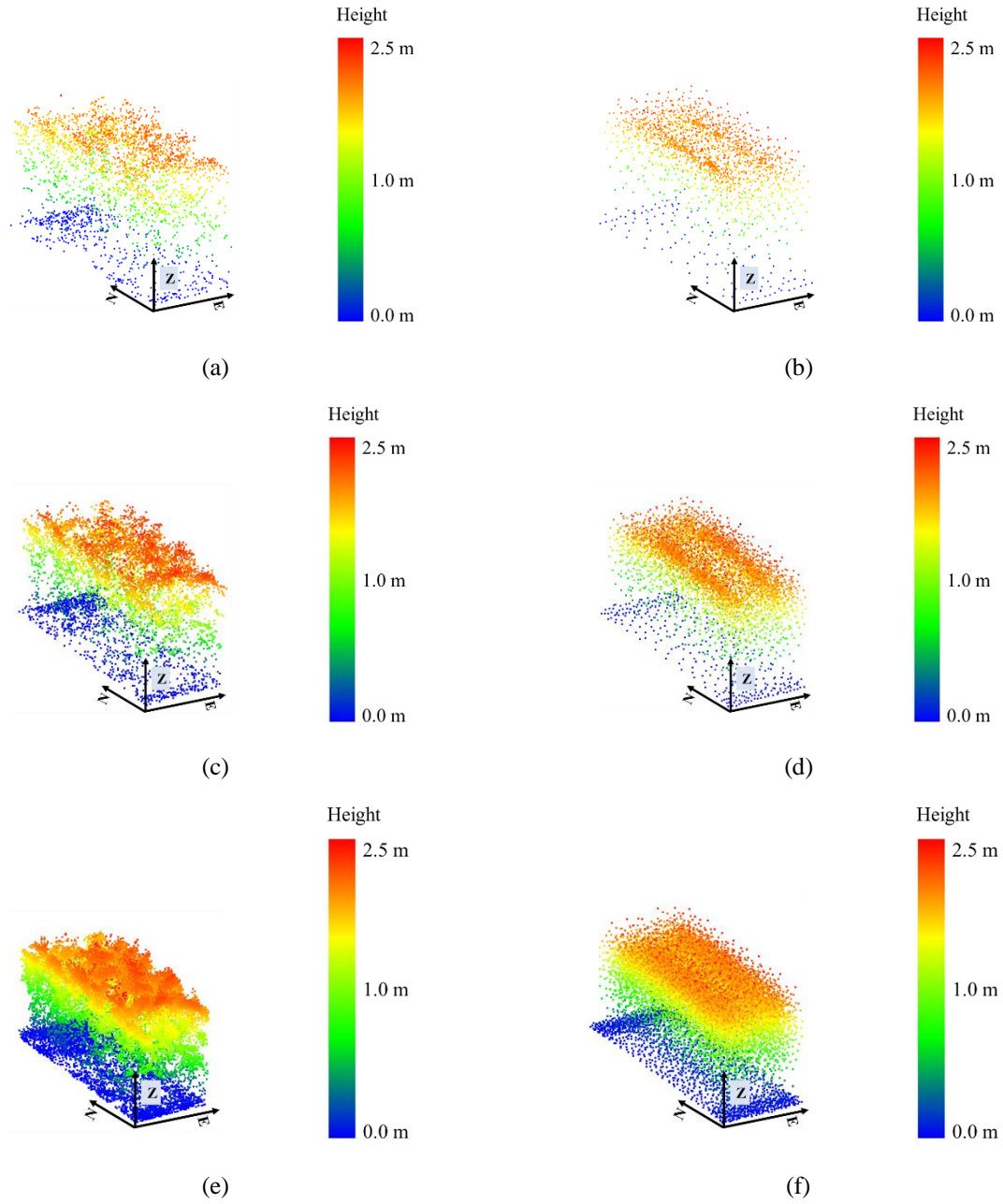


Figure 4.5. Example of input with 2000 (a), 7000 (c), and 29000 (e) points; Figures (b), (d), and (f) show the corresponding reconstructed point clouds acquired from UAV-2 over sorghum rows 2/3 from SbDivTc_Cal on July 13th, 2020 (DAS:61).

Also, Figure 4.6 shows an input with 9000 points and the reconstructed point clouds for early and late-season acquisitions.

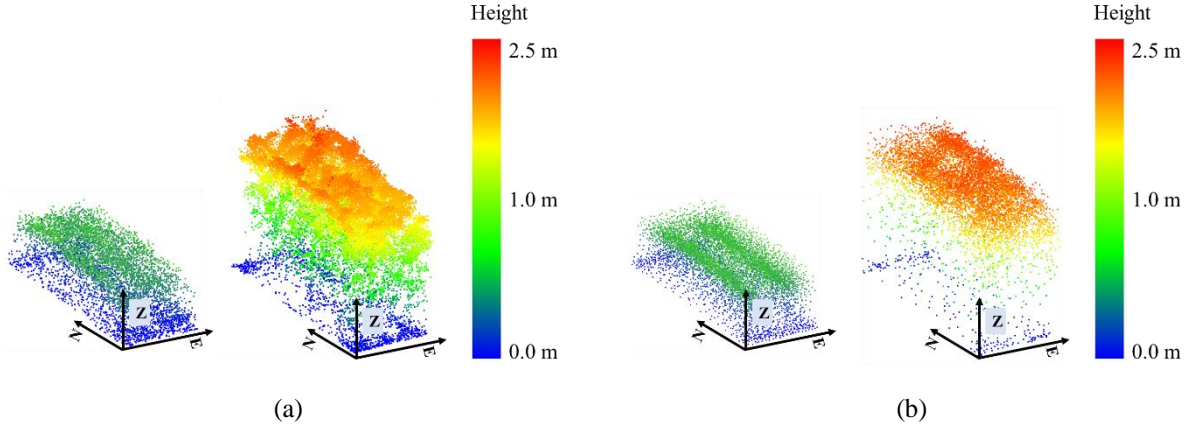
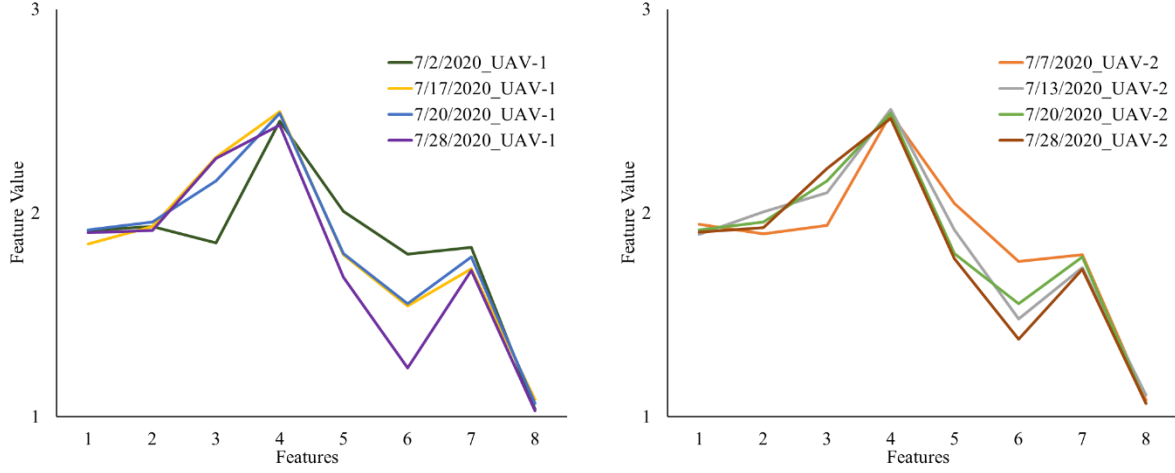


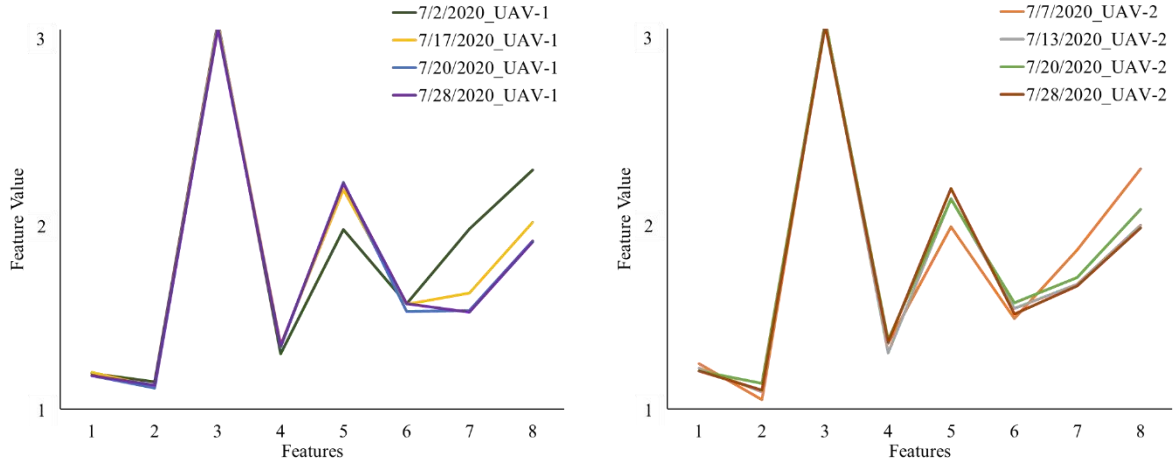
Figure 4.6. Example of (a) input with 9000 points on 7/02/2020 (DAS:50) and 7/28/2020 (DAS:76), and (b) the corresponding reconstructed point clouds acquired from UAV-1 over sorghum rows 2 and 3 from SbDivTc_Cal.

The data were divided into 80% training, 20% testing with 10-fold cross-validation on the training data. The model was trained for 1000 epochs (500, 1000, 2000 epochs were examined) and a learning rate of 0.001, which were determined from a grid search (0.00001 to 0.01 with a step of 10). After obtaining the model, the global features were extracted for each input (8 and 16 features were examined). The models based on eight features yielded better results in terms of R^2 (~ 0.5). A set of features was obtained for each plot for each of 2000, 7000, 9000, and 29,000 point inputs. Figure 4.7 shows an example of extracted features for one variety of the SbDivTc_Cal experiment with the corresponding numbers of input points. Encoder-based features for the 2000 and 7000 input data were remarkably similar across the season, indicating that the distribution of the points throughout the canopy was similar. This was still somewhat surprising, as the canopy changed throughout the growing season. For 2000 points, features 1, 2, 4, 7, and 8 were quite similar, but features 3, 5, 6 were different. Feature 3 increased throughout the season and feature 6 decreased for data from both UAV 1 and UAV2, so these patterns are likely due to the evolution of the canopy. For 7000 points, all the features were similar throughout the season except 5, 7, and 8, with feature 5 decreasing throughout the season and features 7 and 8 increasing for both UAVs. Because the number of points was the same due to sampling (across platforms and heights), the

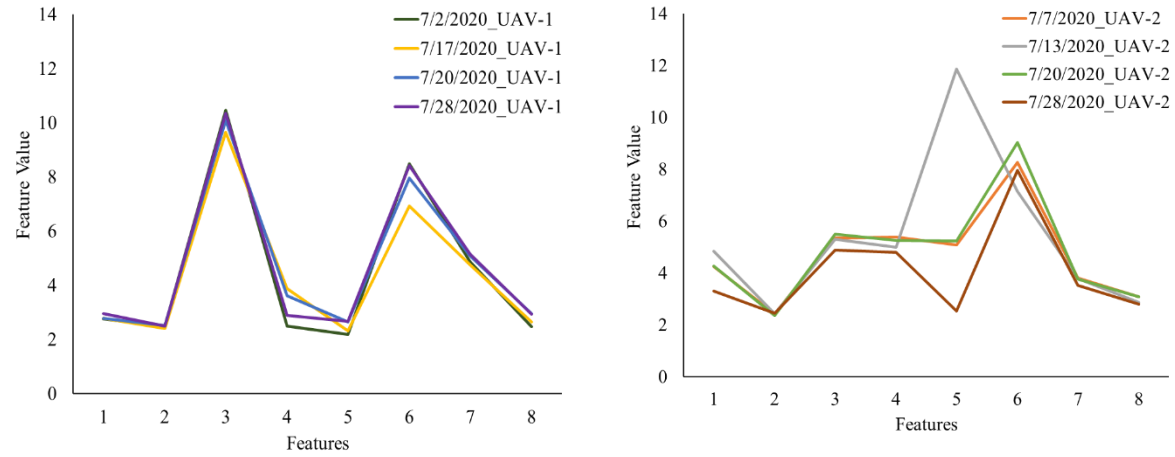
similarity of the features for the two platforms was not surprising. For the 9000 point input from UAV-1, the features were different from the features based on 2000 and 7000 points, but were similar throughout the growing season. Similar to the 2000 and 7000 point results, these changes in features track the canopy growth. For the 29,000 point input from UAV-2, the early season features were similar but changed later in the season, presumably because the structure of the taller canopy was better represented by these data. Also, the features from UAV-1 (9000 points) and UAV-2 (29000 points) had different patterns, reinforcing the hypothesis that the features were impacted by the number of input points above some minimum threshold. Feature 5 for both 7/13 and 7/28 was dissimilar from its pattern during the rest of the season, with a sharp increase in 7/13 and a sharp decrease in 7/28. The impact of the features across platforms and dates is investigated further in the prediction of R^2 in Section 4.4.3. The overall similarity of features across the growing season is potentially indicative of the robustness of the features and their possible value for transfer learning and should be further investigated.



(a) 2000-point input for UAV-1 and UAV-2



(b) 7000-point input for UAV-1 and UAV-2



(c) 9000-point input for UAV-1; 29000-point input for UAV-2

Figure 4.7. Example of extracted features for one sorghum variety of the SbDivTc_Cal experiment (a) input with 2000 points for UAV-1 and UAV-2, (b) 7000 points for UAV-1 and UAV-2, and (c) 9000 points for UAV-1; 29,000 points for UAV-2.

4.4.1.2 HIPS (Maize)

The HIPS experiment contained 88 plots with two rows in each plot. Similar to sorghum, three subsets were randomly selected with 2000, 6000, and 9000 (min number of points per plot) points from original datasets to train and compute the loss. Figure 4.8 shows the graph of the loss of three training sets (UAV-1 and UAV-2). Table 4.7 shows the training time for three maize subsets.

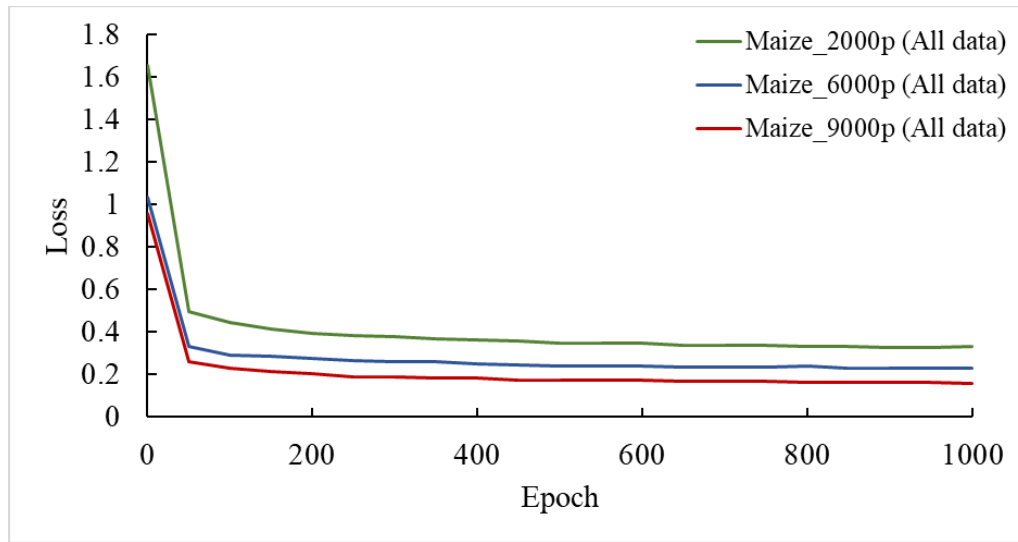


Figure 4.8. Comparing the loss between maize datasets with 2000, 6000, 9000 points

Table 4.7. Maize training time

No	Number of Points	Training Time (HH:MM)
1	2000	00:25
2	6000	00:56
3	9000	01:27

The loss decreased when the number of points increased; however, the time of training increased only slightly. Figure 4.9 shows a sample of the inputs with 2000 and 9000 points and reconstructed point clouds by the PointNet AutoEncoder. The PointNet AutoEncoder was trained with the same approach described in the previous section, and global features were extracted. Similarly, the extracted features and plant canopy analyzer data were used for regression modeling to estimate the maize LAI for both the 2000 and 9000 point subsets.

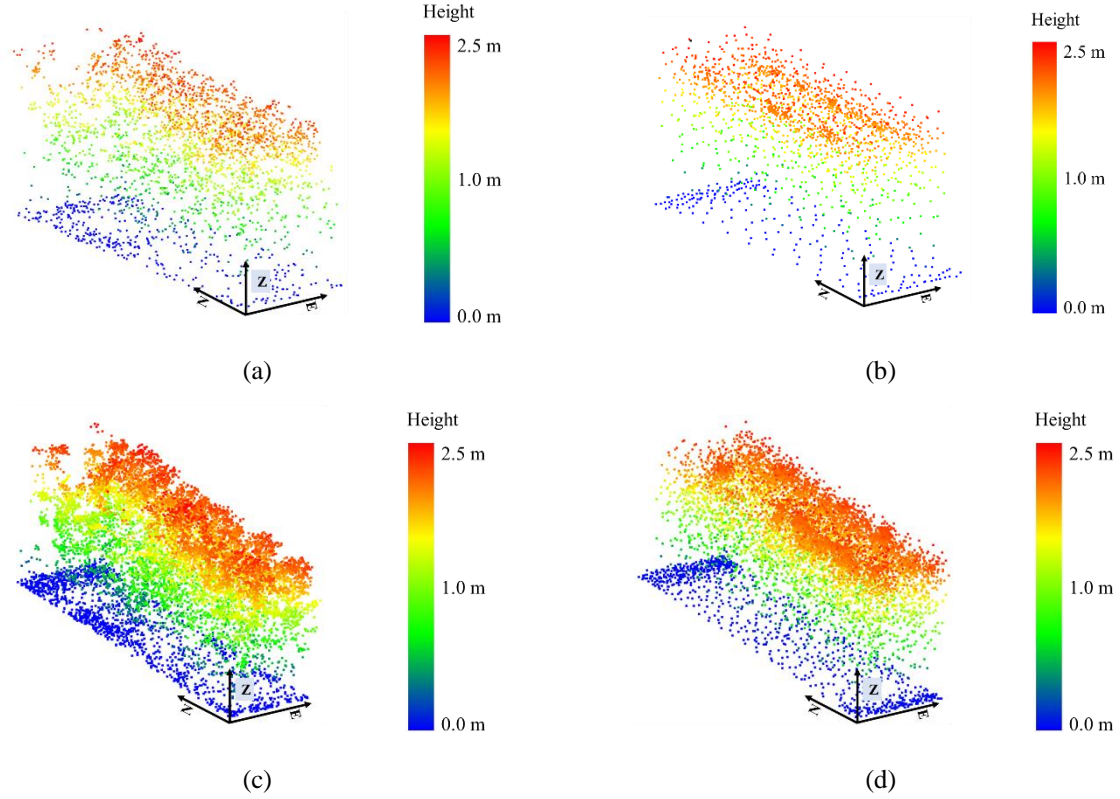
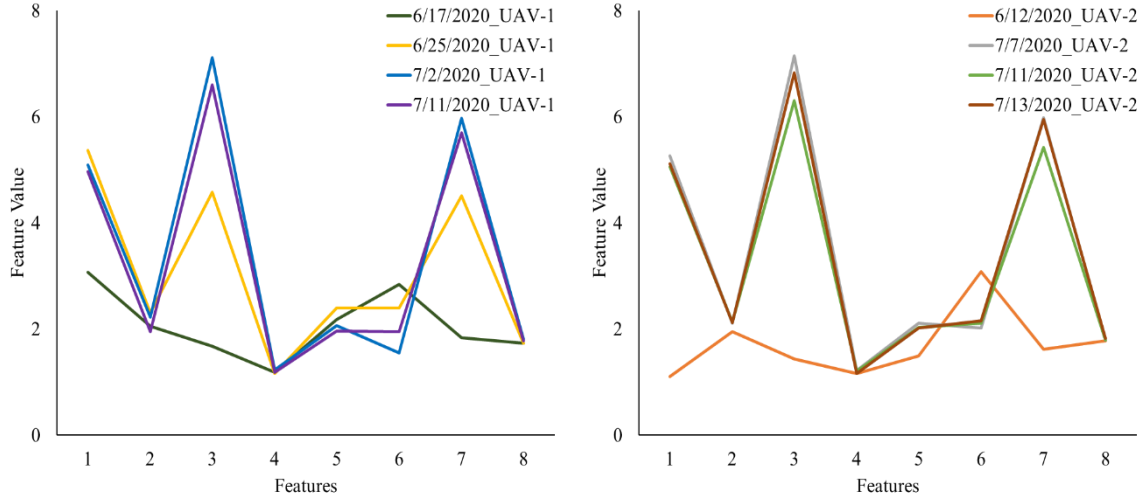
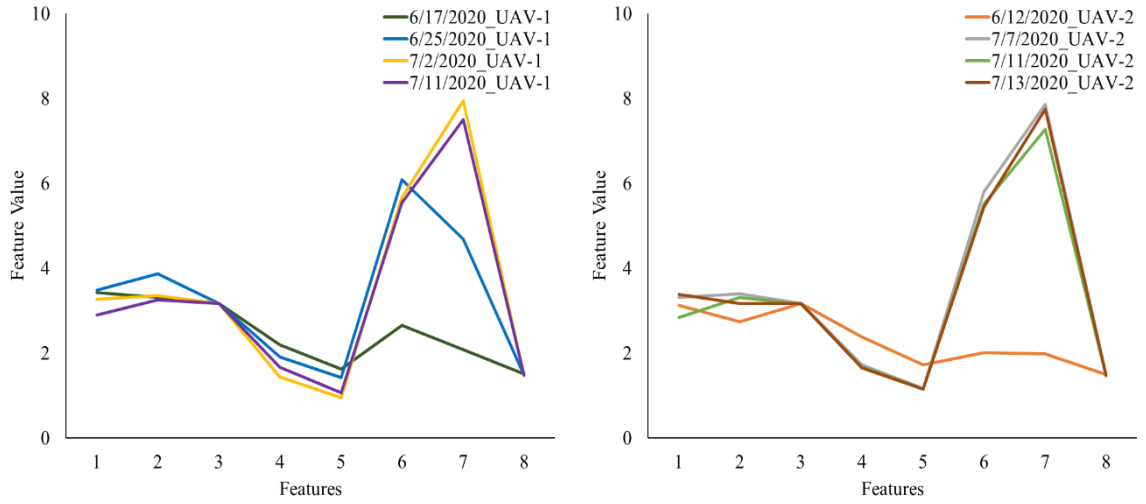


Figure 4.9. Example of input with 2000 (a) and 9000 (c) points, (b) and (d) are the corresponding reconstructed points clouds acquired from UAV-2 over maize from HIPS on 7/11/2020 (DAS:60).

Figure 4.10 shows an example of extracted features for one inbred variety over HIPS with 2000 and 9000 input points for UAV-1 and UAV-2 over all dates. For maize, the features were less similar for the various missions than for sorghum. For 2000 and 9000 points inputs, early-season features were different from later season features derived from both UAV-1 and UAV-2 data, which are potentially related to structural changes in the canopy. Features had a similar pattern for both numbers of input points on UAV-1 and UAV-2. The general patterns of the features are similar to features obtained for sorghum at low density (2000 pts) but are significantly different from sorghum at the end of the season. This could potentially be attributed to the dense canopy of sorghum, including tillers. Relative to the implementation of the encoders in conjunction with deep learning architectures for generalization, blind use of features for transfer learning across the two crops does not appear to be appropriate. Further investigation with additional acquisitions is needed to develop a better understanding of the phenomena.



(a) 2000-point input for UAV-1 and UAV-2



(b) 9000-point input for UAV-1 and UAV-2

Figure 4.10. Example of extracted features for one maize variety of the HIPS experiment (a) input with 2000 points and (b) 9000 points for all datasets. The feature value does not have a unit.

4.4.2 Geometric Feature Extraction from LiDAR Data

The geometric features were extracted from rows 2 and 3 of each plot in the SbDivTc_Cal field and both rows of each plot of the HIPS field. The features included the Laser Penetration Index (LPI) (Richardson et al., 2009), Vertical Complexity Index (VCI) (Pope and Treitz, 2013), Height mean, standard deviation, and skewness, 3rd quartile of height (Nie et al., 2016), Row volume, Cluster Area Plane Index (CAPI) (See 2.4.1).

4.4.3 Empirical Regression Models

Empirical models were developed with physically-based and encoder-based features using SVR with an RBF kernel to estimate LAI. The data were randomly sampled to 75% training and 25% test, and ten-fold cross-validation was performed on the training set. Results using both sets of input features were obtained, and models were evaluated based on the R^2 statistic (Eqn. 4.1).

$$R^2 = 1 - \frac{\sum(y - \hat{y})^2}{\sum(y - \bar{y})^2} \quad (\text{Eqn. 4.1})$$

where y and \hat{y} denote the LAI ground reference and estimated LAI, respectively, \bar{y} is the sample mean of ground reference LAI, and the number of samples is denoted by n .

4.5 Results

Bar charts illustrating the mean R^2 and associated standard deviations of the models developed using both geometric and encoded features using the multiple point cloud sampling rates are shown in Figures 4.11 and 4.12 for the experiments based on the date and the LiDAR sensor mounted on each platform and the two feature extraction methods.

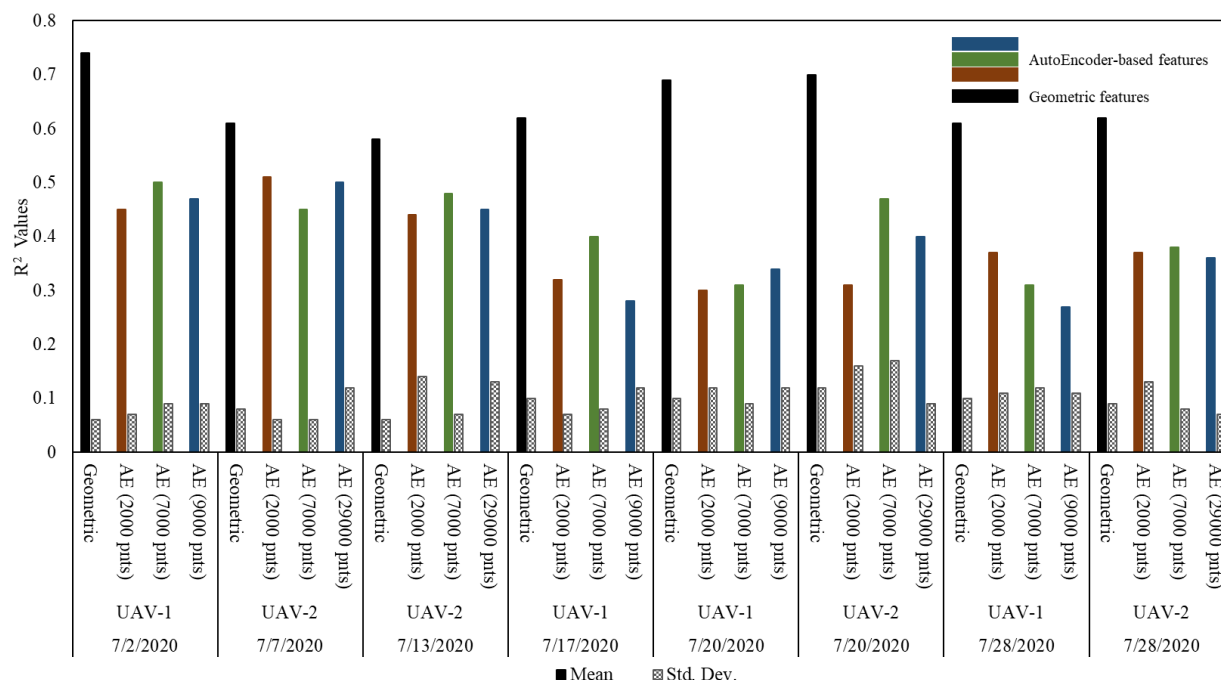


Figure 4.11. R^2 values for sorghum SbDivTc_Cal 2020 SVR regression model for LAI estimation using geometric and autoencoder (AE) feature extraction methods.

Estimates based on geometric features derived from the sorghum data indicate that despite the differences in sensors and flying height, predictions of LAI obtained using data from UAV-1 and UAV-2 were quite similar. The geometric features yielded relatively consistent results in terms of the R^2 statistic (between 0.55 and 0.75) throughout the growing season. The R^2 values of the models using features obtained from the autoencoder were much lower (between 0.30 and 0.55), and particularly later in the season (from 7/17/20). The R^2 values obtained from autoencoder features using the VLP 32C on UAV-2 were higher than for the VLP-16 on UAV-1 on 7/20/2020 and 7/28/2020, dates on which data were acquired by both systems on the same day. Overall, the R^2 results obtained from the autoencoder with the input of 2000, 7000, 9000, and 29000 points did not exhibit consistent patterns and were not as significant as expected. The standard deviation of the R^2 statistic was about 0.05 on earlier dates and increased later in the season to about 0.10 for geometric features. This increased variation of R^2 is consistent with the later season growth in the plants and increased complexity of the canopy. As noted previously, the sorghum was planted at high density, so the penetration dramatically decreased as the growing season progressed. Penetration was further reduced by the sorghum tillers that had an increasing effect later in the

season. The autoencoder features did not capture the structure as well as the physical features, indicating that only the general pattern of the distribution of the LiDAR points through the canopy could be discerned.

In order to evaluate the number of input points to the network for feature extraction using autoencoders, t-tests conducted to evaluate the differences in the mean R^2 values associated with the smallest (2000) and largest (29,000) numbers of points groups were conducted at the 5% significance level based on the sample mean points over sorghum. The p -value of 0.99 indicates that the number of the input points did not significantly impact on R^2 results. A t-test was also conducted to compare the autoencoder vs. geometric feature extraction methods for sorghum. The p -value of 4.34E-6 indicates that the differences between the R^2 values for the two types of features were highly significant.

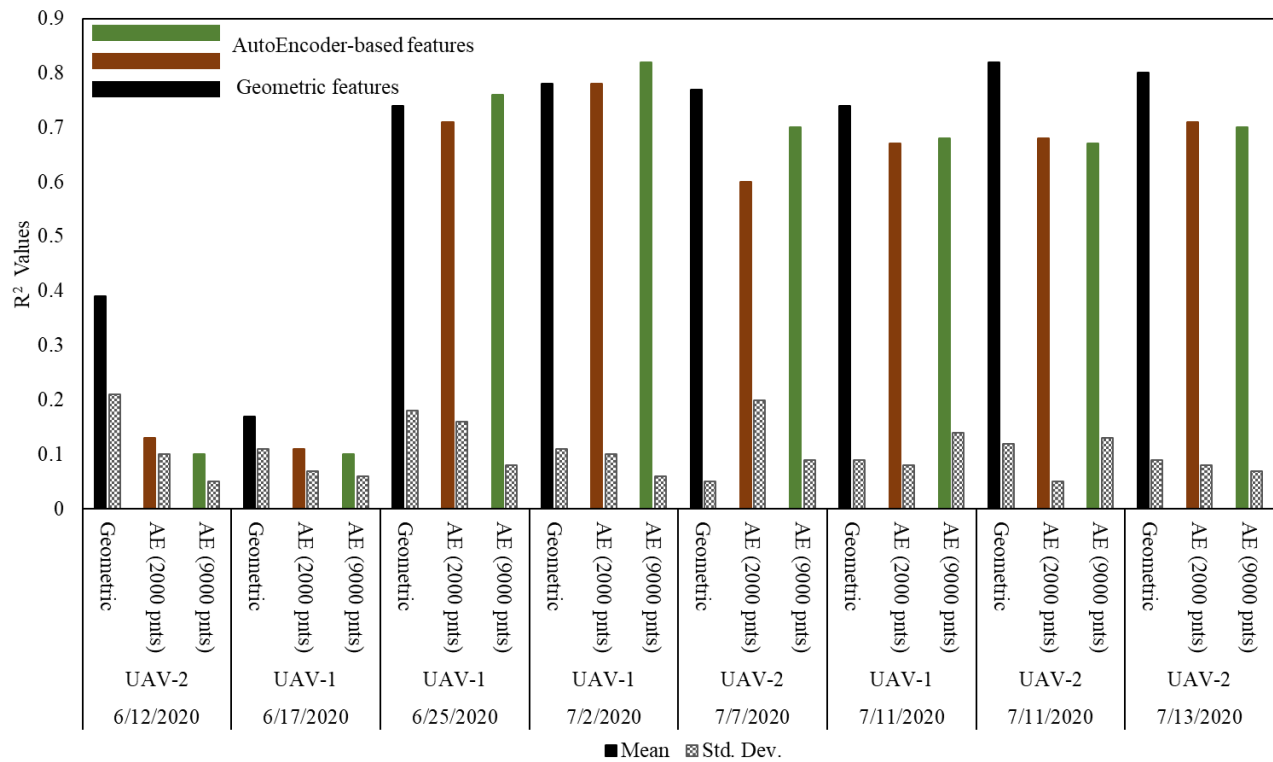


Figure 4.12. R^2 values for HIPS 2020 maize SVR regression model for LAI estimation using geometric and autoencoder (AE) feature extraction methods.

LAI regression-based models were also developed using both geometric and autoencoder features for the HIPS experiment, starting with earlier season acquisitions. The models had low R^2 statistics for the first two dates. The primary reason was that the flying height for both platforms was 40 m, coupled with the small size of the plants (~11 cm and 20 cm) for 6/12/2020 and 6/17/2020, respectively. The measurements from the LAI-2200C acquired between the rows were also not representative of the true canopy gap fraction at this height. The values of the R^2 statistic for 6/25/2020 (41 DAS) to 7/13/2020 (62 DAS) range from 0.74 to 0.85. The lower flying height of both platforms resulted in significantly higher point density (Tables 4.3 and 4.4). The model results obtained using the autoencoder-based features follow the same pattern as the results using geometric features for the datasets from 6/25/2020 to 7/13/2020 for both 2000 and 9000 points. Aside from the first two datasets, the R^2 values for the models developed using the two sampling rates (2000 and 9000 points) were very similar, despite a lower training loss of 9000 points. Both approaches (geometric and AutoEncoder) provide much higher values of the R^2 statistic (between 0.70 and 0.80) than for sorghum.

The same experiments were conducted for the number of input points for deep learning feature extraction (2000 vs. 9000 points) and the autoencoder vs. geometric feature extraction methods for maize. The p -values of 0.90 and 0.53 indicate that neither the null hypothesis regarding the number of points or the type of features (geometric vs. autoencoded) were statistically significant was rejected. This indicates that autoencoder feature extraction could be an alternative to geometric feature extraction.

The sorghum SbDivTc_Cal experiment was more diverse than the maize HIPS experiment in terms of the characteristics of the varieties, leading to more consistent, higher R^2 values on maize over HIPS than sorghum over SbDivTc_Cal for both methods of feature extraction. In SbDivTc_Cal, the complexity and density of sorghum plants in the field were higher than maize plants in the HIPS experiment, as noted previously, also contributed to underestimation of LAI. Overall, the encoded features developed for maize were relevant for estimating LAI than for sorghum.

4.6 Summary and Conclusions

In this study, the goal was to investigate the application of an unsupervised autoencoder strategy for feature extraction, as these approaches do not require prior knowledge and definition

of features. This is the first application of the PointNet Autoencoder to plants, whose complex geometry is difficult to characterize. The method was applied to sorghum and maize experiments collected during the 2020 growing season. Because the data were acquired from two different sensors with mission plans that differed in some acquisitions, the study provided the opportunity to investigate the effects of flying height and the LiDAR sensor technology for estimating LAI. Models based on geometric features yielded good R^2 values for both the sorghum and maize fields after the early season ($DAS \geq 40$). Models for maize had higher R^2 values both due to the more open plant structure and lower planting density for a given time in the growing season. The models using features derived by the autoencoder had statistically lower R^2 values than models determined using geometric features for sorghum (R^2 values of geometric features from 0.58 to 0.74 vs. autoencoder features from 0.27 to 0.50) but were similar for maize (R^2 values of geometric features from 0.74 to 0.82 vs. autoencoder features from 0.67 to 0.82). For autoencoder features, the number of points in each dataset did not have a significant impact on the R^2 values based on the t-test statistic p -value (sorghum: 0.99, maize: 0.90). The results indicate that autoencoder feature extraction could be considered as a viable approach, compared to geometric feature extraction for canopies that have lower complexity (e.g., null hypothesis regarding the mean R^2 values of geometric and autoencoder features are equal was not rejected based on t-test statistic p -value of 0.53). However, more investigation is required to evaluate the robustness of the autoencoder feature extraction relative to LiDAR features. For example, investigating transfer learning approaches with multi-year data acquisitions or in another location data to increase the robustness of prediction models either over one type of row crop plant or from one type to another.

5. CONCLUSIONS

5.1 Summary

The research reported in this dissertation investigated the capability of discrete return LiDAR data acquired in the field in 2019 and 2020 at plot scale for predicting LAI in sorghum and maize using multiple LiDAR sensors on airborne and wheel-based platforms. Geometric features were extracted from row-level data within plots, and multiple regression, partial least squares regression (PLSR), and support vector regression (SVR) models were evaluated for their respective predictive capability. As the LiDAR data were contaminated by noise and outliers relative to the plant structure, the impact of removing outliers on the LAI estimation was investigated over sorghum and maize in 2020 data. Appropriate features are required for robust, reliable predictive model. In addition to geometric features, an unsupervised feature extraction approach was investigated for encoding LiDAR point cloud data to estimate LAI over the sorghum and maize, and the results were compared to the estimates obtained using geometric features.

5.2 Contributions of this work

Contributions of this work are briefly described in the following.

- Investigation of multiple LiDAR-based features for multitemporal prediction of LAI via regression models and evaluation of the capability of LiDAR sensors and platforms for acquiring data to predict LAI in sorghum and maize at multiple times during the growing season.
- Investigation of outlier removal methods including geometric and deep learning-based PointCleanNet to improve the LAI prediction models. For the geometric method, the algorithm from Wang and Feng (2015) was modified for plant data. The PointCleanNet was trained based on synthetic data and applied for field data with complex geometry.
- Investigation of an autoencoder deep learning feature extraction strategy (PointNet AutoEncoder) as an alternative to physical feature extraction to estimate LAI. This is the first application of the PointNet AutoEncoder to plants, whose complex geometry is difficult to characterize.

5.3 Objectives and Key Findings

The objectives and key findings in each chapter of this dissertation are summarized in the following.

- Chapter 2: The objective of this chapter was to investigate the capability of LiDAR data to estimate effective LAI over sorghum experiment fields in 2019 and 2020. Three LiDAR datasets collected in 2019 from a UAV platform were post-processed and used to develop LAI predictive models based on available destructive sampling ground reference data. Due to low point density, canopy penetration, and use of true LAI as a ground reference, the LAI models had low R^2 values. In 2020, UAVs and PhenoRover LiDAR datasets were collected and analyzed using a plant canopy analyzer, as well as limited destructive sampling for ground reference. LiDAR data acquired from the UAV-2 with a Velodyne VLP-32C were higher density, and there was greater penetration through the canopy than with a Velodyne VLP-Puck Lite, and particularly at lower flight altitudes. However, in most cases, the R^2 values for estimated LAI obtained using the two UAVs, as well as the PhenoRover, were similar. The models were developed using diverse hybrids in the calibration panels, including some photoperiod sensitive varieties. The R^2 values of the models improved when the photoperiod sensitive varieties were excluded, and especially in the later season. The geometric features used in this study were based on height-related sample statistics, canopy gap fraction feature (LPI) as well as the proposed horizontal feature (CAPI). In most of the datasets, the UAV models had higher R^2 values compared to those developed using wheel-based data in 2020, especially later in the growing season. The nonlinear regression model SVR with an RBF kernel had the highest R^2 and lowest RMSE of all other methods used in this study. The study encountered multiple challenges, including that the method for acquiring ground reference data changed during the two-year period. The more intensive remote sensing data acquisition campaign in 2020 and the use of the plant canopy analyzer LAI-2200C for ground reference data were motivated by the need for more frequent data acquisitions during the vegetative stages of the growth cycle when the plants were growing rapidly.
- Chapter 3: This chapter investigated two outlier removal methods for point clouds from the greenhouse, synthetic data, and field sorghum and maize plants. The goal was to evaluate the impact of outlier removal on LAI estimation over field data (sorghum and maize). The

outlier removal method from Wang and Feng (2015) was initially implemented and evaluated for non-isolated outliers in the point cloud. For removing isolated outliers, a simple approach based on the geometric relationship between points was proposed. This method requires specification of input parameters, including radius search and number of points in a neighborhood of a point of interest. These parameters were sensitive to the distribution and density of the points in the dataset. When a platform is stationary, and the points are uniformly distributed, e.g., as in the example of the individual plant in this study, finding the parameters is straightforward, as the density of points is adequate to detect the outliers. When the platform moves, the points are distributed sparsely. Coupled with the irregular shape of the plant-based objects, it is challenging for this method to remove the outliers. When the method was applied to sorghum datasets acquired from a UAV and the PhenoRover wheeled vehicle, the points within the canopy were sparse, and the geometric method did not perform well. In the maize dataset, the structure of the plants was visually more identifiable from both the UAV and the PhenoRover. Although some outliers were removed from the sorghum dataset, the plant structure was not recognizable after outlier removal. This illustrates the impact of sparse point datasets on this outlier removal approach. The PointCleanNet deep learning framework was also investigated for removing outliers from a LiDAR point cloud obtained for a single plant in a greenhouse, and multiple plant image-based point clouds derived image and field data. When the model was retrained using generated point clouds from overlapped images that were contaminated with different levels of simulated outliers, the loss was lower than the training the model-based solely on point clouds from actual plants. The network successfully removed different levels of outliers in the greenhouse data, which were not as complex as field data in terms of geometry and level of outliers. PointCleanNet was also applied to both maize and sorghum field data whose outliers included the impact of the complex structure of multiple rows of densely sown plants and movement of the platforms. LAI was estimated over field plots before and after outlier removal using the sorghum and maize data from both platforms. Although the p values from t-test statistics (sorghum:0.79, maize:0.78) show that there was not a significant difference between results obtained using data prior to and after outlier removal, the R^2 values of estimated LAI from the PhenoRover improved both in terms of increased sample means and decreased standard deviations of R^2 (e.g., sorghum on 7/24/2020 before outlier removed 0.57

and after 0.66). Based on these experiments, removal of outliers appears to be justified for plant structures when the point density is greater than ~ 600 points per m^2 , as was the case for the low altitude UAV and PhenoRover acquisitions where penetration through the canopy was higher.

- Chapter 4: In this chapter, the primary focus was to investigate the application of an unsupervised autoencoder strategy for feature extraction, as these approaches do not require prior knowledge and definition of physical features. The method was applied to sorghum (SbDivTc_Cal) and maize (HIPS) experiments collected during the 2020 growing season. Because the data were acquired by two sensors (VLP-32C and VLP Puck Lite) on different platforms, the study provided the opportunity to investigate the effects of flying height and the different LiDAR sensors on the feature encoding and the resulting models. Models based on geometric features yielded good R^2 values for both the sorghum and maize fields. Models for maize had higher R^2 values due to both the plant structure and lower planting density (maize R^2 values from 0.74 to 0.82 vs. sorghum R^2 values from 0.58 to 0.74). The models using features derived by the autoencoder have substantially lower, statistically different R^2 values than models determined using geometric features for sorghum (R^2 values of geometric features from 0.58 to 0.74 vs. autoencoder features from 0.27 to 0.50) but are similar for maize (R^2 values of geometric features from 0.74 to 0.82 vs. autoencoder features from 0.67 to 0.82). The results indicate that autoencoder feature extraction could be considered as an alternative to geometric feature extraction for canopies that are less dense. (e.g., maize null hypothesis was not rejected based on t-test statistic p -value of 0.53). However, geometric features are recommended as the model values are superior, and they can be related to the plant characteristics.

5.4 Research Limitations and Challenges

Some limitation and challenges throughout this research are listed as follows:

- LAI Ground reference: In this study, destructive sampling and LAI-2200C plant canopy analyzer were used as a ground reference. In 2019 three destructive sampling data sets were acquired. The 2020 season included investigation of LAI-2200C data as a reference source for LAI. There were three destructive sampling data sets, and weekly LAI-2200C data were collected throughout the season, but there was only one common date for the two approaches,

as destructive sampling is performed at the beginning of the season, around flowering time, and at the end of the season. It is necessary to have more coincided of two types of reference to formulate the relationship between them, although increasing the destructive sampling would require larger plots with more rows.

- **Limitation in field sample data:** For outlier removal by the deep learning method, having training data similar to the field data would increase the robustness of the models. In this study, the training data was synthetically generated from imagery whose characteristics were not aligned completely with the field data in terms of environmental condition and method of planting (e.g., planting in pots). Acquisition of LiDAR data from a gantry or a controlled facility with field arrangement simulation should be considered for future studies.
- **Noisy Data:** After outlier removal, the field-based PhenoRover and UAV LiDAR data are contaminated by noise from different sources, including the moving platform, multi-path, and the complex geometry of plant structure. Although the PhenoRover platform LiDAR units are quite close to the plants, the plant structure and geometric characteristics could not be extracted directly from these data.

5.5 Future Work and Recommendations

Based on the results of this study, several future research directions should be considered:

- **Flight configuration:** The trajectories of all the data acquired in 2019 and 2020 were in the row direction. As the platform did not fly over each row, there were more occluded areas between rows as the distance increased from the nadir, resulting in lower penetration deeper of the canopy. It is recommended to investigate flying perpendicular to the rows to determine whether canopy penetration is increased.
- **Additional data sources in LAI prediction models:** Other sources of data such as RGB imagery should be investigated. Extracting features from RGB imagery, including leaf count and canopy cover, may enhance the performance of a predictive model. Also, the data from platforms such as small-wheeled rovers that provide data beneath the canopy would be useful to observe the structure of the plants deeper in the canopy and potentially provide additional features.
- **Implementation of multi-temporal deep learning networks for prediction,** instead of classical SVR methods.

- Transfer learning: Investigate transfer learning approaches with multi-year data acquisitions to increase the robustness of prediction models. Also, some environmental and weather condition features could be useful if there is more than one year of data.
- Explore relationships between approaches for ground reference: Further study is needed to investigate the impact of the different methods in providing ground reference data, both in terms of quality control and their impact on prediction models.
- Field-based LiDAR reference data: Training data is the basis for and one of the major challenges in machine learning, and particularly for deep learning. Although synthetic data could be used in training, they do not generally have the rich geometric characteristics of field data. Having reliable field data that are collected under controlled environmental conditions with a stationary platform, such as a gantry, would be beneficial to incorporate in the machine learning and deep learning models as well as use as a reference for evaluating new methods.

REFERENCES

- Agresti, G., Minto, L., Marin, G., & Zanuttigh, P. (2017). Deep learning for confidence information in stereo and tof data fusion. *Proceedings of the IEEE International Conference on Computer Vision*, 697–705.
- Akinseye, F. M., Adam, M., Agele, S. O., Hoffmann, M. P., Traore, P. C. S., & Whitbread, A. M. (2017). Assessing crop model improvements through comparison of sorghum (sorghum bicolor L. moench) simulation models: A case study of West African varieties. *Field Crops Research*, 201, 19–31. <https://doi.org/10.1016/j.fcr.2016.10.015>
- Alonzo, M., Bookhagen, B., McFadden, J. P., Sun, A., & Roberts, D. A. (2015). Mapping urban forest leaf area index with airborne lidar using penetration metrics and allometry. *Remote Sensing of Environment*, 162, 141–153.
- Aoki, Y., Goforth, H., Srivatsan, R. A., & Lucey, S. (2019). Pointnetlk: Robust & efficient point cloud registration using pointnet. *Proceedings of the IEEE Conference on Computer Vision and Pattern Recognition*, 7163–7172.
- Apolo-Apolo, O. E., Pérez-Ruiz, M., Martínez-Guanter, J., & Egea, G. (2020). A mixed data-based deep neural network to estimate leaf area index in wheat breeding trials. *Agronomy*, 10(2), 175.
- Ariza-Carricondo, C., Di Mauro, F., de Beeck, M. O., Roland, M., Gielen, B., Vitale, D., Ceulemans, R., & Papale, D. (2019). A comparison of different methods for assessing leaf area index in four canopy types. *Central European Forestry Journal*, 65(2), 67–80.
- Bengio, Y. (2012). Deep learning of representations for unsupervised and transfer learning. *Proceedings of ICML Workshop on Unsupervised and Transfer Learning*, 17–36.
- Blancon, J., Dutartre, D., Tixier, M.-H., Weiss, M., Comar, A., Praud, S., & Baret, F. (2019). A High-Throughput Model-Assisted Method for Phenotyping Maize Green Leaf Area Index Dynamics Using Unmanned Aerial Vehicle Imagery. *Frontiers in Plant Science*, 10. <https://doi.org/10.3389/fpls.2019.00685>
- Boulch, A., & Marlet, R. (2016). Deep Learning for Robust Normal Estimation in Unstructured Point Clouds. *Computer Graphics Forum*, 35(5), 281–290. <https://doi.org/10.1111/cgf.12983>
- Bréda, N. J. J. (2003). Ground-based measurements of leaf area index: A review of methods, instruments and current controversies. *Journal of Experimental Botany*, 54(392), 2403–2417. <https://doi.org/10.1093/jxb/erg263>

- Brenner, A. J., Cueto Romero, M., Garcia Haro, J., Gilabert, M. A., Incoll, L. D., Martinez Fernandez, J., Porter, E., Pugnaire, F. I., & Younis, M. T. (1995). *A comparison of direct and indirect methods for measuring leaf and surface areas of individual bushes*. Wiley Online Library.
- Černý, J., Pokorný, R., Haninec, P., & Bednář, P. (2019). Leaf Area Index Estimation Using Three Distinct Methods in Pure Deciduous Stands. *Journal of Visualized Experiments: JoVE*, 150.
- Chang, Q. (2020). *Mapping shrub biomass, Leaf Area Index and rainfall interception capacities in the Arctic tundra using L-band SAR* [PhD Thesis].
- Chen, J. M., & Black, T. A. (1991). Measuring leaf area index of plant canopies with branch architecture. *Agricultural and Forest Meteorology*, 57(1–3), 1–12.
- Chen, J. M., Menges, C. H., & Leblanc, S. G. (2005). Global mapping of foliage clumping index using multi-angular satellite data. *Remote Sensing of Environment*, 97(4), 447–457.
- Chen, Jing M., & Black, T. A. (1992). Defining leaf area index for non-flat leaves. *Plant, Cell & Environment*, 15(4), 421–429.
- Chen, Jing M., & Cihlar, J. (1996). Retrieving leaf area index of boreal conifer forests using Landsat TM images. *Remote Sensing of Environment*, 55(2), 153–162.
- Chen, Jing M., Rich, P. M., Gower, S. T., Norman, J. M., & Plummer, S. (1997). Leaf area index of boreal forests: Theory, techniques, and measurements. *Journal of Geophysical Research: Atmospheres*, 102(D24), 29429–29443.
- Cheng, G., Yang, C., Yao, X., Guo, L., & Han, J. (2018). When Deep Learning Meets Metric Learning: Remote Sensing Image Scene Classification via Learning Discriminative CNNs. *IEEE Transactions on Geoscience and Remote Sensing*, 56(5), 2811–2821. <https://doi.org/10.1109/TGRS.2017.2783902>
- Cheng, X., Zhong, Y., Dai, Y., Ji, P., & Li, H. (2019). Noise-aware unsupervised deep lidar-stereo fusion. *Proceedings of the IEEE Conference on Computer Vision and Pattern Recognition*, 6339–6348.
- Estrada, J., Sánchez, H., Hernanz, L., Checa, M. J., & Roman, D. (2017). Enabling the Use of Sentinel-2 and LiDAR Data for Common Agriculture Policy Funds Assignment. *ISPRS International Journal of Geo-Information*, 6(8), 255. <https://doi.org/10.3390/ijgi6080255>
- Fang, H., Baret, F., Plummer, S., & Schaepman-Strub, G. (2019). An Overview of Global Leaf Area Index (LAI): Methods, Products, Validation, and Applications. *Reviews of Geophysics*, 57(3), 739–799. <https://doi.org/10.1029/2018RG000608>
- Fang, H., Liu, W., Li, W., & Wei, S. (2018). Estimation of the directional and whole apparent clumping index (ACI) from indirect optical measurements. *ISPRS Journal of Photogrammetry and Remote Sensing*, 144, 1–13.

- FARO Focus3D X 330*. (n.d.). Retrieved September 27, 2020, from <https://faro.app.box.com/s/8ilpeyxcuitnczqgsrgp5rx4a9lb3skq/file/441668110322>
- Fassnacht, K. S., Gower, S. T., Norman, J. M., & McMurtric, R. E. (1994). A comparison of optical and direct methods for estimating foliage surface area index in forests. *Agricultural and Forest Meteorology*, 71(1–2), 183–207.
- Feng, K., & Li, Q. (2014). Using stepwise regression and support vector regression to comprise REITs' portfolio. *2014 IEEE 7th Joint International Information Technology and Artificial Intelligence Conference*, 158–162.
- Fournier, R. A., & Hall, R. J. (2017). *Hemispherical photography in forest science: Theory, methods, applications*. Springer.
- Gaillard, M., Miao, C., Schnable, J. C., & Benes, B. (2020). *Voxel Carving Based 3D Reconstruction of Sorghum Identifies Genetic Determinants of Radiation Interception Efficiency* [Preprint]. *Plant Biology*. <https://doi.org/10.1101/2020.04.06.028605>
- Garcia-Garcia, A., Orts-Escolano, S., Oprea, S., Villena-Martinez, V., & Garcia-Rodriguez, J. (2017). A review on deep learning techniques applied to semantic segmentation. *ArXiv Preprint ArXiv:1704.06857*.
- Ge, L., Cai, Y., Weng, J., & Yuan, J. (2018). Hand pointnet: 3d hand pose estimation using point sets. *Proceedings of the IEEE Conference on Computer Vision and Pattern Recognition*, 8417–8426.
- Guerrero, P., Kleiman, Y., Ovsjanikov, M., & Mitra, N. J. (2018a). PCPNet Learning Local Shape Properties from Raw Point Clouds. *Computer Graphics Forum*, 37(2), 75–85. <https://doi.org/10.1111/cgf.13343>
- Guerrero, P., Kleiman, Y., Ovsjanikov, M., & Mitra, N. J. (2018b). PCPNet Learning Local Shape Properties from Raw Point Clouds. *Computer Graphics Forum*, 37(2), 75–85. <https://doi.org/10.1111/cgf.13343>
- Guo, Y., Wang, H., Hu, Q., Liu, H., Liu, L., & Bennamoun, M. (2020). Deep Learning for 3D Point Clouds: A Survey. *IEEE Transactions on Pattern Analysis and Machine Intelligence*, 1–1. <https://doi.org/10.1109/TPAMI.2020.3005434>
- Hammer, G. L., van Oosterom, E., McLean, G., Chapman, S. C., Broad, I., Harland, P., & Muchow, R. C. (2010). Adapting APSIM to model the physiology and genetics of complex adaptive traits in field crops. *Journal of Experimental Botany*, 61(8), 2185–2202.
- Hasheminasab, S. M., Zhou, T., & Habib, A. (2020). GNSS/INS-Assisted Structure from Motion Strategies for UAV-Based Imagery over Mechanized Agricultural Fields. *Remote Sensing*, 12(3), 351. <https://doi.org/10.3390/rs12030351>
- Hinton, G. E., & Salakhutdinov, R. R. (2006). Reducing the dimensionality of data with neural networks. *Science*, 313(5786), 504–507.

- Jaderberg, M., Simonyan, K., Zisserman, A., & kavukcuoglu, koray. (2015). Spatial Transformer Networks. In C. Cortes, N. D. Lawrence, D. D. Lee, M. Sugiyama, & R. Garnett (Eds.), *Advances in Neural Information Processing Systems* 28 (pp. 2017–2025). Curran Associates, Inc. <http://papers.nips.cc/paper/5854-spatial-transformer-networks.pdf>
- Jensen, J. L., Humes, K. S., Vierling, L. A., & Hudak, A. T. (2008a). Discrete return lidar-based prediction of leaf area index in two conifer forests. *Remote Sensing of Environment*, 112(10), 3947–3957.
- Jensen, J. L., Humes, K. S., Vierling, L. A., & Hudak, A. T. (2008b). Discrete return lidar-based prediction of leaf area index in two conifer forests. *Remote Sensing of Environment*, 112(10), 3947–3957.
- Jimenez-Berni, J. A., Deery, D. M., Rozas-Larraondo, P., Condon, A. T. G., Rebetzke, G. J., James, R. A., Bovill, W. D., Furbank, R. T., & Sirault, X. R. (2018). High throughput determination of plant height, ground cover, and above-ground biomass in wheat with LiDAR. *Frontiers in Plant Science*, 9, 237.
- Johnsson, T. (1992). A procedure for stepwise regression analysis. *Statistical Papers*, 33(1), 21–29. <https://doi.org/10.1007/BF02925308>
- Jonckheere, I., Fleck, S., Nackaerts, K., Muys, B., Coppin, P., Weiss, M., & Baret, F. (2004). Review of methods for in situ leaf area index determination: Part I. Theories, sensors and hemispherical photography. *Agricultural and Forest Meteorology*, 121(1–2), 19–35.
- Jung, J., & Crawford, M. M. (2012). Extraction of Features From LIDAR Waveform Data for Characterizing Forest Structure. *IEEE Geoscience and Remote Sensing Letters*, 9(3), 492–496. <https://doi.org/10.1109/LGRS.2011.2172769>
- Kohara, Y., & Nakazawa, M. (2019). Human Tracking of Single Laser Range Finder Using Features Extracted by Deep Learning. *2019 Twelfth International Conference on Mobile Computing and Ubiquitous Network (ICMU)*, 1–5.
- Korhonen, L., Korpela, I., Heiskanen, J., & Maltamo, M. (2011). Airborne discrete-return LIDAR data in the estimation of vertical canopy cover, angular canopy closure and leaf area index. *Remote Sensing of Environment*, 115(4), 1065–1080.
- Kucharik, C. J., Norman, J. M., Murdock, L., & Gower, S. T. (1997). Characterizing canopy nonrandomness with a multiband vegetation imager (MVI). *Journal of Geophysical Research: Atmospheres*, 102(D24), 29455–29473.
- Küßner, R., & Mosandl, R. (2000). Comparison of direct and indirect estimation of leaf area index in mature Norway spruce stands of eastern Germany. *Canadian Journal of Forest Research*, 30(3), 440–447.
- Lang, A. R. G. (1986). Leaf-area and average leaf angle from transmission of direct sunlight. *Australian Journal of Botany*, 34(3), 349–355.

- Lang, A. R. G., & McMurtrie, R. E. (1992). Total leaf areas of single trees of *Eucalyptus grandis* estimated from transmittances of the sun's beam. *Agricultural and Forest Meteorology*, 58(1–2), 79–92.
- Lauzon, F. Q. (2012). An introduction to deep learning. *2012 11th International Conference on Information Science, Signal Processing and Their Applications (ISSPA)*, 1438–1439. <https://doi.org/10.1109/ISSPA.2012.6310529>
- Lefsky, M. A., Cohen, W. B., Parker, G. G., & Harding, D. J. (2002a). Lidar remote sensing for ecosystem studies: Lidar, an emerging remote sensing technology that directly measures the three-dimensional distribution of plant canopies, can accurately estimate vegetation structural attributes and should be of particular interest to forest, landscape, and global ecologists. *BioScience*, 52(1), 19–30.
- Lefsky, M. A., Cohen, W. B., Parker, G. G., & Harding, D. J. (2002b). Lidar remote sensing for ecosystem studies: Lidar, an emerging remote sensing technology that directly measures the three-dimensional distribution of plant canopies, can accurately estimate vegetation structural attributes and should be of particular interest to forest, landscape, and global ecologists. *BioScience*, 52(1), 19–30.
- Li, F., Piasecki, C., Millwood, R. J., Wolfe, B., Mazarei, M., & Stewart, C. N. (2020). High-Throughput Switchgrass Phenotyping and Biomass Modeling by UAV. *Frontiers in Plant Science*, 11. <https://doi.org/10.3389/fpls.2020.574073>
- Lobell, D. B., Thau, D., Seifert, C., Engle, E., & Little, B. (2015). A scalable satellite-based crop yield mapper. *Remote Sensing of Environment*, 164, 324–333.
- Ludwig, J. A., QUARTET, L., & Reynolds, J. F. (1988). *Statistical ecology: A primer in methods and computing* (Vol. 1). John Wiley & Sons.
- Ma, L., Liu, Y., Zhang, X., Ye, Y., Yin, G., & Johnson, B. A. (2019). Deep learning in remote sensing applications: A meta-analysis and review. *ISPRS Journal of Photogrammetry and Remote Sensing*, 152, 166–177.
- Masjedi, A., Carpenter, N. R., Crawford, M. M., & Tuinstra, M. R. (2019). Prediction of Sorghum Biomass Using Uav Time Series Data and Recurrent Neural Networks. *Proceedings of the IEEE Conference on Computer Vision and Pattern Recognition Workshops*, 0–0.
- Masjedi, A., Crawford, M. M., Carpenter, N. R., & Tuinstra, M. R. (2020). Multi-Temporal Predictive Modelling of Sorghum Biomass Using UAV-Based Hyperspectral and LiDAR Data. *Remote Sensing*, 12(21), 3587. <https://doi.org/10.3390/rs12213587>
- Masjedi, A., Zhao, J., Thompson, A. M., Yang, K.-W., Flatt, J. E., Crawford, M. M., Ebert, D. S., Tuinstra, M. R., Hammer, G., & Chapman, S. (2018). Sorghum Biomass Prediction Using Uav-Based Remote Sensing Data and Crop Model Simulation. *IGARSS 2018 - 2018 IEEE International Geoscience and Remote Sensing Symposium*, 7719–7722. <https://doi.org/10.1109/IGARSS.2018.8519034>

- Myneni, R. B., Ramakrishna, R., Nemani, R., & Running, S. W. (1997). Estimation of global leaf area index and absorbed PAR using radiative transfer models. *IEEE Transactions on Geoscience and Remote Sensing*, 35(6), 1380–1393.
- Nie, S., Wang, C., Dong, P., & Xi, X. (2016). Estimating leaf area index of maize using airborne full-waveform lidar data. *Remote Sensing Letters*, 7(2), 111–120.
- Nie, S., Wang, C., Dong, P., Xi, X., Luo, S., & Zhou, H. (2016a). Estimating leaf area index of maize using airborne discrete-return LiDAR data. *IEEE Journal of Selected Topics in Applied Earth Observations and Remote Sensing*, 9(7), 3259–3266.
- Nie, S., Wang, C., Dong, P., Xi, X., Luo, S., & Zhou, H. (2016b). Estimating leaf area index of maize using airborne discrete-return LiDAR data. *IEEE Journal of Selected Topics in Applied Earth Observations and Remote Sensing*, 9(7), 3259–3266.
- Peduzzi, A., Wynne, R. H., Fox, T. R., Nelson, R. F., & Thomas, V. A. (2012). Estimating leaf area index in intensively managed pine plantations using airborne laser scanner data. *Forest Ecology and Management*, 270, 54–65.
- Petrovska, B., Zdravevski, E., Lameski, P., Corizzo, R., Štajduhar, I., & Lerga, J. (2020). Deep learning for feature extraction in remote sensing: A case-study of aerial scene classification. *Sensors*, 20(14), 3906.
- Pope, G., & Treitz, P. (2013a). Leaf area index (LAI) estimation in boreal mixedwood forest of Ontario, Canada using light detection and ranging (LiDAR) and WorldView-2 imagery. *Remote Sensing*, 5(10), 5040–5063.
- Pope, G., & Treitz, P. (2013b). Leaf area index (LAI) estimation in boreal mixedwood forest of Ontario, Canada using light detection and ranging (LiDAR) and WorldView-2 imagery. *Remote Sensing*, 5(10), 5040–5063.
- Poux, F., & Billen, R. (2019). Voxel-based 3D Point Cloud Semantic Segmentation: Unsupervised Geometric and Relationship Featuring vs Deep Learning Methods. *ISPRS International Journal of Geo-Information*, 8(5), 213. <https://doi.org/10.3390/ijgi8050213>
- Qi, Charles R. (2020). *Charlesq34/pointnet-autoencoder* [Python]. <https://github.com/charlesq34/pointnet-autoencoder> (Original work published 2018)
- Qi, Charles R., Liu, W., Wu, C., Su, H., & Guibas, L. J. (2018). Frustum pointnets for 3d object detection from rgb-d data. *Proceedings of the IEEE Conference on Computer Vision and Pattern Recognition*, 918–927.
- Qi, Charles R., Su, H., Mo, K., & Guibas, L. J. (2016). PointNet: Deep Learning on Point Sets for 3D Classification and Segmentation. *ArXiv:1612.00593 [Cs]*. <http://arxiv.org/abs/1612.00593>

- Qi, Charles Ruizhongtai, Yi, L., Su, H., & Guibas, L. J. (2017). Pointnet++: Deep hierarchical feature learning on point sets in a metric space. *Advances in Neural Information Processing Systems*, 5099–5108.
- Rakotosaona, M.-J., La Barbera, V., Guerrero, P., Mitra, N. J., & Ovsjanikov, M. (2019). POINTCLEANNET: Learning to Denoise and Remove Outliers from Dense Point Clouds. *Computer Graphics Forum*.
- Ravi, R., Lin, Y., Shamseldin, T., Elbahnasawy, M., Masjedi, A., Crawford, M., & Habib, A. (2018). Wheel-Based Lidar Data for Plant Height and Canopy Cover Evaluation to Aid Biomass Prediction. *IGARSS 2018 - 2018 IEEE International Geoscience and Remote Sensing Symposium*, 3242–3245. <https://doi.org/10.1109/IGARSS.2018.8518673>
- Richardson, J. J., Moskal, L. M., & Kim, S.-H. (2009). Modeling approaches to estimate effective leaf area index from aerial discrete-return LIDAR. *Agricultural and Forest Meteorology*, 149(6–7), 1152–1160.
- Rosipal, R., & Krämer, N. (2005). Overview and recent advances in partial least squares. *International Statistical and Optimization Perspectives Workshop" Subspace, Latent Structure and Feature Selection"*, 34–51.
- Ryu, Y., Nilson, T., Kobayashi, H., Sonnentag, O., Law, B. E., & Baldocchi, D. D. (2010). On the correct estimation of effective leaf area index: Does it reveal information on clumping effects? *Agricultural and Forest Meteorology*, 150(3), 463–472.
- Scharr, H., Briese, C., Embgenbroich, P., Fischbach, A., Fiorani, F., & Müller-Linow, M. (2017). Fast High Resolution Volume Carving for 3D Plant Shoot Reconstruction. *Frontiers in Plant Science*, 8. <https://doi.org/10.3389/fpls.2017.01680>
- Sonnentag, O., Talbot, J., Chen, J. M., & Roulet, N. T. (2007). Using direct and indirect measurements of leaf area index to characterize the shrub canopy in an ombrotrophic peatland. *Agricultural and Forest Meteorology*, 144(3–4), 200–212.
- ten Harkel, J., Bartholomeus, H., & Kooistra, L. (2020). Biomass and Crop Height Estimation of Different Crops Using UAV-Based Lidar. *Remote Sensing*, 12(1), 17. <https://doi.org/10.3390/rs12010017>
- van Ewijk, K. Y., Treitz, P. M., & Scott, N. A. (2011a). Characterizing forest succession in Central Ontario using LiDAR-derived indices. *Photogrammetric Engineering & Remote Sensing*, 77(3), 261–269.
- van Ewijk, K. Y., Treitz, P. M., & Scott, N. A. (2011b). Characterizing forest succession in Central Ontario using LiDAR-derived indices. *Photogrammetric Engineering & Remote Sensing*, 77(3), 261–269.
- van Klompenburg, T., Kassahun, A., & Catal, C. (2020). Crop yield prediction using machine learning: A systematic literature review. *Computers and Electronics in Agriculture*, 177, 105709.

- Velodyne VLP-32C*. (n.d.). Retrieved September 19, 2020, from http://www.mapix.com/wp-content/uploads/2018/07/63-9378_Rev-D_ULTRA-Puck_VLP-32C_Datasheet_Web.pdf
- Velodyne VLP-Puck Hi-Res*. (n.d.). Retrieved September 19, 2020, from http://www.mapix.com/wp-content/uploads/2018/07/63-9318_Rev-E_Puck-Hi-Res_Datasheet_Web.pdf
- Velodyne VLP-Puck LITE*. (n.d.). Retrieved September 19, 2020, from http://www.mapix.com/wp-content/uploads/2018/07/63-9286_Rev-H_Puck-LITE_Datasheet_Web.pdf
- Wang, Y., & Feng, H.-Y. (2015). Outlier detection for scanned point clouds using majority voting. *Computer-Aided Design*, 62, 31–43.
- Watson, D. J. (1947). Comparative physiological studies on the growth of field crops: I. Variation in net assimilation rate and leaf area between species and varieties, and within and between years. *Annals of Botany*, 11(41), 41–76.
- Welles, J. M., & Cohen, S. (1996). Canopy structure measurement by gap fraction analysis using commercial instrumentation. *Journal of Experimental Botany*, 47(9), 1335–1342.
- White, W. A., Alsina, M. M., Nieto, H., McKee, L. G., Gao, F., & Kustas, W. P. (2019). Determining a robust indirect measurement of leaf area index in California vineyards for validating remote sensing-based retrievals. *Irrigation Science*, 37(3), 269–280. <https://doi.org/10.1007/s00271-018-0614-8>
- Yan, G., Hu, R., Luo, J., Weiss, M., Jiang, H., Mu, X., Xie, D., & Zhang, W. (2019). Review of indirect optical measurements of leaf area index: Recent advances, challenges, and perspectives. *Agricultural and Forest Meteorology*, 265, 390–411.
- Yang, K.-W., Chapman, S., Carpenter, N., Hammer, G., McLean, G., Zheng, B., Chen, Y., Delp, E., Masjedi, A., & Crawford, M. (2021). Integrating Crop Growth Models with Remote Sensing for Predicting Biomass Yield of Sorghum. *In Silico Plants*.
- Zhang, L., Zhang, L., & Du, B. (2016). Deep Learning for Remote Sensing Data: A Technical Tutorial on the State of the Art. *IEEE Geoscience and Remote Sensing Magazine*, 4(2), 22–40. <https://doi.org/10.1109/MGRS.2016.2540798>
- Zhang, Liangpei, Zhang, L., & Du, B. (2016). Deep learning for remote sensing data: A technical tutorial on the state of the art. *IEEE Geoscience and Remote Sensing Magazine*, 4(2), 22–40.
- Zhao, K., & Popescu, S. (2009). Lidar-based mapping of leaf area index and its use for validating GLOBCARBON satellite LAI product in a temperate forest of the southern USA. *Remote Sensing of Environment*, 113(8), 1628–1645.

Zhu, X., Liu, J., Skidmore, A. K., Premier, J., & Heurich, M. (2020). A voxel matching method for effective leaf area index estimation in temperate deciduous forests from leaf-on and leaf-off airborne LiDAR data. *Remote Sensing of Environment*, 240, 111696. <https://doi.org/10.1016/j.rse.2020.111696>